

MICRO AND NANO FABRICATION OF STRUCTURES FOR LIGHT-MATTER INTERACTION

María Barra Burillo

PhD thesis

Supervised by:

Prof. Luis E. Hueso

Prof. Rainer Hillenbrand

Universidad del País Vasco

2023



*“Porque no el mucho saber harta y satisface el ánima,
mas el sentir y gustar de las cosas internamente.”*

San Ignacio de Loyola

Resumen

El término *nanofabricación* hace referencia al conjunto de procesos y técnicas que se emplean para generar estructuras en las que alguno de sus elementos presenta un tamaño inferior a 100 nm, para diseñar, crecer o retirar material con precisión casi nanométrica. Tener la posibilidad de acceder a estas dimensiones, de la escala de los átomos y las moléculas, permite grandes avances en la ciencia fundamental y aplicada.

En el día a día encontramos muchos productos en los que la nanociencia juega un papel importante: desde procesadores y otros componentes presentes en ordenadores, smartphones, televisiones, y en general detrás de cualquier pantalla, cada día más abundantes en comercios y lugares de ocio; hasta nuevos materiales para mejorar la resistencia de estructuras de vehículos, edificios, objetos y textiles. La industria y la sociedad demandan nanociencia, y se sigue avanzando para crear nuevos procesos y mejorar los ya existentes. Un ejemplo de ello es el reciente anuncio de la nueva biblioteca cuLitho, de la compañía Nvidia, que promete una mejora en la eficiencia técnica y energética de los procesadores dedicados a litografía a escala industrial. Se trata de una prueba de que, a pesar de los grandes avances y de los retos ya conquistados, la nanociencia y la nanofabricación son campos en continuo desarrollo.

Uno de los avances que más interés ha suscitado en los últimos años en todos los ámbitos es el descubrimiento de materiales bidimensionales. Estos materiales presentan enlaces débiles entre sus capas atómicas, por lo que, a

partir de exfoliación mecánica con cinta adhesiva, es posible obtener capas tan delgadas que pueden tener único átomo de espesor. El interés de este tipo de materiales radica sus propiedades, que difieren de las que se encuentran en estos mismos materiales a escala macroscópica. Entre ellas destacan: las propiedades mecánicas, ya que son muy flexibles y resistentes sin perder su integridad estructural; su alta conductividad eléctrica, que los hace candidatos ideales para integrar dispositivos electrónicos; o la posibilidad de modificar gradualmente sus propiedades ópticas, bien mediante procesos químicos, cambiando su composición, o factores externos como una deformación física (tensión) o la aplicación de voltaje. Además, presentan un alto ratio de superficie en poco volumen, una característica ventajosa para procesos de catálisis y reacciones químicas, ya que presentan una gran superficie activa, mejorando la eficiencia de estos procesos. Por todo ello, los materiales bidimensionales son considerados candidatos prometedores para una gran serie de aplicaciones.

Esta tesis se ha llevado a cabo combinando las técnicas ya existentes y disponibles en CIC nanoGUNE, con el objetivo de, realizando algunas modificaciones o caracterizando los parámetros involucrados, optimizar los procesos de preparación de muestras. De esta forma, mediante de la combinación de las técnicas anteriormente mencionadas y del uso y caracterización de materiales bidimensionales (2D), se han realizado muestras para una serie de estudios, principalmente relacionados con la nano óptica. La nano óptica estudia la interacción entre luz y materia en la nanoescala, empleando para ello plataformas tales como nanopartículas o superficies nanoestructuradas. Los materiales bidimensionales, dadas sus propiedades ópticas y su pequeño espesor, son una herramienta crucial para la observación de nuevos fenómenos ópticos a escala atómica.

Mediante la exfoliación mecánica usando trozos de celo azul de la compañía Nitto, conseguimos obtener capas finas de material, de espesores tan bajos como una única capa atómica. La caracterización del espesor de

estas capas se puede realizar en primera instancia mediante inspección visual en un microscopio óptico, y de forma cuantitativa usando técnicas como la microscopía de fuerza atómica o la espectroscopía Raman. La recogida y transferencia de las capas finas a un sustrato, bien desde el cielo azul o desde otro sustrato desde el cual se realizó su caracterización, para una posterior fabricación de estructuras específicas, es posible mediante el uso de sellos viscoelásticos de polidimetilsiloxano o técnicas específicas basadas en membranas adhesivas, como es el caso de los sellos recubiertos de membranas policarbonato, entre otros polímeros. Estas técnicas son también útiles para la fabricación de heteroestructuras, mediante el apilamiento sucesivo de capas de diferentes materiales bidimensionales.

Por otro lado, la fabricación de las muestras se ha realizado tanto directamente sobre sustratos, como sobre láminas de estos materiales bidimensionales. Con el objetivo de realizar la escritura de patrones y diseños, hemos empleado técnicas litográficas tales como la litografía óptica de escritura directa con haz láser y la litografía electrónica. En ambos casos, la litografía se realiza sobre una resina sensible, sin necesidad de una máscara física, lo que permite una mayor versatilidad y adaptabilidad de los diseños a los requerimientos de las muestras. Por otro lado, para quitar o añadir material hemos recurrido a técnicas se ha realizado la fabricación de capas finas de materiales mediante su deposición sobre sustratos, por evaporación o pulverización catódica (*sputtering*), o destrucción de material mediante técnicas de grabado, como el grabado con iones reactivos o por bombardeo de iones.

El potencial de estas técnicas queda puesto de manifiesto mediante la fabricación de muestras tanto sobre sustrato limpios como sobre materiales exfoliados, en el marco de distintos proyectos, a modo de colaboraciones. Uno de los problemas típicos en la fabricación de muestras usando litografía electrónica es la aparición del llamado efecto de proximidad, debido a la acumulación de carga en la resina, que sobreexpone los patrones a obtener

y afecta a sus dimensiones finales. Este efecto se observa en la preparación de matrices de varias micras de tamaño lateral formadas por tiras de unas pocas decenas de nanómetros de anchura separadas entre sí en el rango de distancias de 100 nm. Otro efecto estudiado es la escritura usando litografía electrónica sobre sustratos aislantes, que requiere el empleo de una capa conductora sobre la resina sensible que evite la acumulación de nubes de carga, y el desarrollo de pruebas de dosis para optimizar los parámetros de exposición requeridos.

El conocimiento sobre exfoliación de materiales bidimensionales y las posibilidades de la combinación de técnicas se ha aplicado en el estudio de la tensión sobre perovskitas híbridas. En los últimos años, las perovskitas de haluro de metal orgánico-inorgánico en capas (HOIPs) han surgido como materiales prometedores en el desarrollo de dispositivos optoelectrónicos, principalmente debido a su ancho de banda ajustable y alta movilidad de portadores. Se han propuesto diferentes técnicas para diseñar y ajustar sus propiedades ópticas, y en particular su fotoluminiscencia (PL, por sus siglas en inglés), por ejemplo, mediante la variación de su composición orgánico-inorgánica o la aplicación de deformación mecánica. De hecho, la ingeniería de deformación ha demostrado ser una estrategia efectiva para modular las propiedades optoelectrónicas de materiales bidimensionales (2D), pero apenas se ha explorado en perovskitas híbridas de haluro de metal. En este trabajo, investigamos la sintonización de la micro fotoluminiscencia de láminas de HOIP de bromuro de plomo 2D sujetas a deformación biaxial. Para este propósito, fabricamos una plataforma rígida con micro anillo de SiO_2 sobre la cual las láminas se colocan mediante estampado viscoelástico, lo que lleva a la formación de cúpulas. A bajas temperaturas, encontramos que una deformación inferior al 1% puede cambiar la emisión de PL desde un solo pico (sin deformación) a tres picos bien definidos. Combinando medidas de micro-PL realizadas en función de la temperatura, de la adquisición de mapas usando espectroscopía Raman y simulación numéricas

de elementos finitos para reconstruir analíticamente las estructuras obtenidas, confirmamos que la aparición de los dos nuevos picos de PL está relacionada con la coexistencia de deformaciones térmicas y mecánicas de tracción y compresión a lo largo de la lámina. Nuestros hallazgos brindan una nueva visión sobre la relevancia de la selección del material y el enfoque de la ingeniería de deformación para el diseño de dispositivos optoelectrónicos y de detección basados en deformación utilizando HOIPs 2D.

Independientemente a este proyecto, se ha realizado un estudio de la evolución del régimen de acoplamiento en micro cavidades clásicas construidas usando materiales bidimensionales. Recientemente, se ha estudiado ampliamente cómo algunas propiedades de materiales moleculares, como la reactividad química o las transiciones de fase, pueden verse afectadas por el acoplamiento fuerte de las vibraciones moleculares a un modo de micro cavidad. El acoplamiento entre fonones y modos de micro cavidad ha sido mucho menos estudiado, pero puede ofrecer posibilidades intrigantes tanto para estudios fundamentales como para aplicaciones. Utilizando cavidades basadas en nitruro de boro hexagonal (hBN), realizamos un estudio teórico y experimental de la evolución del régimen de acoplamiento en micro cavidades clásicas de Fabry-Pérot. Mediante exfoliación mecánica del hBN, podemos obtener capas delgadas y de alta calidad de manera controlada. Sorprendentemente, una capa delgada de 10 nm de hBN colocada en el centro de la micro cavidad es suficiente para lograr un acoplamiento fuerte, lo que demuestra que el régimen de acoplamiento fuerte se puede alcanzar con una cantidad muy pequeña de material fonónico. Además, se logra el régimen de acoplamiento ultra fuerte a partir de 100 nm de hBN. Por último, el estudio de cavidades completamente llenas produce una dispersión de polaritones que coincide con la de los polaritones fonónicos en cristales macroscópicos de hBN, lo que destaca que el acoplamiento máximo entre luz y materia en micro cavidades

está limitado por la fuerza de acoplamiento entre los fotones y el material a escala macroscópica. Los polaritones fonónicos formados en cavidades clásicas podrían convertirse en una plataforma versátil para estudiar cómo la fuerza de acoplamiento entre fotones y fonones puede modificar las propiedades de los cristales polares.

Abstract

The term nanofabrication refers to all those processes and techniques employed in the preparation of structures which include any feature below 100 nm. Using the tools that nanofabrication englobes, we are able to design structures, grow or remove material with near nanometric accuracy. Being able to access the realm of atoms and molecules leads to great advances for fundamental and applied science.

Nowadays, nanoscience plays a key role in many products that are at our reach, from processors and electronic components in computers, televisions, and smartphones, to new materials with improved properties, present in vehicles, buildings or even clothes. As both industry and society demand new advances, progress continues to be made. An example of this is the recent announcement of Nvidia's new cuLitho library, which promises to enhance the technical and energetical efficiency of processors devoted to industrial-scale lithography. This is evidence that, despite the significant advancements and challenges already achieved, nanoscience and nanofabrication are fields in continuous evolution.

One of the most important milestones reached in past years was the experimental discovery of bidimensional (or 2D) materials. 2D materials exhibit weak bonds between atomic layers, making it possible to easily isolate thin layers, even down to the single atom thickness. Their

properties differ from bulk materials: they are more flexible and mechanically resistant, present high mobilities and conductivity, and optical properties tunable by strain or electric gating. Furthermore, they have a high surface to volume ratio, improving the efficiency of catalytic processes and chemical reactions.

This thesis has been carried out using the techniques available at CIC nanoGUNE, with the aim of optimizing the preparation of samples by the controlled modification of the involved parameters and successive characterization of the results. We combine fabrication techniques with two-dimensional materials, to prepare samples for different applications, mainly related nanooptics. Nanooptics investigates the interaction between light and matter at the nanoscale, employing platforms such as nanoparticles or nanostructured surfaces. Two-dimensional materials, given their optical properties and small thickness, are a crucial tool for observing new optical phenomena at the atomic scale.

To obtain thin layers, or flakes, of material, with thicknesses as low as a single atomic layer, we mechanically exfoliate bulk crystals of van der Waals materials using blue Nitto tape. The thickness characterization of these layers can be initially performed through visual inspection under an optical microscope, and quantitatively using techniques such as atomic force microscopy or Raman spectroscopy. To pick up and transfer flakes to a substrate, either from the blue tape or from another substrate, for subsequent fabrication of specific structures, we use either viscoelastic polydimethylsiloxane stamps or specific techniques based on adhesive membranes, such as polycarbonate membranes. These techniques can also be exploited for the fabrication of heterostructures, formed by successive layers of different two-dimensional materials.

On the other hand, sample fabrication has been carried out both directly on substrates and on sheets of these two-dimensional materials.

To write patterns and designs, lithographic techniques such as direct laser writing lithography and electron beam lithography have been employed. In both cases, the design is written on a sensitive resist without the need for a physical mask, allowing greater versatility and adaptability of the designs to the requirements of the samples. Moreover, for material deposition, we employed techniques such as evaporation or sputtering, whereas reactive ion etching or ion bombardment, have been used to controllably remove material.

The potential of these techniques is demonstrated through the fabrication of samples both on clean substrates and on exfoliated flakes, as part of different projects and collaborations, which allows the detailed study of the described techniques. For instance, a typical problem encountered in sample fabrication using electron beam lithography is the appearance of the so-called proximity effect, due to charge accumulation in the resist, which overexposes the desired patterns and affects their final dimensions. This effect is observed in the preparation of several micrometer-sized arrays formed by nano ribbons with few tenths of nanometers of width, separated by distances in the range of 100 nm. Other observed effect when using electron beam lithography on insulating substrates is the accumulation of charge on the resist, which requires the use of a conductive layer on top of the resist to prevent the charge buildup, and the performance of dose tests to optimize the required exposure parameters.

The knowledge of two-dimensional material exfoliation and the possibilities derived from the combination of techniques have been applied in the study of strain on hybrid perovskites. In recent years, layered hybrid organic-inorganic metal halide perovskites (HOIPs) have emerged as promising materials in the development of optoelectronic devices, mainly due to their tunable bandgap and high carrier mobility.

Different techniques have been proposed to design and adjust their optical properties, particularly their photoluminescence (PL), such as varying their organic-inorganic composition or applying mechanical strain. In fact, strain engineering has been shown to be an effective strategy to modulate the optoelectronic properties of two-dimensional (2D) materials, but it has been barely explored in hybrid metal halide perovskites. In this work, we investigate the tuning of micro photoluminescence of 2D lead bromide HOIP sheets subjected to biaxial strain. For this purpose, we fabricate a rigid platform with a SiO₂ micro-ring on which the sheets are placed using viscoelastic stamping, resulting in the formation of domes. At low temperatures, we find that strain below 1% can change the PL emission from a single peak (no strain) to three well-defined peaks. Combining temperature-dependent micro-PL measurements, mapping acquisition using Raman spectroscopy, and finite element numerical simulations to analytically reconstruct the obtained structures, we confirm that the appearance of the two new PL peaks is related to the coexistence of thermal and mechanical tensile and compressive strains along the sheet. Our findings provide new insights into the relevance of material selection and strain engineering approach for the design of optoelectronic and strain-based sensing devices using 2D HOIPs.

Moreover, an investigation of the evolution of the coupling regime in classical microcavities constructed using two-dimensional materials was also conducted, taking advantage of the knowledge on the fabrication of heterostructures of bidimensional materials. Recently, there has been extensive research on how certain properties of molecular materials, such as chemical reactivity or phase transitions, can be affected by the strong coupling of molecular vibrations to a microcavity mode. The coupling between phonons and microcavity modes has been much less studied, but it holds intriguing possibilities for fundamental studies and applications.

Using cavities based on hexagonal boron nitride (hBN), we perform a theoretical and experimental study on the evolution of the coupling regime in classical Fabry-Pérot microcavities. By mechanically exfoliating hBN, we can controllably obtain thin and high-quality layers. Remarkably, a thin layer of 10 nm of hBN placed in the center of the microcavity is sufficient to achieve strong coupling, demonstrating that the strong coupling regime can be reached with a very small amount of phononic material. Furthermore, the ultrastrong coupling regime is achieved from 100 nm of hBN onwards. Finally, the study of fully filled cavities results in a polariton dispersion that matches that of phonon polaritons in macroscopic hBN crystals, highlighting that the maximum light-matter coupling in microcavities is limited by the coupling strength between photons and the bulk material. Phonon polaritons formed in classical cavities could become a versatile platform for studying how the coupling strength between photons and phonons can modify the properties of polar crystals.

TABLE OF CONTENTS

Resumen	i
Abstract	vii
1. Exfoliation and transfer of 2D materials.....	7
1.1. Mechanical exfoliation of 2D materials	8
1.1.1. Preparation of the exfoliation tape	10
1.1.2. Determination of the flake thickness by optical contrast	12
1.2. Direct exfoliation on Si/SiO₂ substrate for the obtention of large-area graphene monolayers	16
1.3. Deterministic dry transfer using viscoelastic stamps.....	18
1.4. Transfer and stacking techniques.	23
1.4.1. Pick up and transfer using PDMS stamp.....	23
1.4.2. Transfer using a polycarbonate (PC) membrane.	25
1.4.3. Wet transfer using a PMMA carrying membrane.	27
1.4.4. Fabrication of heterostructures of 2D materials.....	32
1.5. Conclusions	35
2. Nanofabrication	37
2.1. Defining a pattern by lithography.....	39
2.1.1. Direct Laser Writing (DWL) lithography	39
2.1.2. Electron Beam Lithography (EBL).....	41
2.1.3. Polymeric resists for lithography.....	42

2.1.4. Spin coating step.....	45
2.1.5. Patterning a sample using EBL.....	50
2.2. Metallization and lift-off.....	56
2.3. Etching.....	58
2.3.1. Hard mask for etching.....	60
2.4. Conclusions.....	62
3. Design and optimization of fabrication processes	63
3.1. Fabrication of SiO₂ nanogratings for coherent phononics ...	64
3.1.1. Coherent phononics on van der Waals materials.....	64
3.1.2. Fabrication protocol of SiO ₂ nanogratings.....	66
3.2. ML-hBN nanoribbon arrays for observation of phonon polariton resonances	68
3.2.1. Motivation for the search and manipulation of CV ML-hBN phonon polaritons.....	68
3.2.2. Fabrication process of ML-hBN nanoribbons.....	69
3.2.3. Summary of results.....	70
3.3. Nanoresonators on thin membranes for magneto-optical studies	71
3.3.1. Magneto-optics and plasmonic nanorings.....	71
3.3.2. Substrate preparation and spin coating.....	72
3.3.3. Importance of the design and writing modes during the EBL exposure of the structures.....	73
3.3.4. Metal deposition and lift-off of nano structures on TEM membranes	75
3.3.5. Fabrication summary and results of EELS characterization.....	76

3.4. Nanoresonators on transparent substrates for PL enhancement	78
3.4.1. Motivation and previous works	78
3.4.2. Fabrication of nano slits arrays.....	80
3.4.3. Fabrication of nano antennas arrays.....	82
3.4.4. Characterization of the metasurfaces	84
3.4.5. Summary of results and outlook	85
3.5. Fabrication of a single THz resonator on hBN-graphene for ultrastrong light-matter coupling	86
3.5.1. Previous works and sample design	86
3.5.2. Edge contacts for electrical measurements.....	89
3.5.3. Fabrication of the single resonator using EBL.....	92
3.5.4. Measurements and perspectives	94
3.6. Conclusions	95
3.7. Appendices: fabrication recipes	98
3.7.1. Parameters for electrical contacts at the EBL	98
3.7.2. RIE recipes.....	98
3.7.3. Ion Miller recipes	98
4. Strain modulation of the photoluminescence of 2D perovskites.....	99
4.1. Selection of the composition and structure of the perovskite	100
4.2. Transfer of 2D HOIP flakes on SiO ₂ rings.....	102
4.2.1. Preparation of rings on SiO ₂ /Si substrates.....	102
4.2.2. Exfoliation and transfer of 2D perovskites on microstructures ...	104
4.3. Photoluminescence and Raman spectroscopy studies.....	107

4.4. Reconstruction of mechanical behavior via reverse engineering	110
4.5. Conclusions.....	112
4.6. Appendices	113
4.6.1. AFM study	113
4.6.2. Estimation of the strain from the AFM profiles	115
4.6.3. Publisher permission	116
5. Phonon-photon coupling in microcavities filled with hBN	117
5.1. Introduction	118
5.2. Fabrication of hBN filled microcavities tuned to the hBN TO phonon.....	121
5.2.1. Fabrication of fully filled microcavities.....	123
5.2.2. Fabrication of microcavities embedding a thin layer of hBN.....	124
5.3. Infrared spectroscopy and analysis of hBN-filled microcavities	127
5.3.1. Experimental and numerical study of microcavities tuned to the TO phonon of hBN.....	127
5.3.2. Evolution of the coupling strength with the cavity filling factor ..	130
5.3.3. Ultrastrong coupling in fully filled cavities.	133
5.4. Comparison of polariton dispersion	134
5.5. Conclusions.....	137
5.6. Appendices	139
5.6.1. Fourier Transform Infrared Spectroscopy	139
5.6.2. Characterization of the optical parameters of the materials used in the microcavities	140

5.6.3. Determination of the coupling strength g in TM simulations	142
5.6.4. Comparison between phonon polariton dispersions.....	143
6. Summary and final conclusions.....	145
List of recipes	153
Acronyms	155
Publications	157
References	159
Acknowledgements	179

1 ● Exfoliation and transfer of 2D materials

Two-dimensional (2D) materials are crystalline structures that present weak bonds, typically van der Waals, between their atomic layers. The atomic planes can be hence separated using mechanical exfoliation [1], making 2D materials an ideal platform for studying phenomena down to the atomic thickness. Ever since the first experimental isolation of graphene using mechanical cleavage of graphite [2], the family of 2D materials has significantly increased [3]. The layered nature of 2D materials allows great control over the thickness of the exfoliated flakes, which present atomically flat surfaces, and high crystalline quality [1,4–6].

There are several techniques for the obtention of thin layers of 2D materials, with distinct advantages and disadvantages for the fabrication of functional samples. For instance, liquid [7–9] and mechanical [10–12] exfoliation yield good quality thin flakes from bulk crystals, but these techniques are not scalable since the flakes are typically very small in size. On the other hand, techniques such as chemical vapor deposition (CVD) or epitaxial growth yield wafer-scale thin layers, but typically with lower crystalline quality [13–15].

In this chapter, we focus on the fabrication of flakes using mechanical exfoliation of 2D materials. This type of fabrication is not always

straightforward, and there are many protocols and strategies that our group has been developing over the years. Often, some of those details are left out of manuscripts and are only passed verbally from generation to generation of researchers. Eventually, some important information may be lost in the process. In this chapter, we thus present a compilation of tricks and techniques for a successful preparation of samples comprising flakes of 2D materials.

1.1. Mechanical exfoliation of 2D materials

2D materials are characterized by their ability to be exfoliated into thin layers, ideally down to the atomic monolayer. One of the methods for thinning down 2D materials is via mechanical exfoliation, by cleaving successive layers using adhesive tape, as shown in the schematic presented in Figure 1.1. However, there is not just one correct protocol for exfoliation, and techniques that work well for one person or material may differ slightly from those that work for another. For instance, the amount of material that a person extracts from a bulk crystal may depend on their manual strength as much as on the type of tape they are using. However, the main concepts and procedures can be inferred. Having a fundamental understanding of what to do and what not to do can make a significant difference in the amount of time spent optimizing sample preparation, reducing it from months to days. In this section, we review the preparation of blue tape for exfoliation of flakes of different thicknesses, and give some details for the exfoliation of hexagonal Boron Nitride (hBN), MoS₂ and graphene, as significative 2D materials.

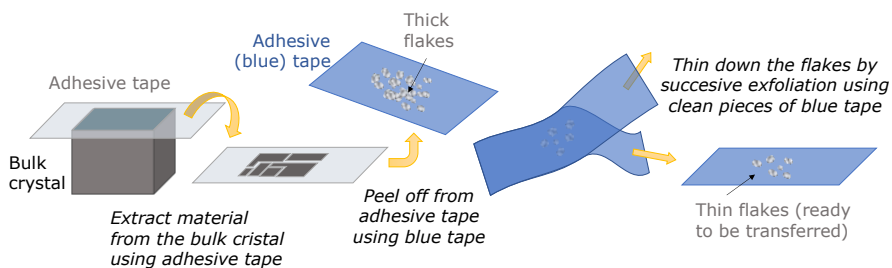


Figure 1.1: Schematic of the obtention of thin flakes using adhesive tape via mechanical exfoliation of a bulk crystal.

Additional information 1.1.: List of lab material required for the exfoliation process

To start exfoliating, it is important to first prepare all the materials that will be used in the process:

1. Bulk crystal from which to extract the flakes.
2. Adhesive tape to successively separate layers of material. The type of tape used will also affect the process of exfoliation and transfer. In general, the so-called “blue tape” is recommended for exfoliation over commercial Scotch tape. The best, and most used, is the blue tape commercialized by the Nitto company to protect metallic surfaces¹. This tape has a weak adhesion glue, leaving less residues after the flake transfer process, and making it possible to separate the sheets of tape from each other without applying too much strain or tearing the material. The blue tape is normally sold in rolls, from which we cut thick square, single layer pieces, as shown in Figure 1.2a.
3. Sharp tweezers, useful to separate, and handle pieces of blue tape.
4. Platform to transfer and identify the flakes, either a substrate or a stamp. One option is to transfer the flakes from the blue tape to a substrate (as described in section 1.2. Another common procedure is to transfer the flakes from the blue tape to viscoelastic polydimethylsiloxane (PDMS) stamps as shown in Figure 1.2b (see section 1.3 for details on this type of transfer). Stamps can be prepared by cutting square pieces from commercial sheets². For cleaner stamps, one can also buy PDMS in pellets or powder to prepare films or droplets.
5. In the case of working with PDMS stamps, microscope glass slides will be used as holders for the stamps.

¹ Available at https://www.nitto.com/eu/en/products/surface/spv_metal017/

² Available at <https://www.gelpak.com/gel-film/dgl-film/>

1.1.1. Preparation of the exfoliation tape

One of the most important steps to obtain good flakes of 2D materials is to transfer some material from the original crystal to a clean piece of tape. This piece of blue tape needs to have enough material, in the appropriate state of exfoliation, to obtain a successful transfer. These two parameters may vary with the material to be exfoliated, and the desired thickness of the final flake. Being aware of this, and to start to prepare the sample, we need to transfer some material from the original crystal to a piece of blue tape.

Usually, 2D materials are synthesized in the form of crystals, that vary in size from powder with of approximately 100 μm of mean size to centimeters-big crystals. To begin to exfoliate from a powder-like crystal, we need to place a bit of the powder on the blue tape. To avoid dropping an excessive amount of material, we can use either the tip of clean tweezers or a plastic spatula to pick material from its recipient. Once on the blue tape, we transform the original crystals into thin flakes by successively peeling them off the starting tape using new, clean pieces of tape, until we can use the tape for transferring the flakes (Figure 1.2c). On the other hand, if we need to start the exfoliation from a bigger crystal, we carefully peel its first layer using either commercial scotch tape or a clean and big piece of blue tape, and we save the rest of the crystal. Then, we use a piece of blue tape to extract some material from the scotch tape and proceed with the exfoliation process as described above. We repeat the exfoliation step until we consider that the amount of material on the blue tape is enough for obtaining the desired flakes. The criteria will vary for different materials and thicknesses. For instance, for obtaining thin layers of hBN, the material on the blue tape needs to be almost invisible to the bare eye. However, for graphene, it is better to have big pieces to not break it down in excess.

In the final step, we need to transfer the flakes that we have on the blue tape to the substrate on which we will fabricate the final sample. The most common technique for exfoliation and transfer of 2D flakes is the deterministic dry transfer, that uses transparent poly dimethyl-siloxane (PDMS) stamps to select and transfer the flake to the final substrate. The transfer from blue tape to

PDMS stamps and from the PDMS stamps to substrates is detailed further on in this chapter, in section 1.3. However, some 2D materials cannot be exfoliated using this method. Depending on the optical properties of the material, the optical contrast of thin flakes on PDMS may be so low that it does not allow identification of the flakes. It can also happen that the low affinity between the PDMS and the material itself prevents any flakes from being transferred from the blue Nitto tape to the stamps. For these materials, new strategies were developed and optimized according to the requirements of each sample. Such is the case of graphene, that needs to be exfoliated directly on SiO_2 substrates, as is described in section 1.2.

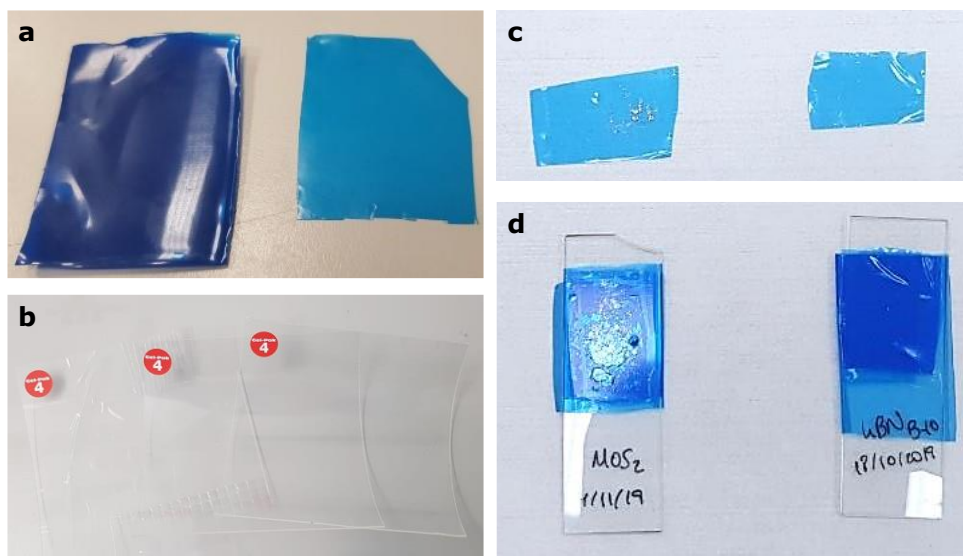


Figure 1.2: Some of the tools and materials required for the exfoliation of thin flakes of 2D materials. a) Pieces of blue tape cut from the original roll. The piece on the left shows a stack of blue tape as directly cut from the roll, from which we can separate a single layer, shown on the right. b) PDMS gel sheets from which we prepare the stamps for the transfer. c) Pieces of blue tape containing MoS_2 (left), that can be seen as bright, grey spots on the tape, and hBN (right), almost invisible already in this step of exfoliation. d) Suggestion for storing reusable pieces of blue tape containing exfoliated material, using microscope glass slides.

Additional information 1.2.: Storage of pieces of blue tape containing exfoliated material

- The pieces of blue tape with material can be used for multiple exfoliations, so after obtaining the desired flakes, it is advisable to keep them separately and labelled.
- One way of storing them is to put them together, the sticky side of the first covering the non-sticky part of the next one, and then fix them to a microscope glass slide, as shown in Figure 1.1d.

1.1.2. Determination of the flake thickness by optical contrast

One of the most important parameters when talking about 2D materials is the number of layers in a specific flake, i.e., its thickness. For all of the materials, the thickness can be determined within a range of values by optical inspection, in some cases even down to the monolayer [16] (see section 1.2 for exfoliation of graphene monolayers). Optical inspection of the substrates or the PDMS stamps is performed at an optical microscope, using reflection mode. The optical contrast, i.e., the difference of intensity between the collected light coming from the substrate and from the flake, allows us to identify the flake and give a first approximation for its thickness.

The optical contrast is determined by the optical properties of the material itself and the thickness of the flake, but also by the substrate below the flake [17–19]. During the development of this thesis, most of the exfoliation and transfer was done on standard commercial substrates of Si with 300 nm of SiO₂ thermally grown, generally also used for the fabrication of electronic devices. Flakes generally stick well to Si/SiO₂ substrates and exhibit sufficient optical contrast to identify them. As mentioned, the substrate affects the optical contrast of the flakes. The air/flake/substrate structure behaves as a multilayer structure, due to the absorption of light and the change of the optical path, which is also wavelength dependent. Thus, we will observe different colors and

contrast coming from the flake than coming from the bare substrate or from flakes with different thicknesses. This effect can be described by Fresnel law of multilayer interference [17] and derives in the possibility of accurate identification of the thickness of the flakes. By changing the thickness of the SiO₂ layer, the range of flake thickness we are able to distinguish is also changed. For example, the thinnest hBN flake one can observe on 300 nm of SiO₂ thermally grown on Si is approximately 5-10 nm thick, whereas for 90 nm SiO₂ on Si it is possible to identify hBN flakes down to the monolayer [20,21]. Furthermore, graphene monolayers can be optically identified on Si/SiO₂ (300nm) substrates. Figure 1.3 shows a characterization of graphene monolayer (1L), bilayer (2L) and multilayer on Si/SiO₂ (300 nm) substrate. The recorded values from the red, blue, and green channels of the optical microscope are shown in panel c. The step between the substrate and the monolayer, and between graphene layers can be identified in the green channel as a step of approximately 20 counts in intensity. The flake shown in Figure 1.3b is characterized at the AFM as shown in Figure 1.3d-e, to measure its thickness. The profile of the 1L-2L area marked in Figure 1.3d by an arrow is shown in Figure 1.3f. To properly identify a monolayer and quantitatively differentiate it from a bilayer or an even thicker flake, it is useful to also do Raman spectroscopy, particularly for transition metal dichalcogenides (TMDs) [22,23] and graphene [24,25]. For some materials, such as hBN, the thinnest flakes that we can observe at the optical microscope is around 10 nm, but it has been reported the possibility to also identify monolayers optimizing the microscope and camera settings [21].

For exfoliation of flakes thicker than the monolayer, it is useful to prepare a color scale to allow visual identification of thickness. An exfoliated wedge of hBN on PDMS and on a Si/SiO₂ substrate and the corresponding color scales are shown in Figure 1.4a-b and c-d respectively. To prepare this kind of color scale, we take the optical image when the flake is on the PDMS, and then transfer it to a substrate. This is useful, since normally we look for the flakes of the aimed thickness on PDMS, before transferring them to a substrate (the transfer process using PDMS stamps is described exhaustively in section 1.3 of this chapter). Once on the substrate, we do AFM measurements to characterize

the thickness and link them to the observed color. Figure 1.4a and Figure 1.4c show the optical image of an hBN flake on PDMS and Si/SiO₂ (300 nm) respectively. The correspondence between color and thickness of hBN on PDMS is shown in Figure 1.4b, and for the same flake and thicknesses but on Si/SiO₂ (300 nm) substrate in Figure 1.4d. Another example of a color scale is shown in Figure 1.5, in this case for a MoS₂ flake on PDMS stamp.

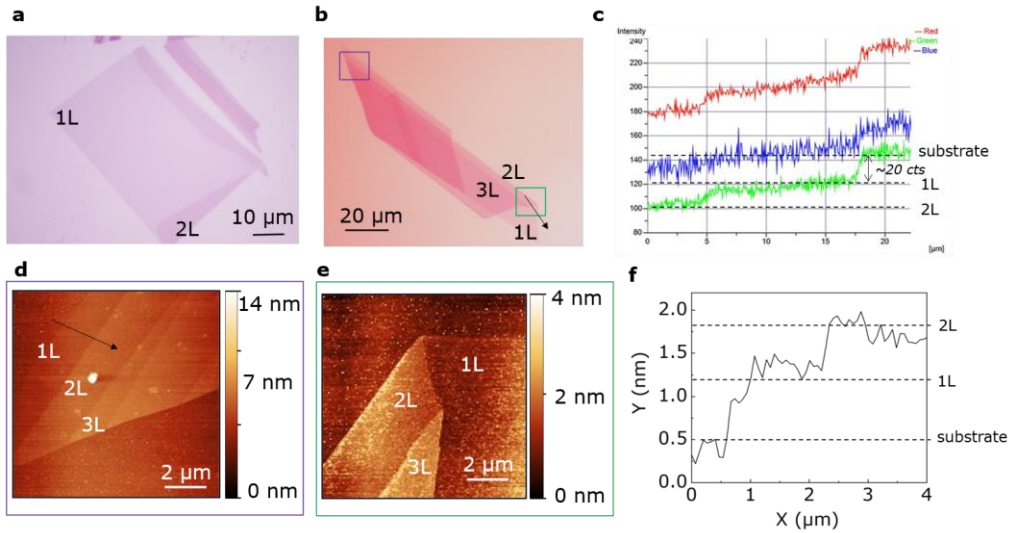


Figure 1.3: Optical contrast of graphene flake on a Si/SiO₂ substrate.

a) Optical image of a graphene flake on Si/SiO₂ (300 nm substrate), captured using a Leica microscope [26]. b) Optical image of a graphene flake on Si/SiO₂ (300 nm) substrate, captured using a Nikon microscope [27] and shown next to (a) to exemplify the slight change on the color tone due to the use of two different microscopes, that however do not affect to the identification of the monolayer. The 1L, 2L and 3L areas are characterized by the AFM measurement shown in panels (d) and (e), marked by the purple and green lines, respectively. The black arrow indicates the area from which the optical intensity measurement shown in (c) was taken. c) Measurement of the intensity counts in the line marked by the black arrow in (b), corresponding to the red, green and blue channels. d) AFM map of the area marked by the purple line in (b). AFM map of the area marked by the purple line in (b). The black arrow marks the line for the profile shown in (f) e) AFM map of the area marked by the green line in (b). f) AFM profile marked by the black arrow in (d), for the characterization of the monolayer and bilayer parts of the flake.

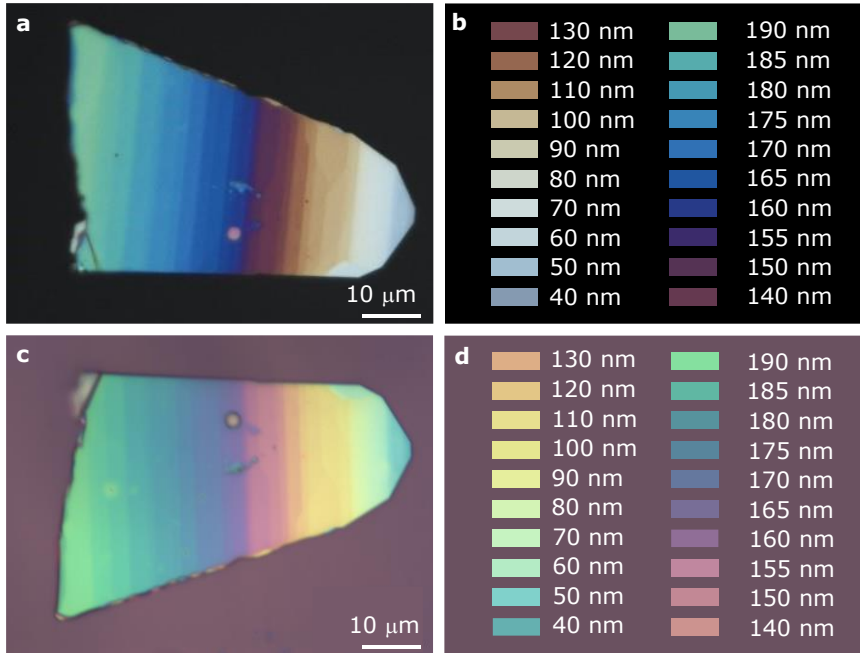


Figure 1.4: Color scales of hBN. a) hBN wedge on PDMS stamp. b) Color scale for different hBN thicknesses as observed on PDMS. c) hBN wedge shown in (a), after transfer to Si/SiO₂(300nm) substrate. d) Color scale of hBN on Si/SiO₂(300nm) substrate.

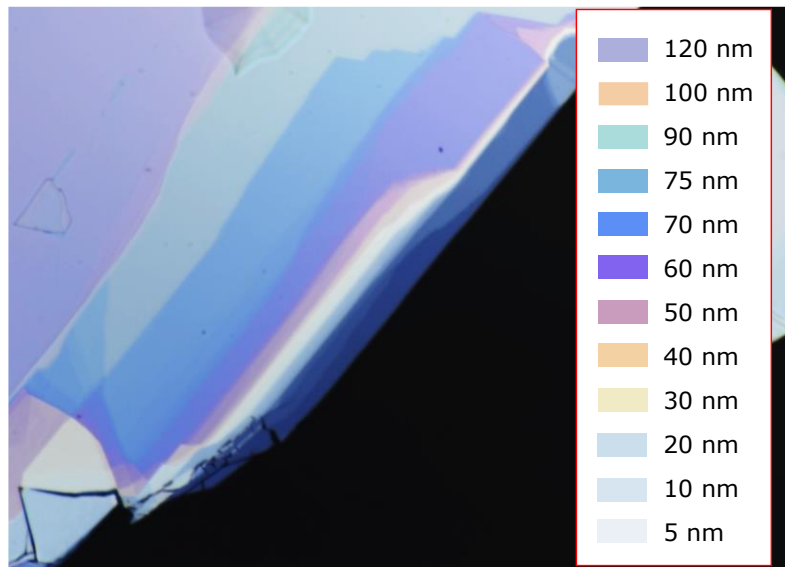


Figure 1.5: MoS₂ color scale on PDMS stamp.

Additional information 1.3.: General considerations for the thickness characterization of flakes using optical contrast

- Note that the color tone of the flakes may slightly vary for different optical microscopes, due to differences in the optic elements of the equipment, such as the objective lenses, the camera or the light source.
- An example of the change of the color tone of two graphene flakes on Si/SiO₂ (300 nm) can be seen in Figure 1.3a-b. Figure 1.3a shows the image of a graphene flake captured at a microscope from Leica Microsystems [26], whereas the image shown in Figure 1.3b was captured using a microscope from Nikon [27]. As can be observed in these two images, although the color is not exactly the same, the color contrast between the flake and the substrate is in both cases almost identical.
- Nevertheless, it is advisable to configure the settings for the characterization of the flakes to be comparable by setting the light intensity, white balance and exposure time.

1.2. Direct exfoliation on Si/SiO₂ substrate for the obtention of large-area graphene monolayers

Monolayer graphene is invisible on PDMS. Furthermore, the humidity and presence of non-cross-linked polymers on the PDMS stamp makes its affinity to graphene to be very low [28]. If we tried to exfoliate graphene on a PDMS stamp, we would only obtain thick flakes [29,30]. Given all this, and to obtain big areas of monolayer graphene, we need to exfoliate directly on a Si/SiO₂ substrate [31].

There are two key aspects that play an important role during the exfoliation process of graphene monolayers. First, we need to have enough material which is not too broken on the blue tape, but that has undergone several exfoliations, so that it is thin enough to produce large monolayers. Secondly, we need to prepare the substrates that we will use for the final exfoliation step. We will

exfoliate directly on a Si/SiO₂ (300nm) substrate and then proceed to look for appropriate flakes. Picking up the flake after this step might be required for the preparation of heterostructures, or to transfer it to a different substrate

To maximize the number of monolayers on the substrate, we use big, manually cut pieces of Si/SiO₂ substrate. It is important that the Si/SiO₂ substrate was never coated with any polymer, nor cleaned in acetone or any other solvents. Not having any polymers on the substrate enhances the adhesion of the flakes. Furthermore, we need to remove any traces of humidity on the substrate to favor the exfoliation process. Therefore, to have the substrates ready for exfoliation, we leave them on a pre-heated hot plate at 100°C, during the preparation of the blue tape. Oxygen plasma can also help to clean the Si/SiO₂ substrates, and a process of just 60 seconds of plasma before heating the substrates is enough to improve the adhesion of graphene flakes. However, it will make more difficult the pick-up process, so this step is not generally recommended when planning to pick-up the flakes for a subsequent fabrication of heterostructures.

While the substrates are being heated to eliminate humidity, we can proceed to exfoliate the material from bulk crystal to monolayers. We always start from a big graphite crystal, from which we peel off the first layer using scotch tape. Then, we exfoliate from the tape just 2-3 times using big pieces of blue tape. As previously mentioned, graphene does not stick properly to the substrates, hence the need to have abundant material on the blue tape. After these 2-3 rounds of exfoliation from the original layer, we prepare some more pieces of blue tape of approximately the size of the Si/SiO₂ substrate that we will use. We transfer some material to these pieces of blue tape, which will only be used once. It is advisable to prepare several substrates each time since the success ratio may vary. After this step, we should have as many pieces of blue tape prepared with material as substrates containing graphene flakes, we want to produce.

With everything ready, we take one substrate from the hot plate. Immediately after, we place one of the pieces of blue tape on top. We gently press the blue tape against the substrate to remove bubbles, using the tip of a finger, without rubbing. We then place the substrate with the blue tape still on

it again on the hot plate for about a minute. Finally, we take them out and let them cool down for a couple of minutes before very slowly removing the blue tape from the substrate, which should now contain many graphene flakes, including monolayer and bilayer flakes. Graphene monolayers are very thin, but still give enough contrast to identify them (see images and further explanation on the optical identification of graphene monolayers in Figure 1.3 and section 1.1.2).

Additional information 1.4.: Exfoliation of hBN directly on SiO₂/Si substrates

- It is also possible to exfoliate hBN directly on Si/SiO₂ substrates, as in the case of graphene, by putting a good amount of material on the blue tape, and again using pre-heated substrates to avoid humidity and enhance the adhesion of hBN flakes.
- The minimum thickness that can be identified after this type of exfoliation is determined by the SiO₂ thickness, as commented in section 1.1.2.

1.3. Deterministic dry transfer using viscoelastic stamps

Described by A. Castellanos et al. in [32], the goal of the deterministic dry transfer technique is to transfer some flakes from the blue tape to a prepared viscoelastic stamp, normally PDMS, and then from the stamp to the final substrate. As discussed in the previous section, PDMS can be used to obtain monolayers of materials with high reflective index, such as TMDs, which give enough optical contrast to be optically identified down to the monolayer. Some other materials, such as hBN or 2D perovskites, can be transferred to PDMS stamps, but as mentioned on section 0, the optical contrast is not enough to allow the direct identification of monolayers. Finally, other materials, such as graphene or MoO₃, exhibit low affinity to the PDMS, making the transfer from

blue tape to the stamp almost impossible. Only a few thick flakes of several tenths of nanometers will adhere to the stamp.

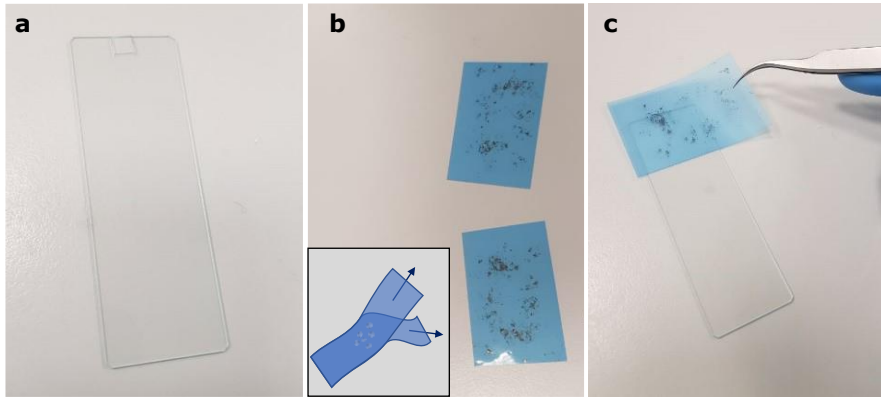


Figure 1.6: Preparation for the transfer. a) PDMS stamp on the glass slide. b) Pieces of blue tape containing exfoliated material, inset shows a schematic of the thinning of the flakes on the blue tapes by placing two of them together and successively separating them. c) Blue tape covering the PDMS stamp, in order to have some material transferred on it.

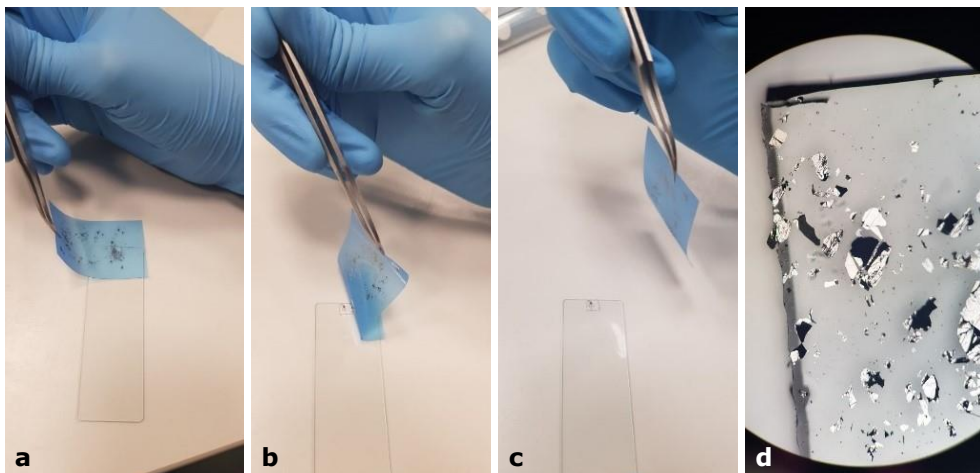


Figure 1.7: Exfoliation on PDMS stamp process. a) Using tweezers, carefully start to lift the blue tape from the PDMS stamp. b) Peel the blue tape until we completely remove the blue tape from the stamp, as shown in c). d) Optical microscope image of the surface of the PDMS with the results of the exfoliation.

To prepare the stamps, we use commercial PDMS sheets (gel-pak, Gel-Pak® Part n: PF-3-X4³), that we cut into square shaped stamps of a few millimeters of lateral size. We place the prepared stamp on a microscope glass slide for better handling (Figure 1.6a). Using the piece of blue tape containing the exfoliated material (Figure 1.6b), we cover the PDMS stamp (Figure 1.6c). We gently press down and quickly peel the tape from the stamp (Figure 1.7a-c). Finally, we look for flakes on the surface of the PDMS, using an optical microscope (Figure 1.7d).

When exfoliating flakes, we are normally targeting certain characteristics, such as thickness or lateral size. The thickness of the flakes can be determined to a certain level by optical contrast (see section 0 in this chapter for color scales and examples of exfoliation of 2D materials), that is normally enough for the fabrication of the samples. In some cases, the optical contrast of the flake on the PDMS stamp is high enough to differentiate down to the monolayer, as in most TMDs [10]. Atomic force microscopy (AFM) or Raman spectroscopy is normally used in these cases to completely characterize [22–24]. Once we find a flake that fulfills the requirements of thickness and size that we need for the preparation of the final sample, we are ready to proceed to the transfer step.

Now we need to transfer the flakes from the PDMS stamp to a substrate. The detailed schematics of the transfer process using PDMS stamp is illustrated in Figure 1.8, while the transfer, or delamination, system employed for the transfer is shown in Figure 1.9. It consists on a stage and a micro-controlled arm, that allow the alignment of the flake and the substrate (Figure 1.9a). The sample is fixed on the stage, that can move and rotate to adjust the position of the sample. The glass slide containing the PDMS stamp and thus, the flake, is fixed to the micro controlled arm. The arm can move over the stage, thus positioning the flake over the substrate. The system is coupled to an optical microscope, so that we are able to locate the flake on the PDMS stamp, and to visualize the substrate below them. Before transferring the flake to the substrate, we first need to find the flake on the PDMS stamp. Then, we need

³ Available at <https://www.gelpak.com/gel-film/dgl-film/>

to locate the area of the substrate on which we want to make the transfer. We align the substrate and the flake so that the transfer may happen in the position of our choosing. Then, we lower the glass slide until the PDMS nearly touches the substrates (Figure 1.9b). We fine tune the alignment with the micrometric screws of the glass slide arm-holder and lower again the arm until contact between the PDMS and the substrate is achieved.

Once we have the flake aligned at the position where we want to place it, we keep lowering the arm to press the stamp and the flake against the substrate. We leave the stamp to relax for a few seconds, before proceeding to lift the arm very slowly. After this step, the PDMS should have released the flake, that will stay adhered to the substrate.

Additional information 1.5.: Some guidelines and information for the transfer step from the PDMS stamp to a substrate

- To avoid transferring too many flakes around the desired one (which may affect posterior fabrication processes on the sample), it is recommended to transfer the flake with a slight angle between the substrate and the flake. For this purpose, depending on the system, the arm or the stage can be tilted in the required direction.
- For transferring thick flakes, over 100 nm, after achieving contact, it is helpful to press down the PDMS stamp against the substrate using the tip of a tweezer.
- Normally, thin flakes stick to the substrates without any issue. However, thicker flakes might be more irregular and present some difficulties in the transfer process. If the flake does not stick to the substrate, there are different strategies that can help. Moving the arm and the stage to the X and Y directions while lifting the PDMS helps to release thick flakes.
- Stamping from the direction that will make the PDMS lift from the flatter part of the flake will also increase the probability that the flake detaches from the PDMS and stays on the substrate.

- Increasing the temperature of the stage during the transfer can also help the flakes to stick to the substrate, but it is always important to keep in mind possible critical temperatures for the materials that you are using.

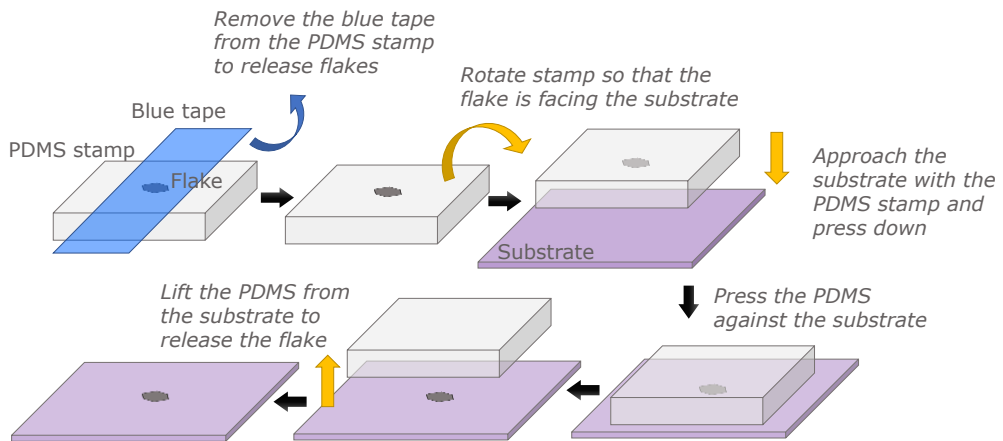


Figure 1.8: Process for transferring flakes using PDMS stamp. Black arrows indicate the succession of steps, while blue and yellow arrows indicate movement of the elements in the process.

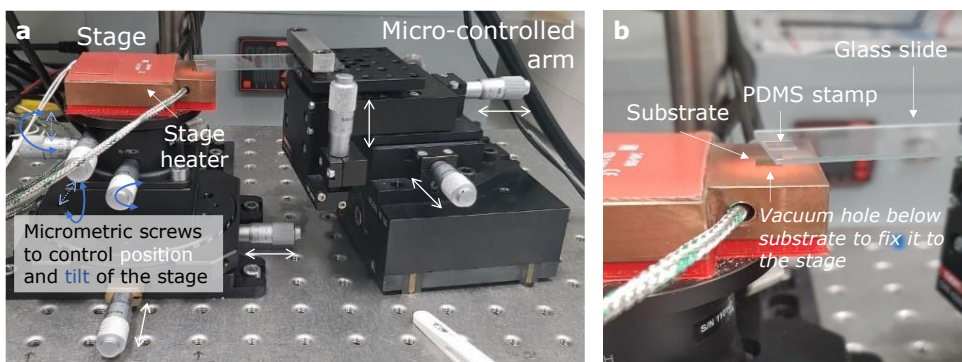


Figure 1.9: Delamination system. a) General view of the delamination system: the screws pointing out of the stage and the glass holder allows micrometric control on all directions. b) Zoom into a substrate placed on the holder and a glass slide containing a PDMS stamp with flakes, ready for the transfer.

1.4. Transfer and stacking techniques.

In many cases, we are interested in studying the properties of the material, so we can proceed with the characterization or fabrication of structures after transferring just one flake. However, some other times we need to prepare more complex structures that involve new transfer techniques, or successive fabrication and characterization techniques. Here, we show in detail three standard fabrication strategies that are compatible with most materials: PDMS stamps, already described in section 1.3., (section 1.4.1), pick-up using a polymeric membrane (section 1.4.2) and an example of a wet-transfer technique (section 1.4.3). Then, in section 1.4.4, we discuss them altogether, and evaluate the best ways for the preparation of heterostructures.

1.4.1. Pick up and transfer using PDMS stamp.

If the flake that we want to use has been synthesized or deposited on a substrate with which we cannot work, we may need to transfer it to a more appropriate substrate. Such is the case, for example, of the Ag_2Te flake shown in Figure 1.10. It was transferred after its synthesis to a Si substrate, as can be observed in Figure 1.10a. However, to characterize it using transmission electron microscopy (TEM), we need to place them on a suitable substrate, like a carbon membrane on a copper grid, as shown in Figure 1.10b [33]. On the other hand, it is also possible that we have exfoliated on the PDMS stamp, but we need to carry out some specific characterization that cannot be performed on said stamp, such as AFM. In those cases, we need to transfer the flakes to a substrate to perform the characterization, to then pick up and transfer the flakes that we want to use to a final substrate.

PDMS stamps not only are useful for transferring flakes from the blue tape, on which they are first exfoliated, to a substrate, but can also be used for picking up flakes from a substrate and transferring them to a different place. Its advantages compared to other techniques involving a polymer membrane, as the ones described in sections 1.4.2 and 1.4.4, are that it can be done at room

temperature, and that no solvents are needed for the process. This is important since the use of organic solvents may damage the flake, and in every case, they contaminate the surface of the flake with residues. If possible, it is important to select the first substrate taking into consideration the adhesion between it and the flake, to avoid the use of the aforementioned membranes. Useful substrates with low adhesion on which this step generally works are Pyrex or CaF_2 .

For picking up a flake using the PDMS stamp, we need to prepare a clean piece of PDMS. At the delamination system, we will approach the glass slide holding the PDMS stamp to the flake we want to pick up and press down the arm so that the PDMS slowly gets in contact with the flake. Once the PDMS completely covers the flake, we quickly retract the arm to pick up the flake from the substrate. If the process was successful, we now have the flake on the PDMS and can proceed to transfer it to the final substrate.

We move with the arm to the desired area on the final substrate. We proceed as usual, slowly lowering the arm until the stamp touches the substrate. Once contact has been achieved, we wait for a few minutes to let flake accommodate to the substrate. Slightly heating the stage (40°C) may also help in this step. Then, very slowly, we lift the arm to release the flake. If the flake does not stick on the area where we want to transfer it, we can try again repeating this step, applying a bit more force and waiting a few more minutes before releasing. The same strategies for transferring the flake from the PDMS stamp to the substrate described in section 1.3 are also applicable in this case.

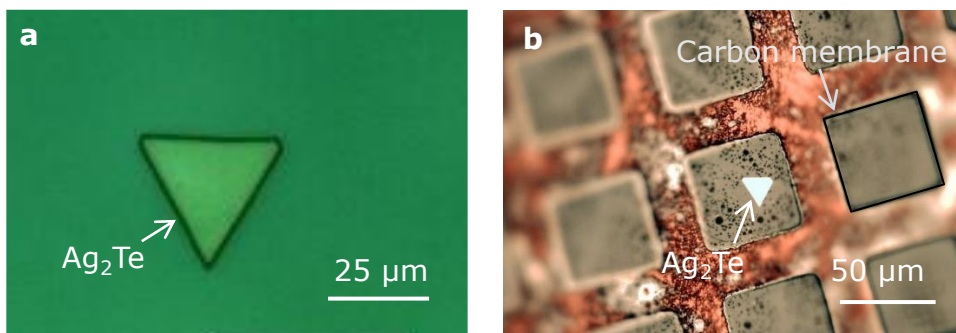


Figure 1.10: Ag_2Te flake transferred from a Si substrate (a) to a carbon TEM membrane (b) using PDMS stamp.

1.4.2. Transfer using a polycarbonate (PC) membrane.

For very thin flakes, using PDMS stamps as pick-up tool will most likely not work. First, the fast pick up will induce a substantial strain which will probably break the flake. Second, the affinity between the flake and the PDMS is not strong enough to be able to successfully pick up the flake. The most used technique for these situations involves the fabrication of a polymer membrane that presents different grades of stickiness as a function of temperature. Here, we review in detail the transfer using the polycarbonate (PC) membrane technique

First, we need to fabricate the membrane that we will use for the transfer process. We prepare a solution, for which we dissolve poly (bisphenol A carbonate) (6% weight – 3.78 g) in chloroform (40 mL) by stirring overnight following the recipe from [34] (473mg/5mL). Then, a drop of the solution is placed on a microscope slide and immediately covered with another microscope glass slide. To get a thin film, we rub one slide against the other, applying some pressure in the process. After this, the two slides are immediately separated by sliding one over the other. In this manner, both slides are covered by a thin film of the solution, that is now left to dry for approximately 15-20 minutes

A polydimethylsiloxane (PDMS) stamp is placed on top of a new glass slide. Using commercial double-sided scotch tape, on which we have prepared a window slightly bigger than the size of the PDMS stamp, we pick up the PC film from the slide. Then, we place it over the new slide, the freestanding film covering the PDMS stamp. The glass slide with the PC-PDMS stamp is now ready to be used for the pick-up and transfer of the flakes.

To perform the pick up process, we work again at the delamination system. The glass slide holding the PC-PDMS stamp is held at the micro-controlled arm, so that we are able to move it gradually, and the substrates will be fixed on the stage. First, after locating the flake that we want to pick up on the substrate, we cover it with the PC-PDMS stamp while the stage is heated up to 90°C. We then approach the arm slowly until the PC membrane is almost touching the substrate. We let the PC-PDMS stamp expand due to the increase

of temperature and watch that it contacts the substrate and covers the flake. We wait for a couple of minutes with the temperature set. In case that we observe that the flake does not adhere to the membrane, the temperature during this step can be increased, until 120°C. The highest the temperature, the more are the chances that we achieve the pick-up. However, we will also be inducing more strain and the chances of creating wrinkles and folds in the flake. An important but not necessary detail is to attempt the pick-up step with the edge of the PC-PDMS stamp, and to only touch the desired flake. In that way, we will pick up the minimum amount of non-wanted flakes possible. After waiting for a few minutes, very slowly retract the slide picking up the flake in the process.

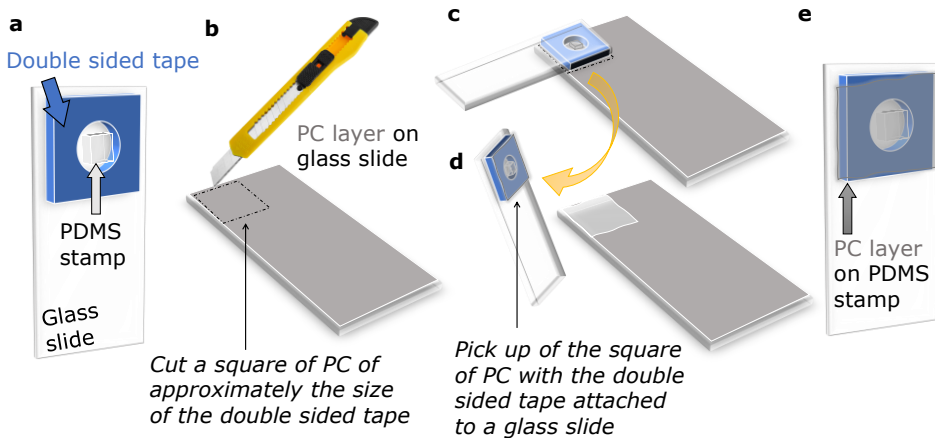


Figure 1.11: Schematics of the preparation of the PC membrane/PDMS stamp. a) schematic of the pick-up process using PC membrane on PDMS stamp; b) optical image of the PC-PDMS stamp on microscope glass slide, to be used for the pick-up technique.

Once the flake is on the PC film, we move the membrane to be on the area of the substrate where we want to place it. We proceed as usual with the alignment, moving the slide down slowly until the flake touches the surface. Then, the heater is set to 180°C (150°C in our system, to avoid damaging the optics of the microscope), so that the PC melts over the substrate. When the temperature is reached, we retract the slide until the PDMS separates from the PC. Finally, when the PDMS has separated, we start to move the slide in the

X direction so the membrane breaks. Once that line is broken, do the same in the Y direction, and then -X and -Y, before removing the slide.

The substrate containing the flake and the melted PC is left to cool down. When at room temperature, it is left for 20 minutes for at least 1 hour (although it can be left overnight to ensure the complete cleaning of the membrane) immersed in chloroform or dichloromethane, that will clean the residues of the melted PC. After that, we cleanse the sample by rinsing it in IPA and drying it with the N₂ gun.

Additional information 1.6.: Tips for the successful pick-up of flakes using PC membrane

- If the controller of the movement of the membrane is too rough and does not allow slow retraction of the membrane, one option is to switch off the heater when you are about to start lifting the flake. The membrane will cool down and retract very slowly, picking up the flake in the process. Once more than half of the flake is lifted, mechanically lift the membrane using the controller, to avoid that the PC gets too cold and the flake sticks back to the substrate. Furthermore, it is possible to know whether you have picked up the flake if it changes color when the membrane (carrying the flake) is lifted from the substrate.

1.4.3. Wet transfer using a PMMA carrying membrane.

The “wet transfer” technique is based on direct exfoliation on a substrate covered with two layers of polymers. The first of these layers is a PVA film, soluble in water. The second layer is a PMMA film on which the flakes will be exfoliated. After the exfoliation step, the substrate with the PVA-PMMA films and the flakes on the PMMA is immersed in water. The PVA layer dissolves, leaving the PMMA layer floating on the surface of the water, as a membrane *carrying* the flakes [35]. Then, we need to fish out this membrane with a spoon and transfer the flake to the final substrate.

We begin by manually cutting Si/SiO₂ (300nm) wafers in big pieces to create the substrates on which we are going to exfoliate. Then we need to spin coat the solutions on said substrates. Poly methyl methacrylate (PMMA) is a polymer commonly used as resist in electron beam lithography, which makes it easy to find in any cleanroom. It is easily cleaned by immersing the samples in acetone for a few hours. Both PMMA and acetone are compatible and commonly used with most of 2D materials during lithography process for sample fabrication, so they can also be used during exfoliation. On the other hand, poly vinyl alcohol (PVA) is a synthetic polymer soluble in water, widely used for different applications. It is commercialized both in pellets and powder, among other possibilities, so we can prepare the solution with the concentration we find more suitable. Having selected these polymers, we can prepare the substrates for exfoliation.

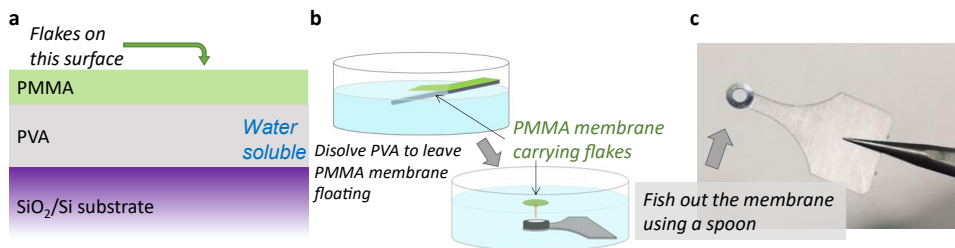


Figure 1.12: PMMA carrying membrane. a) Dipping the silicon substrate with the PMMA-PVA membrane, leaves the PMMA membrane floating on the surface of the water. b) Example of the piece designed for picking up the membrane. c) Schematic of the fishing step.

We first prepare a PVA solution that can be spin coated over a substrate. We prepare a 3% solution by weight of PVA in deionized (DI) water. The PVA is mixed with DI water in a container, sealed and left to spin with a magnetic stirrer at room temperature. After several hours, and depending on the amount that is being prepared, the solution is ready. We then need to spin coat a substrate with both polymers, following the parameters shown in Table 1.1.

	Spinning	Time	Acceleration	Baking
PVA	3500 rpm	120 s	1000 rpm/s	130°C (300 s)
PMMA	2200 rpm	120 s	1000 rpm/s	130°C (300 s)

Table 1.1: Spin coating parameters for the preparation of PVA/PMMA substrates

As in the usual exfoliation process, we first need to prepare the blue tape by putting some material on it, and successively peeling it off with clean pieces of tape. Generally, the materials do not adhere easily to the PMMA, so the recommendation for a successful transfer to the substrate is to leave a good number of big pieces of material on the blue tape. They should be big enough to be clearly seen by the bare eye. Once the blue tape is ready, we place on the PMMA-coated substrate, and gently press down with the finger. It is important not to rub, as it would result in small, broken flakes. Then, we peel the tape from the substrate very slowly, to avoid ripping the PMMA layer.

The next step is to check the substrate under the optical microscope. If there is a flake on the substrate that fits the requirements, the best way to proceed is, having it centered through the oculars, set the 10x objective and the light to the maximum. The circle of light with the flake in the middle is then big enough to comfortably draw a circle around it with a sharp tweezer. Once it is visible, it is recommended to scratch the circle more once the substrate is taken out of the optical microscope, to ensure that the polymers are broken around the area of interest.

In the next step we need to detach the PMMA membrane with the flake on top from the substrate. This step is achieved by immersing the substrate in a recipient filled with deionized water. To make sure that the process is successful, it is important to first dissolve the PVA film. For this purpose, we will fill the scratched circle with water using a tweezer. After wetting the tip of the tweezer by dipping it in water, gently retrace the circle until a water fence surrounding it is formed. Said water circle will start to shrink, as water begins to solve the PVA and flow under the PMMA. Some wrinkles can be seen when the PMMA starts to go up but is not completely detached. If the process stops, repeat the step until the PVA under the PMMA circle is dissolved. Once that happens, the PMMA circle will stay floating on top of the water drop. The substrate can

be then slowly immersed in water, with an angle, so that the PMMA membrane stays floating on the surface (Figure 1.12a). The moment the water drop on top of the substrate touches the water, the membrane will detach and float immediately. We remove the Si substrate and leave it outside the water (otherwise the PMMA that remains on the substrate will detach and can merge with the circled membrane).

Using a ring-shaped holder (“spoon”, Figure 1.12b), we can fish the membrane. With the membrane floating on top of the water surface, take the spoon with the flat tip tweezers and immerse it into the water, under the membrane (Figure 1.12c). We need to approach it gently, from bottom to top, and make sure that the membrane is centered above the ring (covering all the area). Only then, we can proceed to carefully catch it. The membrane should stay tense, free-standing on the center of the ring. If there are any places where the membrane does not touch the edges of the metal ring, we can immerse the holder again into the water to detach the PMMA and try again. Finally, we let it dry for a couple of hours before proceeding to the transfer process.

Finally, we need to transfer the flakes from the membrane to the final substrate. As usual, we approach the membrane to the substrate. When we are close to achieving contact, some lines will appear on the membrane (Figure 1.13.a). Then, we set the temperature to 80°C, and let the membrane expand to the substrate (Figure 1.13.b,c). Since SiO₂ presents less adhesion to the flakes than most of the polymers, transferring the material to the substrate as we did with the PDMS stamp will not work. There are two different strategies one can follow. On the one hand, once we have achieved contact on the substrate, we can melt the PMMA on the substrate (Figure 1.13.d) by setting the temperature at 160°C and operating as for the PC membrane. The piece of PMMA containing the flake will stay on the substrate, but it can easily be cleaned by immersing the sample in acetone and then rinsing in IPA. The other option is to transfer on top of other material, such as hBN, as in the examples shown in Figure 1.13.e,f.

The PMMA wet transfer technique is an example of the capabilities of the two polymers involved. It is not widely used, since there are more powerful

techniques that obtain similar or even better results. However, due to its compatibility with 2D materials, PMMA and PVA are explored for different fabrication processes, such as pick up and transfer of CVD grown materials [29] or pick-up strategies similar to the PC membrane technique [36,37].

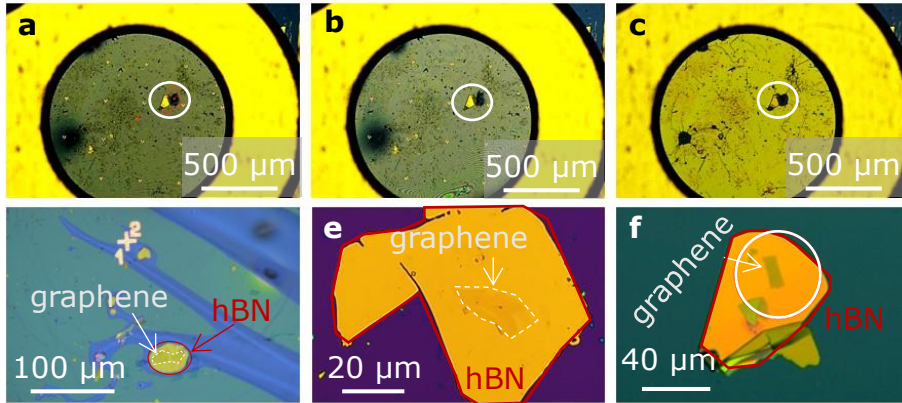


Figure 1.13: Transfer process using PMMA membrane. a-c) Changes of the membrane close to the substrate during ~ 20 minutes at 80°C . The white line circles the flake to be transferred, the final result of the transfer shown in (f). d) PMMA membrane melted on a Si/SiO₂ substrate after the transfer. e, f) graphene flakes transferred on hBN using the PMMA membrane

Additional information 1.7.: Tips for handling the PMMA membrane

- Fix the substrate to a glass slide using double sided tape, so when it is time to draw the circle with the sharp tweezers under the light of the microscope, it will not move.
- It is easier to spot the floating membrane if the petri dish is placed on a dark surface.
- It is possible to obtain more than one flake per substrate if they are sufficiently apart to draw more than one circle and to dip the substrate in water to detach them one by one.
- To calibrate the tilt of the arm, we place the holder on the arm and center it in the microscope screen, out of focus. If the ring is flat, a dark

inner ring will appear inside the metal ring, concentric to it. If the ring is not flat, this darker shadow will be more elliptical. We adjust the tilt until it is correct.

- Note that membranes prepared using PMMA A4 are more robust than the ones with A2, since they are thicker. However, identification of thin flakes is much easier in the latter, due to the difference in the thickness. Good alignment of the holder before transferring is key to achieve the stamping of the membrane and thus, of the flakes. If the membrane sticks to the substrate, dissolve it in acetone while shaking with a tweezer.

1.4.4. Fabrication of heterostructures of 2D materials

Since the experimental obtention of the monolayers from 2D materials, one of the most attractive ideas was to combine them as building blocks to create heterostructures. These stacks of materials provide a versatile platform to tune the properties of the materials and study fundamental effects and novel applications [38–41]. The techniques described in the previous sections are only some of the many possibilities that are being exploited nowadays.

Fabrication of heterostructures was already commented on section 1.4.1, since we can use PDMS stamps to transfer several flakes in consecutive steps, one on top of the other. In the case that the flakes do not have enough optical contrast for their identification on PDMS, we need to develop some strategy to pick up the flake from a substrate, and from the heterostructure on a membrane. As commented on 1.4.2., the pick-up and transfer using a PC membrane is a common technique for this fabrication, with high success rate. In a similar way to this technique, we can use other polymers to prepare the membranes, with similar elastic and adhesion properties, but which present different characteristics, such as critical temperatures or solvents required for cleaning, that are compatible with materials. Such is the case of polycaprolactone (PCL) or nail polish [42,43], that can also be used for pick up and transfer of 2D materials, and the fabrication of heterostructures (stacks). The process, depicted

in Figure 1.15, is the same as the one described for PC: we prepare the stamps, and then proceed to successively pick up the flakes by increasing the temperature each time we need to pick up the flake. Then, as shown in Figure 1.16, we release the stack on a substrate by melting the membrane. For both these polymers, the processes take place at lower temperatures, between 40 and 60°C, whereas PC require temperatures from 100 to 150°C. Note that to address the compatibility between a method and a material we should not only consider the fabrication temperature, but also the solvent that we will need for cleaning the membrane.

Another important step for the fabrication of heterostructures is the annealing of the transferred flakes. After the preparation of the stack and its transfer to the final substrate, the heterostructures are usually annealed in vacuum for an hour at 300°C. This helps the accommodation of the flakes in the heterostructure, removes some air bubbles that might have formed during the stacking, and removes some dirt and residues [44]. An example of this effect for an MoS₂ flake is shown in Figure 1.17. Of course, this step can only be done on materials that are stable at high temperatures, but we should also consider the substrate and possible future fabrication steps. For instance, this annealing process might also induce defects on the SiO₂ layer of the commercial Si/SiO₂ substrates that we use for fabrication, affecting the performance of the future device [45,46]. It can also affect the properties of the material or the stack, such as its photoluminescence [47] or tunneling magnetoresistance [48].

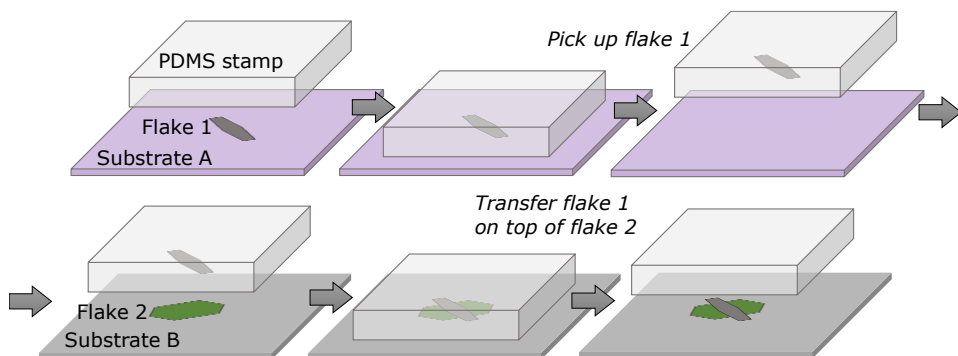


Figure 1.14: Fabrication of heterostructures using a PDMS stamp.

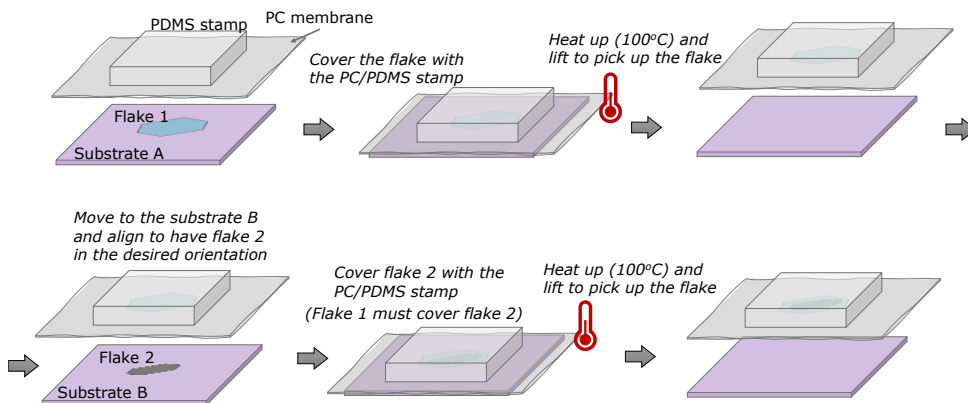


Figure 1.15: Fabrication of heterostructures using PC membrane. Successive pick-ups can be repeated following these steps as many times as needed.

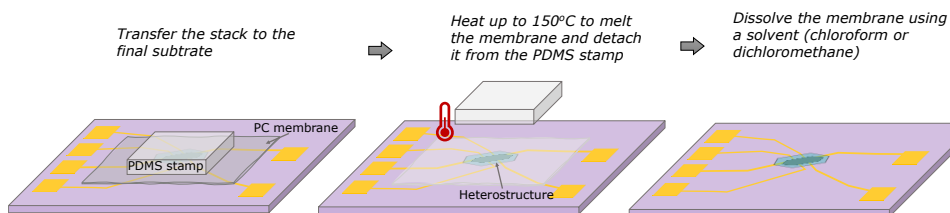


Figure 1.16: Transfer of a heterostructure fabricated by pick up with a PC membrane on a pre-pattern substrate. After the preparation of the heterostructure as shown in Figure 1.15, we transfer it to its final substrate. For example, it can be transferred on top of electrical contacts pre patterned on a substrate, as shown in this schematic.

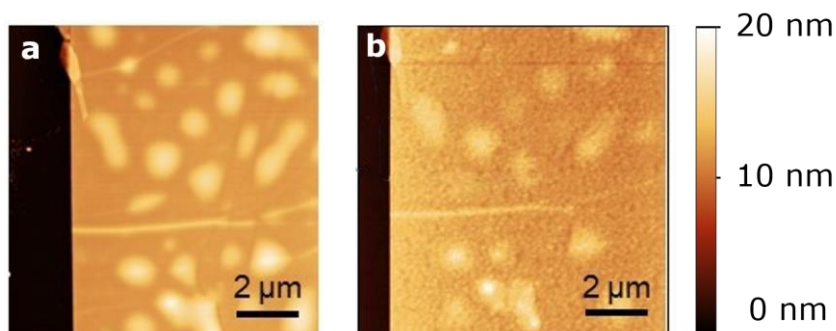


Figure 1.17: AFM profile of a MoS₂ flake. a) MoS₂ flake after being transferred to a SiC substrate using a PDMS stamp. b) Same area of the MoS₂ flake shown in (a), after annealing in vacuum at 300°C for an hour, resulting in a reduction of the bubbles.

1.5. Conclusions

In this chapter, we explored various techniques and strategies for the fabrication of samples and van der Waals heterostructures. We began by discussing the fundamental method of exfoliation, which involves the successive peeling of layered materials using blue tape. This process allows us to obtain thin flakes and even monolayers of 2D materials from bulk crystals. To determine the thickness of these layers, we rely on optical contrast, AFM measurements, and Raman spectroscopy, the latter being particularly useful for identifying monolayers and bilayers of specific materials, like graphene and MoS₂.

We examined next the transfer of flakes onto substrates, a crucial step in sample fabrication and heterostructure formation. One approach involves using viscoelastic stamps made of polydimethylsiloxane (PDMS). These stamps enable the transfer of flakes from the blue tape to a final substrate and offer the advantage of optical inspection due to their translucency, allowing for color contrast analysis of different material thicknesses. However, due to their viscoelastic properties, measurements such as AFM or profilometry cannot be performed directly on the PDMS stamp's surface. Note that while PDMS stamps are suitable for creating heterostructures by sequentially transferring flakes, we should always consider the contamination at the interface between layers.

On the other hand, we explored membrane-based strategies, particularly the use of a PC membrane for picking up flakes and forming heterostructures with clean interfaces. Although this method ensures minimal contamination, it often requires high temperatures and the use of solvents, which may potentially damage the flakes. Furthermore, the cleaning process of the membrane using solvents can result in the accumulation of residues on the upper surface of the heterostructure.

In conclusion, this chapter provided an overview of key techniques employed in sample fabrication, including exfoliation, transfer methods using PDMS stamps and PC membranes, and the formation of van der Waals

heterostructures. These techniques serve as fundamental tools in the realm of 2D material research, enabling the fabrication of samples for the exploration of their unique properties and potential applications.

2 • Nanofabrication

Nanofabrication is the term used to describe the different techniques to design and prepare devices or structures with features that go down to the nanometric scale [49]. It groups different strategies, approaches, and tools, that we can combine to prepare our final samples. In this chapter, we review and comment on some of the procedures that are generally used for nanofabrication, and that were used during the development of this thesis, as summarized in Figure 2.1.

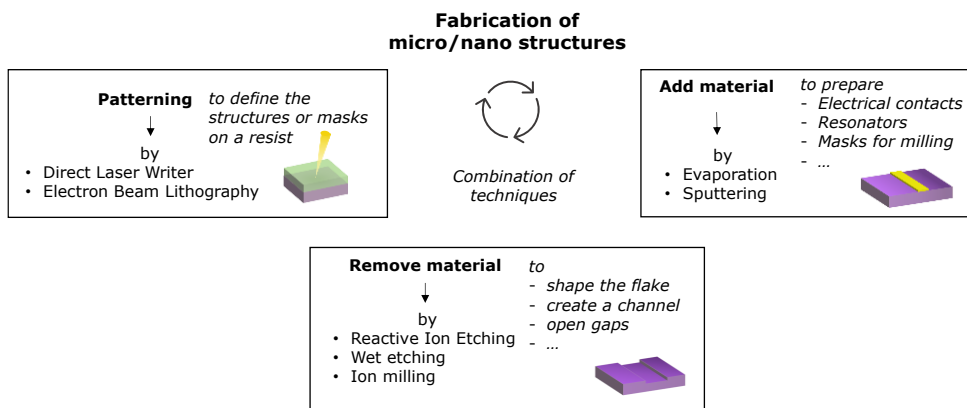


Figure 2.1: Summary of fabrication tools and techniques employed during the development of this thesis.

Additional information 2.1.: Nanofabrication in cleanrooms

- All the processes and techniques described in this chapter were performed inside of a cleanroom [50], i.e. a controlled environment where temperature, humidity, airflow patterns and air pressure conditions are kept at stable values, to ensure optimal conditions for the processes that take place in it. Cleanrooms continuously filter the air using high-efficiency particulate (HEPA) filters, to minimize the presence of airborne microparticles, dust or other contaminants that, due to their size, could potentially impact sensitive processes.
- Cleanrooms are classified based on their level of cleanliness, which is determined by the maximum allowable number of particles per cubic meter of air at specified particle sizes. The classification system most used is ISO 14644⁴, based on particle concentration and consisting on nine classes, ranging from ISO Class 1 (the cleanest) to ISO Class 9 (the least clean). Another classification is the Federal Standard 209E⁵, commonly used before the introduction of ISO 14644 and that categorized cleanrooms based on the maximum allowable number of particles per cubic foot of air at a specified particle size. Both classifications are shown in Table 2.1.

ISO 14644	Federal Standard 209E
ISO Class 1: 0.1 μm or smaller	
ISO Class 2: 0.2 μm or smaller	
ISO Class 3: 0.3 μm or smaller	Class 1: ≤1 particle/ft ³
ISO Class 4: 0.5 μm or smaller	Class 10: ≤10 particles/ft ³
ISO Class 5: 1 μm or smaller	Class 100: ≤100 particles/ft ³
ISO Class 6: 5 μm or smaller	Class 1,000: ≤1,000 particles/ft ³
ISO Class 7: 10 μm or smaller	Class 10,000: ≤10,000 particles/ft ³
ISO Class 8: 20 μm or smaller	
ISO Class 9: N/A (not specified)	

Table 2.1.: Cleanroom classification

⁴ ISO Cleanroom classification: <https://www.iso.org/standard/53394.html>

⁵ Federal Standard Cleanroom Classification: http://everyspec.com/FED-STD/FED-STD-209E_21739/

2.1. Defining a pattern by lithography

Generally, we first need to define a certain structure on the sample. In our specific cases, we might need for instance to prepare electrical contacts to measure the electrical properties of a material, or to create a mask to protect a flake during the etching step. In all those cases, we use lithography, the technique of creating or transferring a pattern to a substrate [51]. In the development of this thesis project, we have focused mostly on the use of direct laser writing (DLW) [52–54] and electron beam lithography (EBL) [55,56], techniques that use a beam of photons or electrons, respectively, to define a pattern on a resist. Resists are solutions of polymers are sensitive to that radiation (see section 2.1.3 for more details about resists for lithography). After the exposure step, and, by some other process, we transfer said pattern to the substrate. In this section, we introduce first the two types of lithography that we used, i.e., DLW and EBL. Then, we describe in detail the process for the fabrication of a sample, from the selection of the most appropriate resist and how to cover the sample with it, to the patterning of the sample and developing of the resist to reveal the design.

2.1.1. Direct Laser Writing (DWL) lithography

In general, optical lithography techniques use visible light to expose a pattern on a photo resist. Typically, they require the use of a shadow mask to define the pattern, and a lamp as a light source [57]. The light is shined through the shadow mask, projecting the design onto the resist. The mask is not required at the DLW, which uses a laser of 375 nm – 405 nm to directly expose the resist [58,59]. The laser beam goes through an optical path formed by modulators and mirrors, and is focused on the surface of the sample using a pattern generator, as shown in Figure 2.2. Furthermore, DLW can write relatively big areas in short times, i.e. square millimeters in a few minutes.

When doing lithography, it is important to consider the resolution limits of the equipment. With a standard DLW set up, the minimum feature one can

achieve with DLW is approximately 500 nm, given the wavelength of the laser beam (405 nm in our system [60]) and the Rayleigh criterium [61]. This limit can be pushed down using specialized polymeric resists, as well as sub-diffraction limit strategies [62].

In general, we can use DLW to fabricate patterns on any kind of substrate, but we might have problems when using too small (5 mm lateral size, or smaller) or transparent substrates. In both cases, the issues will come from difficulties in the focusing process. Small substrates need to be perfectly centered to focus on them. For transparent substrates, the system is not able to distinguish the surface when trying to focus automatically. The way of solving these issues is to focus manually, trying to find the edge of the sample to distinguish some defects that we can see and focus on. In both cases, it is important to keep the focus fixed during the patterning step, and not letting the system readjust it while writing.

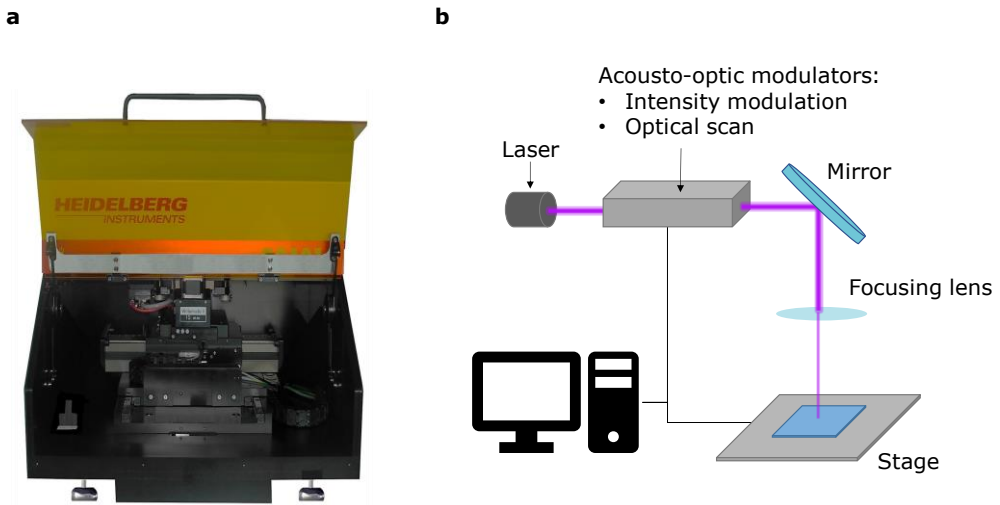


Figure 2.2: DLW system from Heidelberg instruments, as the one used in the development of this thesis. a) General view of a DLW equipment as the one at CIC nanoGUNE [60]. b) Schematics of a DLW system

2.1.2. Electron Beam Lithography (EBL)

As DLW, EBL is based on patterning a sensitive polymer by focusing a beam on the surface of the sample [55,56]. EBL uses an electron beam, that is generated in an electron gun by heating a filament, generally tungsten, and passes through electromagnetic lenses that collimate and direct it, correct the astigmatism, and focus and deflect the beam on the sample. An aperture determines the beam current, and a beam blanker acts as a shutter during the writing step. The basic elements of an EBL system are depicted in Figure 2.3a.

The sample is mounted on a mechanical stage, that loads the sample inside the equipment and moves it to the desired positions. The area that we are able to write is called write field, WF, and is determined by the beam deflector, that moves the beam to scan the surface of the sample. Close to the edges of the WF, the beam gets distorted, and the pattern may be affected. The solution to this issue is to write using several, smaller, WFs. Thanks to an optical interferometer that accurately measures the position of the stage, the system is able to correct the stitching error between adjacent WFs, overall increasing the size of the working area. Similar to the DLW, the beam blanker and pattern generator work together to direct the electron beam on the surface of the sample and create the designed pattern on the resist. In the case of EBL, we can work on insulating, semiconductors, but it is preferable to work on conductive surfaces to avoid charge accumulation that overexposes the resist and destroys the patterns.

The minimum feature that can be patterned using state of the art EBL systems is a few nanometers. The resolution limit of the EBL system used during this thesis, shown in Figure 2.3b, is approximately 10 nm. The resolution limit of an EBL system is given by different factors, that include the energy of the beam, the spot size, proximity effects or the properties of the resist. All these factors are defined, and their influence described in more detail further in this chapter, in section 2.1.5.

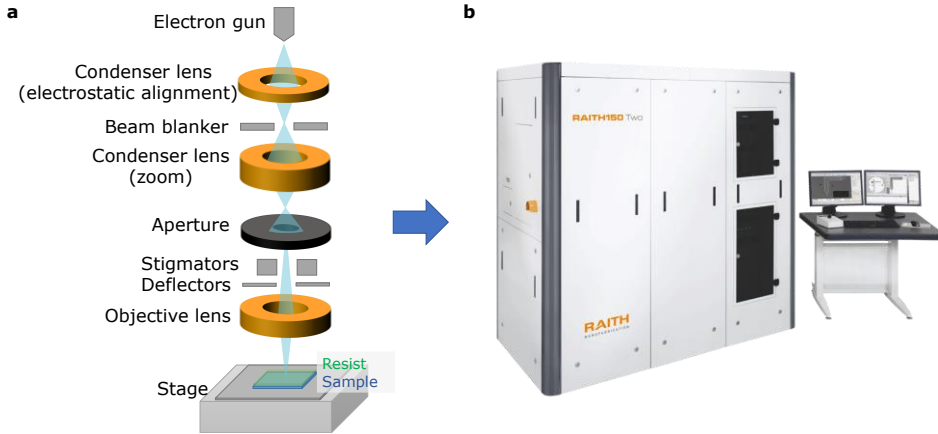


Figure 2.3: Electron Beam Lithography. a) Schematics of the basic elements of the EBL system. The electron beam is generated at the electron gun and passes a series of components until it reaches the sample. b) Commercial EBL Raith 150TWO equipment, as the one available at CIC nanoGUNE. Picture taken from [63].

2.1.3. Polymeric resists for lithography

When patterning a sample using DLW or EBL, we need to select the resist that best fits the requirements of the process. Resists are formulated for a lithography technique or even a particular purpose (i.e., high resolution or conductive resists), and they are often classified in two groups: positive tone or negative tone resists [64]. In this section, we are going to describe some details of each type that are significant to the fabrication process.

The polymers in the resist change their physicochemical properties upon exposure. In the case of positive resists, exposed areas become soluble in the developing solution, and will be removed in the development step. Negative tone resists, however, behave in the opposite way. When the polymeric chains are exposed to radiation, they link together, conforming stronger chemical bonds. During the development process, these exposed areas will remain, while the non-exposed parts of the resist will be removed during development. The final profile of the gaps will be determined by this behavior, so, when selecting a resist for

our fabrication process, we should consider not only the total area to write, but also the cut profile that is obtained. Interestingly, the profile obtained after exposure for different resists also depends on the lithography technique. In the case of EBL, the resists are more exposed at the surface in contact with the substrate, due to the scattering of electrons from the substrate. However, for optical lithography, DLW, the resist is more exposed in the upper surface since light fades as it goes into the resist layer. A schematic exemplifying this effect is shown in Figure 2.4.

When designing and optimizing the process, it is important to consider the final profile that we will obtain. Resist masks with an undercut profile are more suitable for lift-off steps ⁶, since the formation of a gap between the deposited metal and the sidewall of the resist allows to better dissolve the resist, resulting in sharper, better defined edges for the final structure. In this regard, also the thickness of the resist plays a key role in the success of a lift-off step: approximately, the thickness of the deposited metal should stay below half of the resist thickness.

With all these factors in mind, we can now evaluate which resist is more suitable for our fabrication process. For EBL, the most common resist is poly methyl methacrylate (PMMA), a commercially available positive resist. Negative resists for EBL can also be useful depending on the design of the mask that we want to write, since it may significantly reduce the writing time. However, they are less stable over time, and we would need to evaluate the dose required for our design every time we use the resist. These evaluations are commonly referred to as dose tests. In addition to the standard resists that we have just introduced, some more sensitive resists, commonly known as high resolution, were developed to push the limits of the lithography techniques [66–68].

⁶ Lift-off is the process during which we remove the lithography mask and the excess of material after metal deposition [65]. It will be described in detail farther in this chapter.

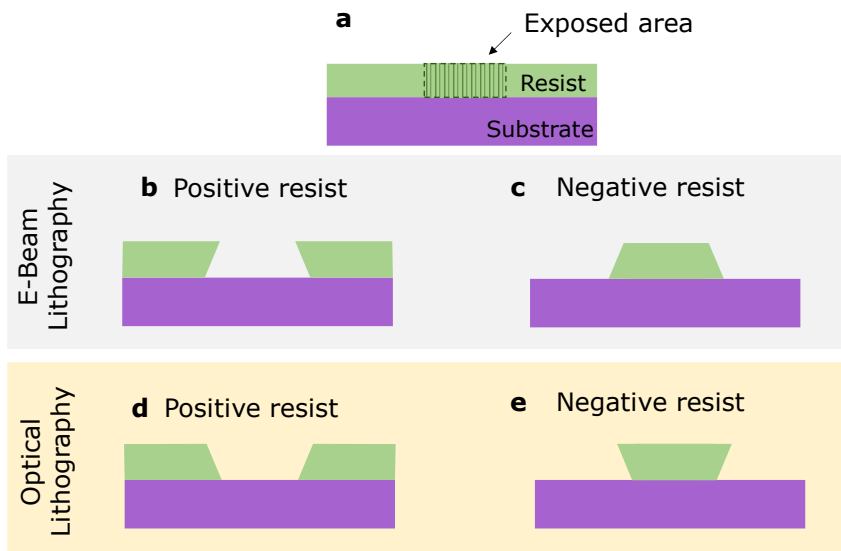


Figure 2.4: Resists profile before and after exposure in EBL (b,c) and optical lithography (d,e). a) Resist layer before exposure by any of the techniques. b) Positive resist for EBL after exposure and development, creating an undercut profile. c) Negative resist for EBL after exposure and development, suitable for etching masks. d) Positive resist for optical lithography after exposure and development. e) Profile of a negative resist for optical lithography after exposure and development.

Additional information 2.2.: Details about PMMA

- When buying PMMA, we find that the name is followed by a series numbers and letters that indicate some specifications of the resist, *PMMA (xxx)K (i)(x)*, where (x) corresponds to numbers and (i) can stand for "A" or "C".
- The first three numbers, (xxx)K, correspond to the molecular weight of the polymers in the solution. The sensitivity of the resists decreases with higher numbers, meaning that we will need more energy to write the same features for PMMA with higher molecular weights. In order to obtain smaller features, we will use higher molecular weights, since these resists will be less sensitive to proximity effects or overexposures.

- The last part of the name, (i)(x), indicates the type of solvent and percentage with which the solution is prepared. For instance, “A4” means that we have a 4% solution prepared in anisole, whereas “C6” stands for 6% in chloroform. This data is relevant for the final thickness of the resist layer: the more concentrated the solution is, the thicker the final layer using same spin coating parameters. The evolution of the thickness for different percentage as a function of the spin coating speed is presented in Table 2.2. Finally, it is also important to consider the compatibility of the solvent with the materials that we are using.

Reversal image resists

For optical lithography, and, in particular, DLW, the writing time is not so relevant, since the process is generally faster than at the EBL. However, we have already commented on the need of an undercut profile if we want to do a lift-off process. Unfortunately, as mentioned, negative resists tend to be less stable than positive resists. They also present adhesion problems, and some of the smaller structures are sometimes removed in the developing step. A way of addressing this issue is using the known as *reversal-image* resists. These resists can be used as positive resist, but also behave as negative if we add some extra steps to the process. After exposure of the pattern, we need to do a flood exposure over the whole sample, followed by a soft bake on a pre-heated hot plate. This will over-dose the areas that we have previously patterned and harden the resist. The areas that were not exposed during the lithography and now received some energy will behave as exposed and will be removed with the developer. With this process, we will create an undercut profile, suitable for the lift-off step on the sample [69].

2.1.4. Spin coating step

Once we have selected the best resist for our sample and design, we need to homogeneously cover the substrate with it by spin coating. We first fix the

sample on a rotating stage using a vacuum hole (Figure 2.5.a). Once the sample is fixed (Figure 2.5.b), we drop cast a droplet of resist on the sample (Figure 2.5.c), and let it spread homogeneously over the surface with the help of the rotation (Figure 2.5.d). Then, by keeping the speed constant, we remove the excess of resist from the substrate (Figure 2.5.e). When the spinning step is finished, the sample is often left on a warm hot plate to help evaporate the solvents and cure the resist (Figure 2.5.f). The parameters for the successive steps of the procedure differ for each type of substrate and resist, although the steps described above are the same in every case.

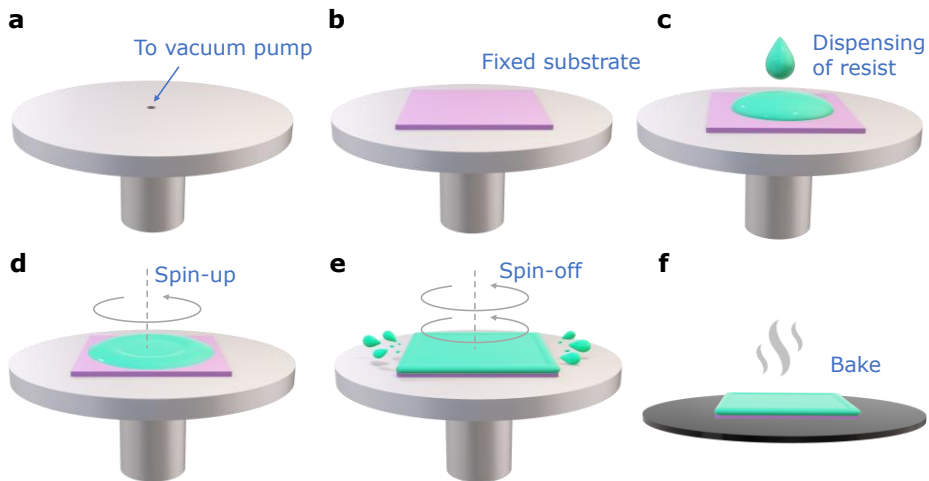


Figure 2.5: Schematics of the spin coating cycle. a) Typical spin coating stage. The hole in the middle of the stage connects to a vacuum line to keep the substrate fixed on the stage during the spinning steps. b) The substrate should be approximately centered on the stage for successful spin coating. c) Deposit some drops of resist to cover the surface of the substrate. d) In the acceleration or spin-up step, the resist homogeneously covers the substrate. e) The excess of resist is removed during the spin-off step; f) the remaining solvent is evaporated during a baking step.

Some substrates may present low adhesion to the resist or inhomogeneities on the surface after the spin coating process. First, we always will need to clean the substrate. The standard substrate cleaning procedure is as follows:

- 5 minutes immersion in acetone at room temperature in an ultrasonic bath (optional)
- 5 minutes immersion in isopropanol (IPA) at room temperature in an ultrasonic bath (optional).

After these two steps, we can directly dry the substrate by blowing N_2 on them. However, it might be that we need to take some additional steps:

- If after the acetone-IPA- N_2 cleaning we still observe some residues or dirt on the surface of the substrate, we can further clean it using O_2 plasma at 100 W for 5 minutes. This will also remove any humidity remains from the surface. For EBL resists this step is also helpful, as the presence of humidity normally causes problems in their adhesion.
- Regarding the presence of water, if the substrates would be damaged by exposure to the O_2 plasma, we can always remove the residual humidity by baking the substrate for a few minutes. The standard recipe is 120-160°C for 5 minutes, but we can also bake it for longer at lower temperatures.
- As mentioned, EBL resists stick in general well to Si/SiO₂ substrates. However, it is common to use hexamethyldisilazane (HMDS) to improve the adhesion of the resist to the substrate, particularly for optical lithography. HMDS reacts on the surface of the Si/SiO₂ substrate, forming a monolayer of trimethylsilano (TMSiOH), which acts as an adhesion promoter for the resist [70].
- Finally, there are some materials, such as CaF₂, that present low affinity with the resists, even after trying all these strategies. The solution for these, is sometimes to generate some residues on its surface before spin coating. We can spin coat the surface with the resist that we want to use, and immediately clean the substrate in acetone for a few minutes. This will remove most of the resist but will leave some residues on the surface, that will promote the subsequent adhesion of the resist. We dry the acetone with N_2 , without rinsing the sample in IPA, and then proceed to the actual spin coating step.

Spin coating protocols for EBL: double layer technique

The most commonly used resist for EBL is PMMA. As mentioned, thickness and profile play an important role in the definition of the structures. One of the standard uses of EBL in nanotechnology is the fabrication of electrical contacts and devices, combining the lithography to define the electrical contacts with the evaporation of the metals that will form them. For this purpose, we need to create a T-shape profile on the resist, which will prevent the metal to adhere to the resist, at the same time that it allows the acetone to flow between the structures and the wall of resist, to better dissolve it (see section 2.2 for more details regarding the process of metallization and lift-off). The evolution of the thickness of the PMMA resists used in the double layer technique with the spin coating speed are shown in Table 2.2. As can be seen in these graphs, the thinnest thickness of PMMA is achieved with spin coating speeds of 4000 rpm, and keeping this speed for a minute is enough to obtain an homogeneous layer. The acceleration for reaching the spin coating spin will affect the final thickness and characteristics of the layer. It has to be fast to completely cover the substrate before the evaporation of the solvents, but at the same time, an excessive acceleration might lead to the formation of defects on the layer. For standard recipes, we chose an acceleration speed of 1000 rpms. Finally, the optimum baking temperature of the resist is provided by the manufacturer, and it depends on the different solvents and polymers composing the resist. In the case of PMMA, we bake each layer for 90 s at 180°C. For clarity, the parameters for the spin coating and baking of double layer of PMMA are summarized in Table 2.3.

Additional information 2.3.: Some tips about spin coating

- If the sample cannot be heated up to the recommended temperatures, it can be baked for longer times at lower temperature, or simply be left to evaporate the solvents at room temperature. In the latter case, it should take a few hours, but it is recommended to leave it for a day to make sure no solvents remain in the resist layer.

- When spin coating more than one layer or samples, it is important to clean the stage after every coating. Firstly, because it stains the back of the sample and can prevent proper fixation to the stage, and secondly, because the accumulation of residues below the sample might affect the homogeneity of consecutive layers.
- Finally, do not drop cast more resist than necessary to cover the surface of the sample. To give an estimation of the amount of resist required, a 10x10 mm chip will be covered with 50 μL of resist, whereas for 5x5 mm chips it is enough with a single drop from the pipette ($<10 \mu\text{L}$).

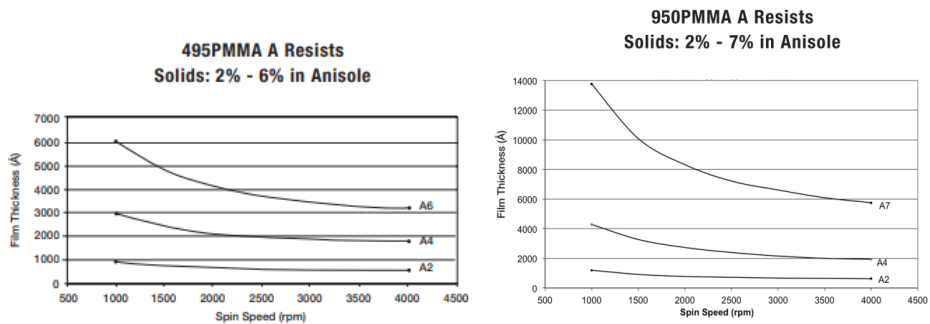


Table 2.2: Evolution of thickness with spin coating speed of a) PMMA 495K in anisole; b) PMMA 950K in anisole.

	Resist	Acceleration	Speed	Time	Bake	Time
Double layer	PMMA 495K A4	1000 rpms	4000 rpm	60 s	180°C	90 s
	PMMA 950K A2	1000 rpms	4000 rpm	60 s	180°C	90 s

Table 2.3: Recipe for spin coating a double layer of PMMA.

Conductive layer for insulating substrates.

When patterning on insulating substrates at the EBL, the task of focusing might be challenging, due to the accumulation of charge and consequent burning of the resist. To avoid this, it is helpful to have a conductive layer on top of the resists.

There are two different approaches that one can follow to create the conductive layer. On the one hand, we can use a conductive resist that we can spin coat over our original resist, but we need to consider that it will add some thickness to the sensitive layer. Another option is to deposit a thin film of gold, of about 2 nm of thickness. The gold layer is thin enough that we can pattern the resist below it, while not affecting the exposure parameters or the resolution of the lithography. Moreover, the gold will easily burn when the beam is properly focused, making it easier to adjust the focus on the surface. In both cases, we will need to remove the conductive layer before the developing step. Details for the deposition and removal of the gold layer are presented in Table 2.4.

Equipment	Material	Nominal thickness (nm)	Rate (Å/s)	Removal
Tabletop sputter	Au	2.3	0.6	<ul style="list-style-type: none"> • Gold etchant (5-10s) • Rinse in DI water (twice) • Rinse in IPA

Table 2.4: Recipe for the deposition of Au conductive layer for EBL on insulating substrates

2.1.5. Patterning a sample using EBL

In this section, we are going to review the most important parameters for the patterning step at the EBL. After following the protocol for loading, focusing, and aligning the sample, we are almost ready to start patterning. However, first we need to understand the importance of each tunable parameter and which value is adequate for our sample and design. The goal is to achieve a spot size, i.e., the diameter that the beam has when it is focused on the resist, smaller than our smallest feature (see Figure 2.6a). For that purpose, we can modify:

- Acceleration voltage: is the bias that we apply in the electron column to accelerate the electrons. It is proportional to the energy with which the electrons arrive to the sample and interact with the resist.
- Aperture: is the whole through which the beam of electrons passes on its way to the sample. It relates to the beam current I , defined as the charge q that flows during a certain time t .
- Dose: is the amount of charge that the resist receives per unit area. It comes from the balance between the beam current, the number of points that constitute the total area under exposure, and the time that the beam takes to irradiate each spot (i.e., the dwell time). By fixing the dose, and adjusting the dwell time, we are able to optimize the fabrication of the structures. Importantly, the actual dose that the resist receives is different from the nominal, established by the user dose, due to the irradiation of the resist with secondary electrons. This results in the proximity effect, that will be discussed further in the text.

Other parameters that can help to optimize the recipe for the structure are:

- Step size: is the distance between consecutive points during the writing step. It will play a role in the writing times, as well as for the definition of very small features. One should always consider the size of the spot to, accordingly, determine the required step. The definition of the step size will determine the value of the dwell time. For example, for an area, the dose can be calculated according to:

$$\text{Area Dose} = \frac{\text{Beam Current} \cdot \text{Area Dwell Time}}{\text{Step Size} \cdot \text{Line Spacing}} \quad [\mu\text{C}/\text{cm}^2] \quad (1)$$

Where the Line Spacing is the distance between the consecutive lines traced by the beam to define the pattern. Therefore, for a certain current, there is only a combination of step size, dwell time, and line spacing that gives the required area dose. This is normally calculated by the EBL software, as shown in Figure 2.6.b.

- Working distance: is the gap between the end of the beam gun and the substrate. However, the beam slightly spreads over the distance. Thus, the closer we work to the gun, the smaller the spot size that we can achieve.

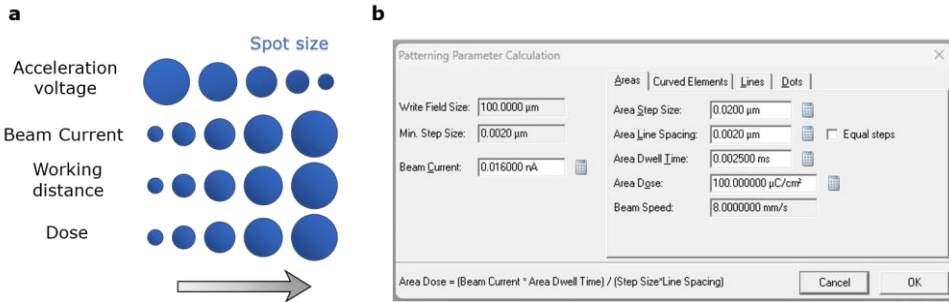


Figure 2.6: Parameters to consider during EBL process. a) Influence of the tunable parameters on the minimum achievable spot size. b) Calculator of parameters in an EBL software from RAITH company, employed during the development of this thesis.

Proximity effect, dose test and dose corrections

When writing a pattern in EBL, we should always consider that the dimensions of the design that we have prepared will turn out slightly different after the lithography step. The emission of secondary electrons that reach the resist will distort our design, making, for instance, some of the smallest features being exposed to turn out bigger than designed. This phenomenon is known as proximity effect [71]. One way to reduce it is by selecting higher acceleration voltages. More energetic electrons penetrate deeper into the substrate, and the resulting secondary electrons will be less likely to reach the resist, as shown in Figure 2.7a, although there is also a dependence on the type of substrate that we use. Although less pronounced for higher voltages, there will always be a proximity effect forming from these secondary electrons, and, therefore, we always need to perform a dose test to adequate the design to the outcome.

The most effective way of performing a dose test is to prepare a two-dimensional array of the structures that we want to fabricate. On one axis, we can progressively change the dose, while on the second, we can modify the dimensions. In this way, covering a wide range of doses and sizes, from too little to excessive, we will find our optimal conditions (Figure 2.7b). Then, we check which combination results in the aimed dimensions, and do not show signs of under or over dosage.

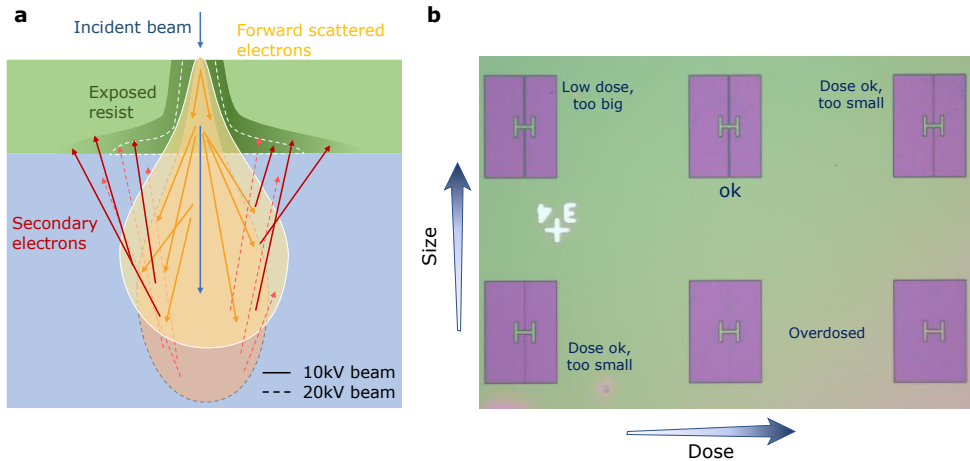


Figure 2.7: Proximity effect and dose tests for optimizing the fabrication using EBL. a) Schematics of the influence of backscattered electrons on the exposure of the resist. b) Dose test performed on PMMA for the fabrication of a THz resonator. The critical part of the design is the vertical line that separates the pattern into two different parts, and that needs to be 500 nm wide for several micrometers. We need to create this line by exposing the surrounding areas. Overdose leads to the over writing of this line due to proximity effect. By slightly lowering the dose and widening the nominal width of the line, we match the aimed design.

Another issue that we might face when designing highly dense patterns, is the formation of a cumulative charge in the center of the design, as in the example shown in Figure 2.8. Here, we wanted to prepare an arrays of ribbons on Si/SiO₂ substrate, by opening the resists in the areas between the ribbons. In this manner, the remaining resist act as a mask to protect the ribbons (Figure 2.8a). As can be seen in Figure 2.8b, the outer parts of the design are underdosed

whereas the inner part is overdosed. This is due to the fact that the sum of electrons reaching the resist during the exposure step. For these cases, another strategy that can be followed is not only to adapt the design dimensions and writing parameters, but to create a dose gradient that will give different dose factors to the different parts of the design, compensating in this way the effective dose distribution (Figure 2.8c).

In summary, except for the case of very standard substrates and samples, such as large electrical contacts on Si/SiO₂ substrates, we will always need to prepare some dose tests and proximity effect corrections before we are able to prepare our sample.

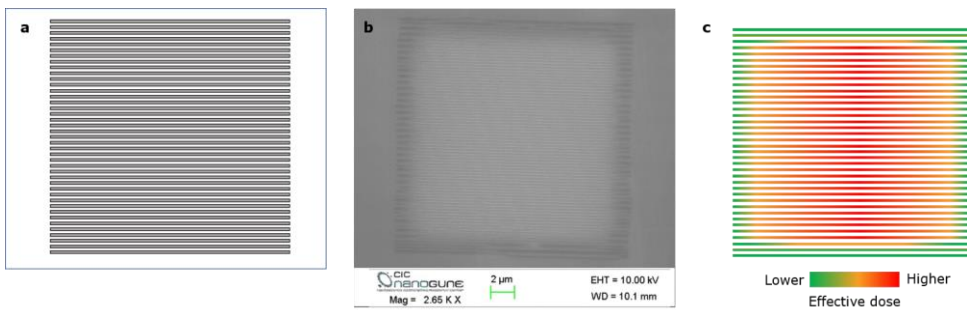


Figure 2.8: EBL exposure of an array of ribbons on Si/SiO₂ (300 nm) substrate. a) Schematics of the design of an array of ribbons. The lines correspond to the exposed areas, thus the areas that will be etched for preparing the array. b) SEM image of an overdosed array, after etching the SiO₂ and before removing the PMMA mask, in which the exposure parameters and the dimensions of the design created an effective dose higher in the central part of the array than in the edges. c) Qualitative schematic of the effective dose distribution experimentally observed in (b), obtained by comparison of the nominal design to the actual result after exposure and etching.

Development after exposure

After the exposure, the results of the patterning are still invisible. We need to *reveal* them by developing the sample. This is done by immersing the sample in a developing solution, commonly known as developer. During this step, we dissolve the exposed parts of the positive resist (or unexposed, in the case of

negative resists). The concentration and temperature of the developer and the developing time affect the result of this step, and each resist may use its own developer and have different sensitivity to the change of these parameters.

For the case of PMMA, the standard developing protocol consists in immersing the sample 60s in the developer, methyl isobutyl ketone (MIBK), diluted 1:3 in IPA, followed by a rinse in IPA. If we used the conductive gold layer, we should remove it before proceeding to develop. For very small structures, cooling down the developer slows down the process and helps improve the definition of the structures. Finally, if the sample that we are fabricating requires a lift-off step, doing a soft O₂ plasma will help burn some possible residues of resist on the opened gaps, and improve the adhesion. All the details regarding the developing step for samples prepared with PMMA are presented in Table 2.5. The time and temperature can also be adjusted to match the requirements of the sample.

Step		Solvent	Temperature	Time	Rinse
Conductive layer removal	<i>Only for Au layer</i>	Au etchant	RT	5-10s	DI water (2 times) IPA
	<i>Standard protocol</i>	MIBK:IPA ⁷	RT	60s	IPA
Developing PMMA	<i>Nanostructures</i>	MIBK:IPA	-10°C	30-60s	IPA
		Process	Power	Time	
Burning PMMA	<i>If lift-off of nanostructures is required</i>	O ₂ plasma	20W		20s

Table 2.5: Parameters for the developing of samples prepared at the EBL using PMMA and 2.3 nm of Au as conductive layer.

⁷ The standard developer solution for PMMA is MIBK, diluted 1:3 in IPA.

2.2. Metallization and lift-off

During the metallization step, we deposit a metal on the sample following the design previously patterned on the resist. After the lift off, we will have transferred the lithography design to the substrate. During this thesis, two techniques were used for deposition of metals: evaporation and sputtering.

Sputtering is based on the bombardment of a target with plasma, typically Argon. The ions hit a target, which contains the material that we want to deposit, ejecting (or *sputtering*) its atoms, which then condense when in contact with a surface [72]. This result is the formation of a film on the walls of the chamber, and the surface of the sample.

Evaporation is based on the principle of vapor deposition. It takes place inside of a chamber in which the pressure has been reduced to achieve high or ultrahigh vacuum. A pocket containing the material is heated up, by an electron beam (electron beam evaporation) or an electrical current passing through the container (thermal evaporation). The material evaporates, and, as the vapor reaches the sample, placed on top of the pocket, it deposits on it, forming a film on the surface. In both cases, we can choose to rotate the sample holder during the deposition of the metal. Rotating the sample will help to achieve more homogeneity in the film thickness, since it will compensate for any possible rate differences due to directional emissions. Nevertheless, when working with double layer of resist or highly pronounced undercut profiles for the fabrication of nanostructures, the rotation might induce the formation of a shadow, enhanced if there are any discrepancies between the angle of incidence of the material (when evaporating more than one metal consecutively).

If we need to perform a lift off step on the sample, we begin the deposition by evaporating the first layer of a few nanometers of Ti or Cr that will act as an adhesion layer for the subsequent metal film. The rate at which these metals are evaporated is also important for the lift-off step. High anisotropy of the metal film, coming from high deposition rates, tends to give better lift off results. Furthermore, we always need to keep in mind that the maximum thickness that

we can deposit for a successful lift off is approximately half of the thickness of the resist.

Finally, during the lift-off step, we dissolve the resist to remove the metal that does not belong to our design. Even though the process is equivalent for every sample, its duration and efficiency strongly depend on the parameters of each one, such as dimension of the patterns and the chip itself, resist, or metal thickness. Normally, lift-off is done by immersing the sample in the resist remover and waiting until the undesired metal lifts from the surface of the sample. For most resists, the remover is acetone, and a rinse in IPA is enough to clean the possible residues.

Additional information 2.4.: Evaporation of metals on CaF_2

- Sometimes, the presence of air inside of very porous substrates can also prevent the proper adhesion of the metallic films, as happens, for example, on CaF_2 substrates. Leaving the substrate overnight in vacuum, inside of the chamber, helps degassing the substrate and improves the success rate after lift-off.

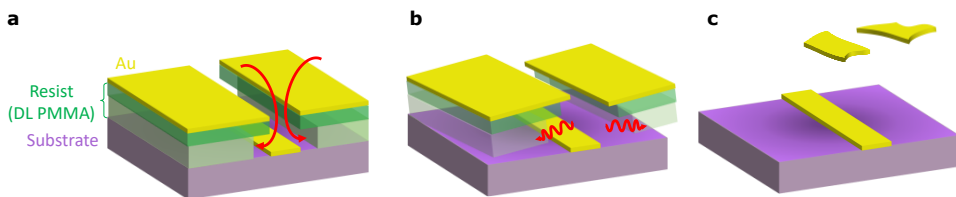


Figure 2.9: Lift-off process on a substrate with double layer of PMMA, red arrows representing the acetone flow, while the sample is immersed in acetone.

a) Thanks to the T profile created by the double layer of PMMA, the acetone is able to flow between the metallic structures on the surface and the resist walls, dissolving it more easily. b) As the resist dissolves, the metal deposited on top of it begins to lift, detaching from the substrate. c) With the resist fully dissolved in the acetone, the metallic leftovers float in the acetone. It is important to take the sample out of the acetone in this step, because if the acetone were to completely evaporate and the metal pieces fell on the substrate, they would attach to it, making it impossible to be removed, and ruining the sample.

Additional information 2.5.: Guidelines for a successful lift-off

- Change the acetone one or two times during the process. For big chips or wafers, this prevents the saturation of the acetone with resist, and favors the flow of acetone between the structures.
- Acetone cools down while reacting with the resist, decreasing the solubility of the resist in the acetone. Warm acetone (40-60°C) can accelerate the lift-off process, but one should be careful that the acetone does not evaporate completely. Once the sample is dry, the process stops, and it is almost impossible to change the results.
- Soft ultrasonication while in acetone is an option, but you risk lifting everything, and not only the metal on the remaining resist. It is however useful for wafers, or substrates to which the deposited metal present good adhesion.

2.3. Etching

Another possibility during the fabrication process is to remove, or *etch*, material, using a mask to protect the areas that we want to preserve. Said mask can directly be the resist used during the lithography step, or a hard mask fabricated by depositing a material that will finally be removed. An schematic of the etching process using resist as mask is shown in Figure 2.10. After lithography, the area to be etched is exposed, whereas the areas to be preserved are covered by the, in this cases resist, mask (Figure 2.10a). After etching, the target material is removed from the exposed areas, while the mask keeps the rest of the surface protected from the etching effect (Figure 2.10b). We then need to remove the resist, to leave the sample as shown in Figure 2.10c.

There are mainly two different ways of etching a sample: wet or dry etching [51]. Wet etching consists in immersing the sample in a solution that has one or several components that react with the material we want to etch, at a certain etching rate. While the sample is in the solution, the material will dissolve in it, forming new compounds that will stay in the solution. This type

of etching is typically selective, but the etching is not directional, and it might affect the conformity of the structure.

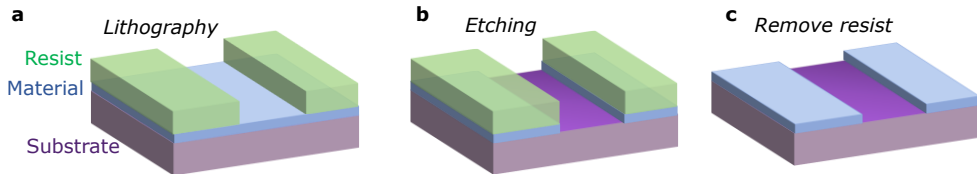


Figure 2.10: Etching step using resist as mask. a) Mask of resist prepared using lithography. The areas to be etched are exposed, while those areas that we want to keep are protected by the resist layer. b) Sample after etching, where the resist keeps the protected areas from being etched. c) After the etching step, we need to remove the resist to reveal the result.

On the other hand, dry etching is based on the removal of material by a bombardment of ions. Depending on the way of producing said bombardment, we can define different techniques. Reactive Ion Etching (RIE) is a technique that etches the material using a neutral gas, such as oxygen or fluorine-based gases, that is ionized to create a plasma. This can be achieved using methods like RF discharge, microwave discharge, or DC discharge. These methods create an electric field that leads to collisions between gas molecules, producing ions and free electrons, that react with the material to be etch, producing volatile products [73]. The presence of charges induces a directionality in the etching, making it more homogeneous than in the case of the wet etching. Furthermore, the presence of a gas flow results in a higher selectivity and tunable etching rates, as function of the pressure and flow rates. The biggest inconvenience from RIE is that the plasma might react with the resist if it is used as a mask, generating crosslinking, thus making it impossible to be removed. Additionally, the interaction between the resist and the material below may damage the surface. The use of Cr-Al hard mask can help to solve this issue, if the sample is not sensitive to the wet etch of the Al mask. Another option is to use the ion milling technique. Argon plasma is used to bombard the surface of the sample, etching the material in the process. It is also very directional, but not as selective, although etching rates can be controlled with the voltage bias that is

applied in the chamber. Both with ion milling and RIE, doing the process in short cycles, letting the resist cool down in between steps, may help avoid overheating the resist and damaging the surface below.

2.3.1. Hard mask for etching

For some materials and processes, we need to further protect the areas that we want to preserve from etching. In those cases, we will prepare a metallic hard mask that will replace the resist, thus avoiding affecting the surface of the material due to cross linking or over heating of the resist. After doing the lithography to define the areas that will be covered by the hard mask, we form the mask by evaporating 5 nm of Chromium via e-beam evaporation, as an adhesion layer, followed by 40 nm of thermally evaporated Aluminum (Figure 2.11a).

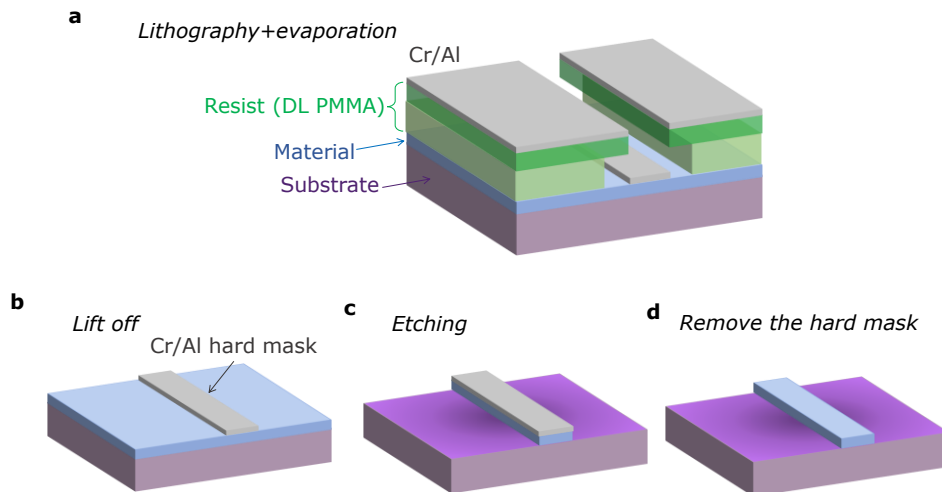


Figure 2.11: Etching step on a sample using a Cr/Al hard mask. a) Evaporation of the Cr/Al layer after the lithography to define the mask. b) Sample with the prepared hard mask after lift-off, ready to be etched. c) Sample after the etching, where the hard mask has protected the material from the etching; d) Result after removal of the hard mask.

Once the evaporation step is finished, we need to do the lift-off, as described in section 2.2.. Finally, we rinse in IPA to remove acetone residues, and we can proceed to etch the sample. After the etching step, to remove the hard mask we need to immerse the sample in Cr etchant, an acid that will etch the Cr adhesion layer and, at a lower rate, the Al. Leaving the sample in the acid for 10-15 minutes is enough to remove the mask. Then, we need to rinse the sample in DI water to remove the residues from the acid, and finally dry it by blowing N₂.

Additional information 2.6.: Technical details for the evaporation of the Cr/Al layer

- In the evaporation of Cr, the whole material needs to be homogeneously heated up, by irradiating it completely with the e-beam. The Cr target contains small scales of material, that individually melt and result in oscillating rates during the evaporation.
- To get a good approximation of the evaporation rate, it is important to set a shutter delay to allow the whole target to melt and start the deposition when the rate approximately stabilizes. However, the rate will never be completely stable, which is it is required to also to set high tolerance for the deposition rate (e.g. 30%).
- The evaporation of Al is done by thermally. The Al target takes a long time to heat up and melt, but, in contrast to chromium, once it starts evaporating, the rate is very stable.
- Due to the thermal capacity of Al and Cr, they take a long time to cool the target down. Additionally, both materials also oxidize quickly while warm. Thus, it is recommendable to wait for an hour after finishing the deposition before opening the chamber, to avoid, on the one hand, oxidation of the target, and on the other hand, breaking any element in the chamber due to thermal shock.

2.4. Conclusions

We have introduced the techniques that have been used for the preparation of all the samples described in this thesis. In particular, we reviewed some lithographic techniques. Direct Laser Writer (DLW), which employs optical lithography to direct a laser beam onto a resist that is sensitive to the laser's wavelength (typically 405 nm). This process allows for the creation of patterns with minimum resolutions of around 500 nm. Another technique explored is Electron Beam Lithography (EBL), which utilizes electron-sensitive resist materials to achieve even smaller feature sizes, with minimum features as small as 20 nm. The successful implementation of EBL relies on adjusting exposure parameters such as acceleration voltage, dose factor, and step size, as well as carefully selecting an appropriate resist and correcting for the proximity effect.

Following the lithography steps, material deposition onto the samples is achieved through techniques such as evaporation or sputtering. These methods involve the controlled deposition of materials onto the desired regions of the samples. During the subsequent lift-off step, excess material that was deposited over the resist layer is removed, resulting in the final structures being obtained. On the other hand, material removal is accomplished through reactive ion etching or ion milling. These processes selectively eliminate material to structure the substrates or flakes into the desired shapes. To protect the surfaces from etching and preserve their properties, Cr-Al hard masks can be utilized.

The recipes and processes described in this chapter correspond to standard protocols, that can be generally adapted to most of the cases. They give a starting point for those samples that, due to their complexity, need further optimization. In the next chapter, we are going to describe recipes and protocols that have been purposely modified and perfected for the fabrication of specific samples.

3. Design and optimization of fabrication processes

The combination of the different protocols and techniques described in the previous chapters allows the fabrication of a wide variety of samples for very different applications. During the development of this thesis, many samples were prepared to address different physical phenomena, all of them to some extent including nanometric features. In this chapter, we present the most significant ones, either due to their process of fabrication or special characteristics of the employed substrate or the samples themselves. Most of them were prepared in the context of collaborations and thus, the details about the motivation for the project, measurements and results obtained from the samples, have been left out and can be found in the referred articles. Instead, here we focus on the detailed description of the optimization of the recipes and protocols, and the characterization of the samples along the fabrication process.

The chapter is divided into five separate sections, each one of them covering a different project or type of sample. An additional section is included at the end of the chapter, as a compilation of recipes for general equipment.

3.1. Fabrication of SiO₂ nanogratings for coherent phonics

3.1.1. Coherent phononic on van der Waals materials

Nanoribbons are rectangular structures, with a width below 100 nm and lengths of several micrometers. Single nanoribbons have been extensively exploited in many studies, which report the change of diverse properties of materials due to this kind of nano-structurization [74–76]. Not only single nanoribbons are of interest: arrays can be used as a platform on which to transfer materials to perform different applications [77,78], or as samples themselves to prepare devices and tune the properties of the materials [79]. In this section, we describe in detail the optimized process for EBL fabrication of arrays of nanoribbons. In particular, we review the fabrication of SiO₂ nanogratings for coherent phonics using van der Waal materials [80].

Strain is known to affect the properties of some 2D material, thus control over the applied strain can lead to tunable modifications [81,82]. By harnessing coherent phonons, which carry dynamic strain, we can push the boundaries of strain engineering to control both classical and quantum phenomena in the unexplored temporal domain of picoseconds and spatial domain of nanometers. [83]. In this work, the aim was to study the interaction between coherent phonons and the flexural modes in thick layers of 2D materials placed on nanogratings of different materials [80]. For this purpose, we were given the task of fabricating nanogratings of SiO₂. We fabricated them by patterning standard substrates of 300 nm of SiO₂ thermally grown on Si, using EBL, and then RIE to etch and obtain the structures. The SiO₂ film was etched in some areas to form the gaps of the nanogratings (*grooves*), while the ribbons (*teeth*) were protected by a Cr/Al hard mask. We aimed for tooth widths ranging from 75 to 150 nm, with grooves from 50 to 100 nm. The nanogratings were designed to have a lateral size of 20 μm , so they could be big enough to transfer flakes of 2D materials required for the final measurements. A summary of the fabrication steps and final sample is shown in Figure 3.1, and the aimed vs. final tooth-

groove ratios are collected, together with some fabrication details, in Table 3.1, at the end of this section. After transfer of 2D materials flakes on the nanogratings, the breathing modes were observed, as reported in literature [84,85]. For the nanograting fabricated on other materials, vdW flakes were transferred, revealing modes in the GHz frequency range for the coherent phonons: (i) a thickness independent zeroth-order symmetric S0 Lamb mode with frequency up to ~ 40 GHz over the grating with a period of 150 nm; (ii) two hybrid flexural phonon modes, which combine flexural modes above the grooves and modes with the mass-on-spring oscillations above the ridges of the nanograting [80]. These findings open the way for control strain induced processes in 2D-vdW materials at the picosecond time scale.

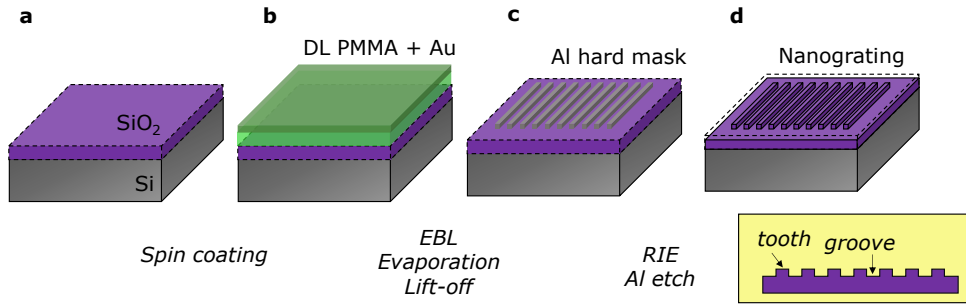


Figure 3.1: Schematics of the fabrication of SiO_2 nanogratings. a) Commercial Si/ SiO_2 substrate, where the SiO_2 layer is 300 nm thick (marked by the dashed line). b) Sample after spin coating with DL PMMA and being covered with 2 nm of Au as a conductive layer, ready for definition of the nanograting at the EBL. c) After the EBL patterning and development, a Cr/Al hard mask is evaporated to protect the surface. After lift-off, the hard mask protects the teeth of the nanograting and leaves the rest of the SiO_2 exposed, so it can be etched at the RIE. d) Schematics of the final nanograting, after etching the SiO_2 surface through the Cr/Al hard mask and removing of the mask to reveal the nanograting. The dash line marks the original thickness of the SiO_2 layer. A cross section of the nanograting is depicted below (d), framed, and marked in yellow.

3.1.2. Fabrication protocol of SiO₂ nanogratings

We begin the fabrication by spin coating DL PMMA on the Si/SiO₂ substrate (Figure 3.1.a,b), following the recipe presented in Chapter 2, and sputtering 2.3 nm of Au to act as conductive layer, for better resolution of the structures. We used an acceleration voltage of 20kV, a 10 μm aperture and different step sizes and doses, ranging from 100 to 180 $\mu\text{C}/\text{cm}^2$. After exposure, we do the developing step following the standard process: we first remove the conductive layer with 10 s of Au etchant, rinse in DI water twice and rinse in IPA, to then develop the sample 60 s in MIBK and rinse for 60 s in clean IPA. The hard mask is prepared following the recipe in chapter 2, by e-beam evaporation of 5 nm of Cr as an adhesion layer and thermal evaporation of 40 nm of Al. Lift-off is done overnight, to make sure that the acetone completely soaks every feature of the nanogratings. We finish the lift-off step by washing the sample in clean acetone, warmed to 60°C, checking every 5-10 mins for an hour. The density of the pattern and the small width of the grooves make this design difficult to lift off. If the lift-off does not progress successfully, we can sonicate the sample for a few seconds to finalize it at the lowest settings, to help detach the aluminum from the areas that need to be exposed. Some examples of samples on which the lift-off was not successful are shown in Figure 3.2.

After lift-off, the sample is ready for the RIE step (Figure 3.1.c). We follow the recipe 4 shown in Table 3.5 to etch the SiO₂ at the RIE. Finally, we remove the hard mask by immersing the sample in Cr etchant for 10 mins, followed by two minutes in DI water and a second rinse in DI water. We dry the sample blowing with N₂ gun, leaving it finally ready for characterization. We characterize the final dimensions of the samples via SEM, to make sure that the nanogratings meet the requirements. SEM images of one of the fabricated nanogratings are shown in Figure 3.3. The discrepancies between nominal and actual dimensions of the nanoribbons are summarized in Table 3.1, with the corresponding fabrication details. As can be observed, the tooth/groove distance is kept in the design, but the actual dimensions of the written lines are approximately twice the size of the nominal design. Remarkably, no dose or size

gradient was required to correct the proximity effect and obtain a good definition of the nanograting.

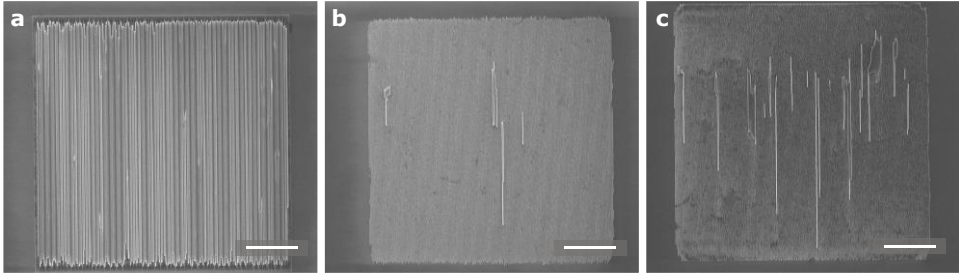


Figure 3.2: SEM images of Cr/Al hard mask not well defined due to problems during the lift-off. Scale bars correspond to 10 μm . a) Sample removed from lift-off too early. b) Nanograting in which some parts of the grooves stayed after lift-off. c) Sample similar to (b), in which the lift-off process failed to completely clean some grooves.

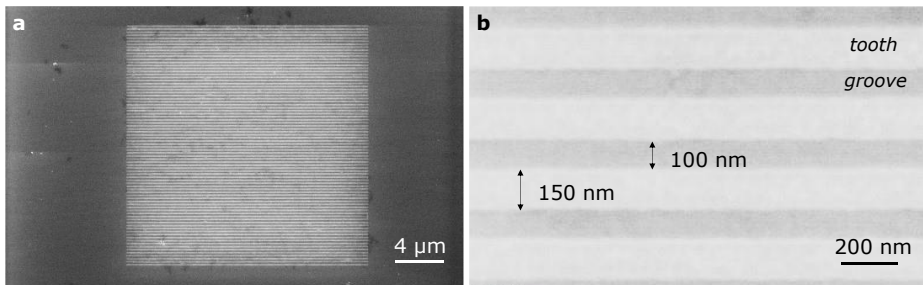


Figure 3.3: SiO₂ nanograting. a) SEM view of a SiO₂ nanograting. b) Zoom into the nanograting shown in (a).

Target dimensions (tooth/groove)	Design dimensions (tooth/groove)	Actual dimensions (tooth/groove)	Step size	Area dose
75/50 nm	30/95 nm	80/45 nm	9.6 nm	170 $\mu\text{C}/\text{cm}^2$
100/60 nm	50/100 nm	100/60 nm	9.6 nm	180 $\mu\text{C}/\text{cm}^2$
120/80 nm	50/150 nm	120/80 nm	14.4 nm	170 $\mu\text{C}/\text{cm}^2$
150/100 nm	70/180 nm	150/100 nm	14.4 nm	170 $\mu\text{C}/\text{cm}^2$

Table 3.1: Summary of the size and dose corrections for the fabrication of SiO₂ nano gratings.

3.2. ML-hBN nanoribbon arrays for observation of phonon polariton resonances

3.2.1. Motivation for the search and manipulation of CV ML-hBN phonon polaritons

Phonon polaritons are electromagnetic waves formed by strong coupling of light to optical phonons of polar materials. In layered materials, such as hBN, phonon polaritons can propagate with short wavelengths and field confinement, long lifetimes and anomalous wavefront [86–88], which promise a many future applications such as ultra-sensitive surface-enhanced infrared molecular vibrational absorption spectroscopy based on polariton resonators [89–91], deep subwavelength-scale infrared waveguiding [92] and ultrafast nanoscale heat transfer [93,94]. However, most phonon polariton studies are performed with micromechanically exfoliated hBN flakes, that cannot be escalated to industrial fabrication processes. Thus, the synthesis of these materials via wafer-scale methods, such as Chemical Vapor Deposition (CVD) growth [95], is key to obtain exploit its properties in applications such as surface enhance infrared molecular vibrational sensing [89,96,97] or plasmon-assisted infrared photodetection [98].

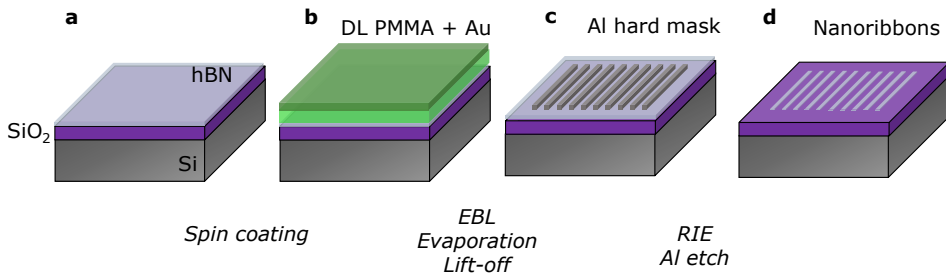


Figure 3.4: Schematics of the fabrication of arrays of ML-hBN nanoribbons. A) CVD-grown ML-hBN after transfer to a Si/SiO₂ substrate. B) Sample prepared for the EBL step by spin coating of DL PMMA and sputtering of 2 nm of Au as a conductive layer on top of the PMMA. C) Cr/Al hard mask the hBN ML, after evaporation and lift-off, before the etching step. D) Final nanograting, after etching the hBN surface through the Cr/Al hard mask.

To evaluate whether multilayer (ML) hBN (ML-hBN) obtained by CVD growth can support phonon polaritons, we fabricated nanoribbons acting as Fabry-Perot resonators for the polaritons, similar to those used for surface-enhanced infrared absorption spectroscopy (SEIRA) organic molecules and gases [90,91,96]. We started the process on ML-hBN that was already transferred onto Si/SiO₂ substrates. We fabricated the nanoribbons following the same protocol as the one described in section 3.1 after adapting the EBL parameters. A summary of the fabrication process is shown in Figure 3.4.

3.2.2. Fabrication process of ML-hBN nanoribbons

We begin by spin coating the substrate with DL PMMA and sputtering 2.3 nm of Au as conductive layer (Figure 3.4.b). After some tests on Si/SiO₂ substrates, we determined the EBL parameters to be 20 kV of acceleration voltage, step size 3.2 nm and dose ranging from 150 to 180 $\mu\text{C}/\text{cm}^2$. We expose the samples using these values and proceed to the developing step. First, we remove the Au layer with 10 s Au etchant that we rinse in DI water twice, followed by a rinse in IPA. Then, we develop for 60 s in MIBK:IPA (1:3) and 60 s rinse in IPA. We dry the sample with the N₂ gun and load the sample in the evaporation chamber. After evaporation of the Cr-Al hard mask and lift off, as shown in Figure 3.4c, we obtain the hard mask to protect the ML-hBN surface. SEM images of this step of fabrication for two arrays are shown in Figure 3.5a,b. Once the hard mask is ready, we proceed to etch the ML-hBN. In this case, we use the standard hBN etching recipe based in Ar and SF₆, that etches the hBN at a rate of about 30 nm/s (recipe 2 in Table 3.5). In this way, we clean the spaces between the nanoribbons just by etching a few seconds. Finally, we remove the hard mask by immersing the sample in Cr etchant for 10 mins, and rinse in DI water, as described in the previous section (Figure 3.4d).

3.2.3. Summary of results

An example of the final arrays and nanoribbons are shown in Figure 3.5c and d, respectively. These arrays were characterized by near- and far-field infrared spectroscopy by E. Calandrini (CIC nanoGUNE), which revealed sharp phonon polariton resonances that shift to higher frequencies for smaller ribbon widths. The quality factor of the phonon polariton reaches up to $Q \approx 50$, demonstrating the potential of CVD-grown ML-hBN for large-scale fabrication of phonon polariton based infrared devices. More details about these results can be found in [99].

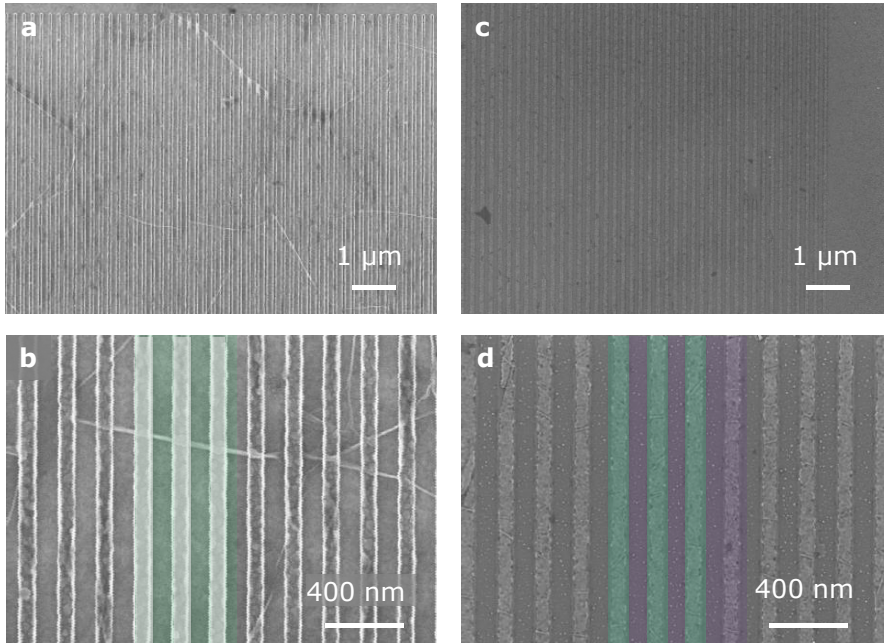


Figure 3.5: Fabrication of nanoribbon arrays using CVD-grown ML-hBN. a) Array on nanoribbons after lithography and Cr-Al hard mask deposition and lift-off. b) Cr-Al hard mask (white) on the ML-hBN (green) previous to RIE, to define the hBN nanoribbons. ML-hBN defects and wrinkles can be seen below the Al structures. c) Array of ML-hBN nanoribbons after RIE and removal of the Cr-Al hard mask. d) Zoom into the hBN nanoribbons shown in (c). Some hBN nanoribbons are marked in green for clarity, whereas the Si/SiO₂ substrate below is highlighted in purple. Final nanoribbon width and period are 75 nm and 200 nm, respectively.

3.3. Nanoresonators on thin membranes for magneto-optical studies

3.3.1. Magneto-optics and plasmonic nanorings

Magneto-optics studies the propagation of light in the presence of magnetic fields, and their influence in light polarization and the intensity of the transmitted light through a magnetic material. Enhancing magneto-optical effects is key to include them in nanophotonic applications, such as optical communication, sensing or imaging [100–102]. Previous works establish gold plasmonic rings as a suitable platform to enhance the magneto optic response of disks of a magnetic material, due to the interaction of the magnetic disk and the dark modes of the ring [103,104]. Furthermore, the less explored non-concentric gold disk-rings nanocavities could provide a tuning knob to induce the enhancement of the magneto-optic response of magnetic materials, by varying the dimensions and distances of the design.

In this context, we prepared arrays of disk-rings nanoresonators to test their plasmonic response as a function of the disk-ring distances and dimensions, while we tested the fabrication limits on the unconventional substrate that are thin membranes, for their characterization using electron energy loss spectroscopy (EELS). EELS has been typically used for the characterization of plasmonic resonators [105–107]. In our case, the energy at which the plasmonic modes are excited will depend on the dimensions of the disk-ring structure. In every case, the sample comprised a ring, with width w up to 100 nm and diameter D from 300 to 500 nm. A disk of diameter d was placed at a certain distance g from the edge of each ring, from the inside or the outside, as shown in Figure 3.6.a and b, respectively. The fabrication was performed on commercial chips that contain a 3x3 matrix of Si_3N_4 membranes of 15 nm of thickness and lateral size of 100x100 μm (Figure 3.7a,b). We used a DL PMMA, to help achieve an easier lift-off. However, due to the variations in the designs, the EBL parameters needed to be optimized for each of the different sizes and configurations required.

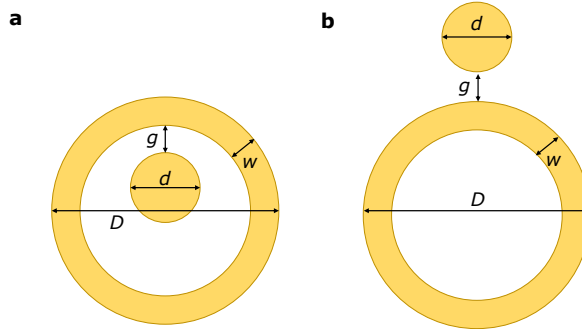


Figure 3.6: Schematic of the non-concentric disk-ring nanocavities, with all the variable parameters. For both panels, D corresponds to the external diameter of the ring, w to the width of the ring, d is the diameter of the disk, and g the gap between the disk and the external edge of the ring. a) Disk-ring nanocavity, in which the disk is placed inside of the ring, at a distance g . b) Disk-ring nanocavity, with the disk placed outside of the ring, at a distance g .

3.3.2. Substrate preparation and spin coating

We first need to prepare the chips by doing an O_2 plasma treatment, to enhance the adhesion of the PMMA resist. We set a power of 100 W for 10 minutes, with 1 mbar of pressure and an O_2 flow of around 10 sccm. As stated before, for this fabrication we need to spin coat the chips DL PMMA. For both bottom and top resist layers the same conditions are used. Each layer is spin-coated and posteriorly baked. To avoid destroying the membranes due to the application of vacuum to hold the chip during spin coating, we used a portable spin-coater, which holds the sample in place thanks to a ledge that takes advantage of the centrifuge force (Figure 3.7c). For both layers, the resist is spined at 3500 rpm for 5 minutes. The chips are then baked at 170°C for one hour in a convection oven. There, the inside of the chamber is kept in a N_2 atmosphere. Additionally, the baking step is programmed to have heating and cooling ramps. The baking temperature is achieved after 20 mins of ramping up from room temperature up to 170°C . After an hour baking, we ramp down to room temperature for another 20 mins. This treatment avoids breaking the membranes due to thermal shocks. After baking the second layer of resist, the chips are ready for patterning.

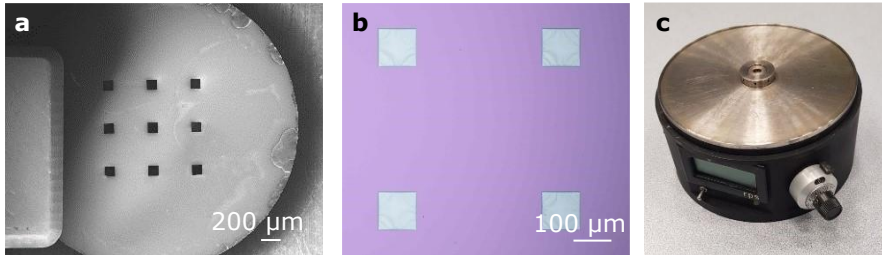


Figure 3.7: TEM membranes used for lithography. a) Si₃N₄ membranes commercial chip. b) Optical image of four membranes. c) Portable spin coater that uses centrifuge force instead of vacuum to fix the sample. The sample stays against the bevel in the center of the spin coater.

3.3.3. Importance of the design and writing modes during the EBL exposure of the structures

The minute thickness of the membranes makes them practically invisible to the electrons, thus making the proximity effect negligible and allowing an excellent resolution. However, the low dimensions of the nano resonators make the rest of the electron beam parameters also play an important role in the outcome of the lithography. First, we need to perform a dose test to determine the dose required for the substrate. Since we do not expect to have any proximity effect, 10 kV of acceleration voltage is enough to define the structures. The absence of backscattered electrons results in the need of higher area dose, as shown in Figure 3.8. The usual area dose required for DL PMMA and 10 kV acceleration voltage is $\sim 100 \mu\text{C}/\text{cm}^2$. However, as can be seen Figure 3.8a., for the nanoresonator on the membranes, the best results are obtained doubling this area dose, and setting it to 200-250 $\mu\text{C}/\text{cm}^2$, using the 10 μm aperture (i.e., current of about 20 pA). A size test to determine the minimum ring width and ring-disk gap is presented in Figure 3.8b. The minimum width that we can obtain with these parameters and equipment is about 20 nm, and the ring-disk gap when the disk is outside of the ring is also 20 nm. Developing is done as usual, by immersing the sample 60s in MIBK:IPA (1:3), and stopping the developing reaction by rinsing in IPA. Finally, the substrate is dried by gently blowing N₂ on the surface.

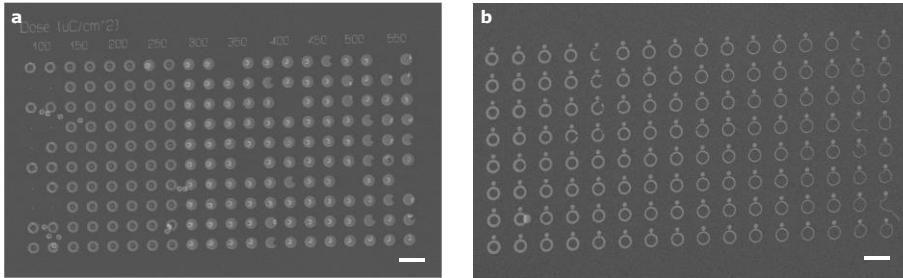


Figure 3.8: Dose and size test for eccentric disk/rings nano resonators using 10 kV acceleration voltage. Scale bars on both images correspond to $1\mu\text{m}$. a) Dose test for the structures with the disk inside of the ring. Best results are obtained for doses 200-250 $\mu\text{C}/\text{cm}^2$. b) Size test for different widths of the ring, with the disk is outside of the ring and a nominal ring-disk gap of 20 nm.

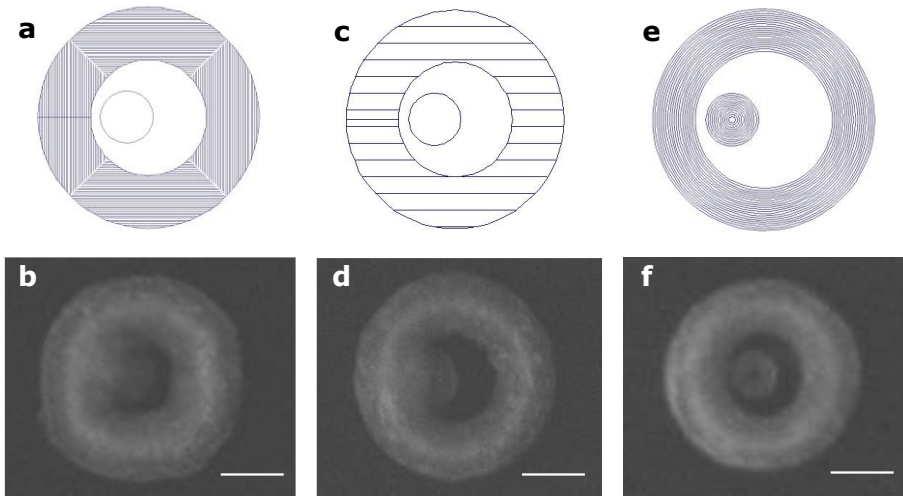


Figure 3.9: Pattern debug for different writing modes at the EBL, in which the lines indicate the beam path, and the corresponding results after Ti/Au evaporation. The scale bar corresponds to 100 nm. a) Pattern debug for the ring-disk designed by subtracting the inner area to a bigger circle and writing in concentric mode. b) Results for the lithography done as described in (a), in which the ring shows square-like features due to the writing mode. c) Pattern debug for the same design as in (a); but using longitudinal mode. d) Results for the lithography shown in (c), in which the ring has a rounder shape, but the inner disk still fuses with the disk. e) Pattern debug for the ring written like a single circle with a given line width, writing with longitudinal mode. In this case, longitudinal and concentric modes are equivalent, since the beam writes along the lines in the design. f) Result for the lithography described in (e), in which the structure is well defined.

The described parameters are suitable for obtaining the required dimensions for the nanoresonators. However, since the samples are close to the resolution limits, the way in which we design and write also affects the final shape of the structures. The results after patterning with different ways of writing are shown in Figure 3.9, the most adequate being the longitudinal writing mode for patterning the resonator ring as circle line with a given width (Figure 3.9e,f).

With all the parameters and variables properly characterized, we have the rings with the desired dimensions on the membranes, and we can proceed to the metal evaporation for forming the metallic structures, and the consequent lift-off and final characterization of the samples.

3.3.4. Metal deposition and lift-off of nano structures on TEM membranes

To place the samples in the evaporating chamber, the best way to proceed is to attach the chips to the sample holder by adding tape on top of them, without touching the membranes. In this manner, it will be possible to detach the chip from the holder after the deposition, without damaging the membrane due to the force used in the process. Furthermore, avoiding the deposition of metal on one side of the chip also helps during the lift-off, as it gives the acetone access to the resist. With the sample fixed and loaded in the evaporator chamber, we can proceed to the metal deposition.

The evaporation of a Ti layer as adhesion layer leads to the formation to a shadow around the structure, due to the mismatch in the evaporation of the two layers. This effect, noticeable due to the dimensions of the rings, can be observed in Figure 3.9b, d and f, and is shown in more detail in Figure 3.10. To avoid the Ti layer and still get successful results during the lift off, we do the evaporation of the Au layer without rotation. This prevents the gold from touching the walls of the resist, and results in smoother lift-off.

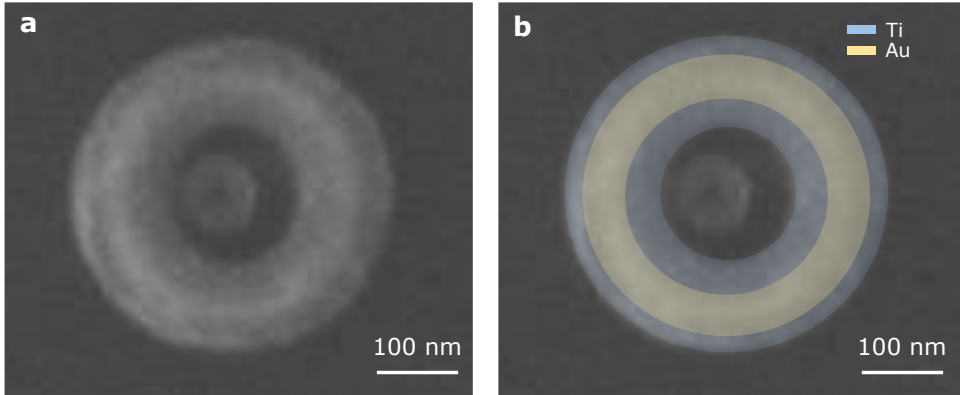


Figure 3.10: Ti/Au mismatch. a) SEM image of a nanoresonator in which the Ti-Au deposition was done using rotation. A difference in thickness between the central and outer parts of the ring can be seen. b) Interpretation of the Ti shadow due to the rotation of the sample during metal deposition, due to the different angle of evaporation and distance from the material target.

Finally, we do the lift-off by leaving the samples in acetone for a few hours, after which we change the sample to clean acetone and gently move around the membranes to help detach the remaining resist. Checking at the optical microscope while still immersed in the acetone might help determine the state of the process. Once we consider the lift-off has finished, we rinse the sample in IPA and dry by gently blowing the sample with the N_2 gun.

3.3.5. Fabrication summary and results of EELS characterization

We have detailed the fabrication of nanoresonators on TEM Si_3N_4 membranes for magneto optic studies. The results with the final dimensions are presented in Figure 3.11. Key parameters and considerations for fabrication on these substrates are summarized in Table 3.2. EELS measurements revealed the coupling of the disk and ring plasmonic modes, as shown for a representative disk-ring in Figure 3.12, demonstrating the hybridization of the disk and the ring modes.

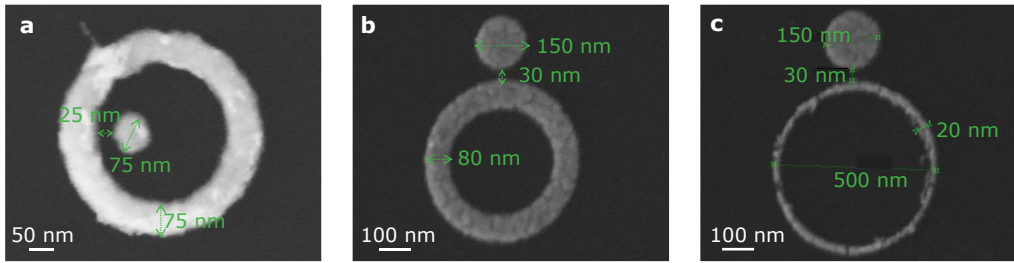


Figure 3.11: Results after optimization of the fabrication process of ring/disks nanocavities. a) Eccentric ring-disk structure with the required dimensions. b) Ring and outside disk. c) Smallest ring fabricated, with same ring-disk gap and disk dimensions as in (b).

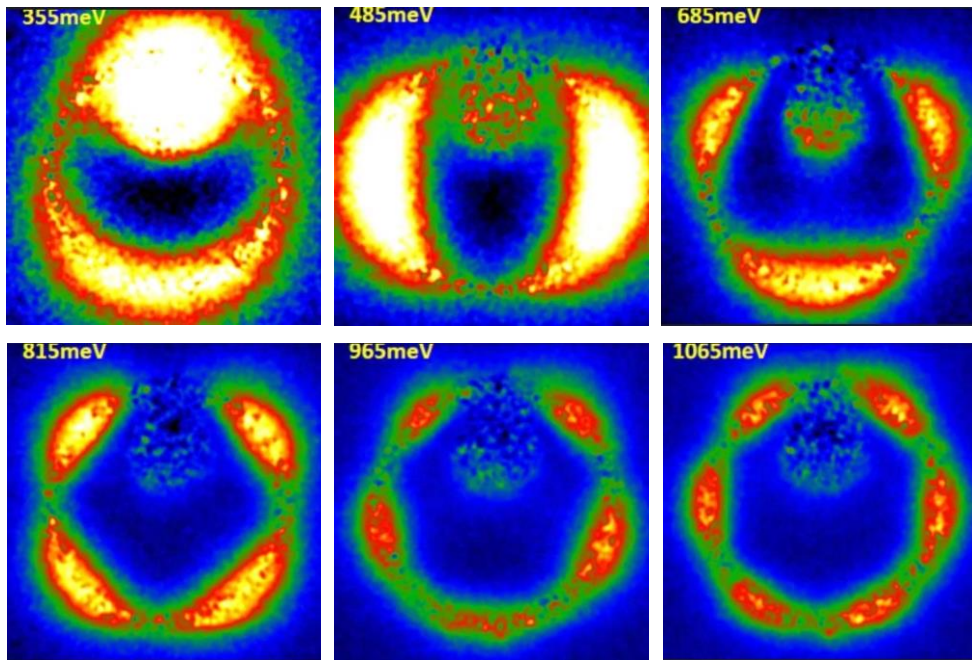


Figure 3.12: EELS characterization of the plasmonic modes of a gold disk-ring system, in which the disk is inside of the rings. The dimensions of the nanocavity are $d = 150$ nm, $D = 500$ nm, $w = 50$ nm, $g = 30$ nm. The energy of the electron beam is indicated in each panel.

Step	Tips
Cleaning the membranes	O ₂ plasma: 100 W for 10 minutes
Spin coating	DL PMMA at the centrifuge force holder spin coater Spin coat at 3500 rpm for 5 mins
Baking	1 hour at 170°C, set temperature ramps.
EBL	10 kV, area dose 200-250 $\mu\text{C}/\text{cm}^2$
Develop	Room temperature MIBK:IPA (1:3) 60 s, rinse in IPA
Evaporation	No rotation, fix chip with one-sided tape
Lift-off	Leave in acetone a few hours, rinse in IPA

Table 3.2: Fabrication of nanostructures via EBL and metal deposition and lift-off on commercial Si₃N₄ membranes

3.4. Nanoresonators on transparent substrates for PL enhancement

3.4.1. Motivation and previous works

Hybrid organic-inorganic metal-halide perovskites (HOIPs) have recently attracted researchers' attention due to their large absorption coefficients, high carrier mobilities and efficient photoluminescence, that makes them suitable for a wide range of optoelectronic applications, particularly photovoltaics [108]. In general, research has focused on lead-based 3D perovskites, more stable and efficient [109,110], but is now shifting towards the search of lead-free materials [111].

In particular, in the study by Adamo et al. [112], a metasurface was patterned to absorb light at the same wavelength as the perovskite photoluminescence, so that, by placing the perovskite on the metasurface, it resulted into a higher effective quantum yield in the perovskite. For fabricating the samples, they prepared an array of slits in a gold film, which was covered with a 3D perovskite,

MAPbI₃. The growth of films of 3D materials can be optimized with annealing and vacuum steps to achieve ordered recrystallization, but leads in general to rough films, full of grain boundaries and small crystals. With this method, there is no precise control over the thickness, to the contrary than using 2D perovskite flakes [22]. In this section, we review the preparation process of metasurfaces for enhancing the PL of lead-free HOIP 2D perovskite (PEA)₂MnCl₄. The quantum yield of this perovskite is lower than for lead-based perovskites, thus making it important to achieve an enhancement for future exploit of these materials.

We prepared metasurfaces based on the design shown in [112] to achieve absorbance around 630 nm, which corresponds to the center of the PL of (PEA)₂MnCl₄ (Figure 3.13). We need to use EBL due to the low dimensions of the resonators, and transparent substrates to be able to measure both in reflection and transmission. The metasurfaces also need to be big enough so that we can transfer the perovskite flakes on top of them. All things considered, we design 45 μm arrays of nanoresonators, both nano slits and nano antennas, with the dimensions ratio as shown in Figure 3.13 After fabrication, we characterized them using a visible spectrophotometer coupled to an optical microscope and Raman spectroscopy for the PL characterization.

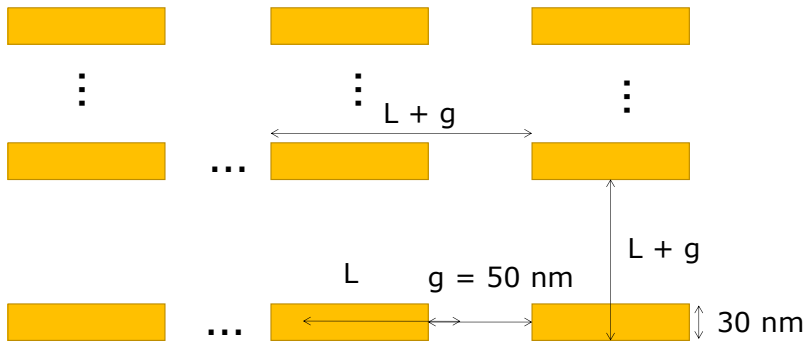


Figure 3.13: Schematics of the design for the fabrication of nano resonators for PL enhancement. Yellow areas indicate the resonators, either slits or nano antennas. L is the length of the resonator, and will range from 50 to 150 nm, to tune the absorbance wavelength of the metasurfaces.

3.4.2. Fabrication of nano slits arrays

Due to the small size of the nano slits, and the technical specifications of our EBL, the best option for their preparation is to use a single layer of PMMA as mask on a previously evaporated Au film. A summary of the fabrication process and final sample is shown in Figure 3.14. To prepare the CaF_2 substrates, we first clean them by sonication in acetone for 2 minutes, followed by 2 mins of sonication in IPA. Then, we need to evaporate the Au thin film on which we will mill the metasurfaces, formed by arrays of nano-slits. We deposit the film by thermal evaporation of 35 nm of Au (Figure 3.14a). After the evaporation, we proceed to spin coat the substrate with resist. For this sample, we use one thin layer of PMMA, which will allow us to get smaller dimensions at the lithography. We chose PMMA 950K, since it is less sensitive than PMMA 495K, which allows the smaller resolution. We spin coat 70 μL of PMMA 950K A2 to completely cover the substrate, at 4000 rpm for 60 s (acc. 1000 rpms), which will form a layer of approximately 100 nm thickness, and then bake the substrate for 90 s at 180°C. We finalize the preparation of the substrate by sputtering 2.3 nm of Au on top of the resist, as a conductive layer (Figure 3.14b).

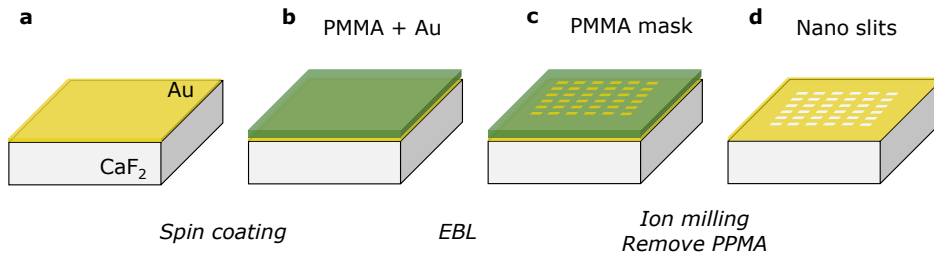


Figure 3.14: Fabrication of nano slits arrays on CaF_2 substrate. a) Evaporated Au film on the surface of the CaF_2 substrate. b) Single PMMA layer spin coated on the Au/ CaF_2 substrate, on top of which we sputter 2 nm of Au as conductive layer. c) Sample after the exposure at the EBL and developing step of the nano slits array. d) Final nano slits array after milling the Au film through the PMMA mask.

With the substrate ready, we use EBL to define the slits, with the following parameters: acceleration voltage of 20 kV, 10 μm aperture, 9.6 nm step size and dose 170-250 $\mu\text{C}/\text{cm}^2$. After exposure, we remove the Au layer by 10 s of gold etchant, cleanse by rinsing in DI water twice and rinse in IPA. We then develop in cold (-10°C) MIBK:IPA (1:3) for 60 s, followed by a 60 s rinse in IPA (Figure 3.14c).

The last step is to remove the gold to form the slits array. For this step, we use the ion miller system with the recipe optimized for milling Au (see Table 3.6 for more details, and Figure 3.14d for a schematic of the sample after this step). The nominal milling rate for Au following this recipe is 14.4 nm/min. We do the process for 180 s to completely clean the slits (Figure 3.15a,c). It is important not to exceed the time, since over milling the structures results in the destruction of the arrays (Figure 3.15b,d). Finally, the resist mask is cleaned by leaving the sample in acetone overnight and rinsing in IPA.

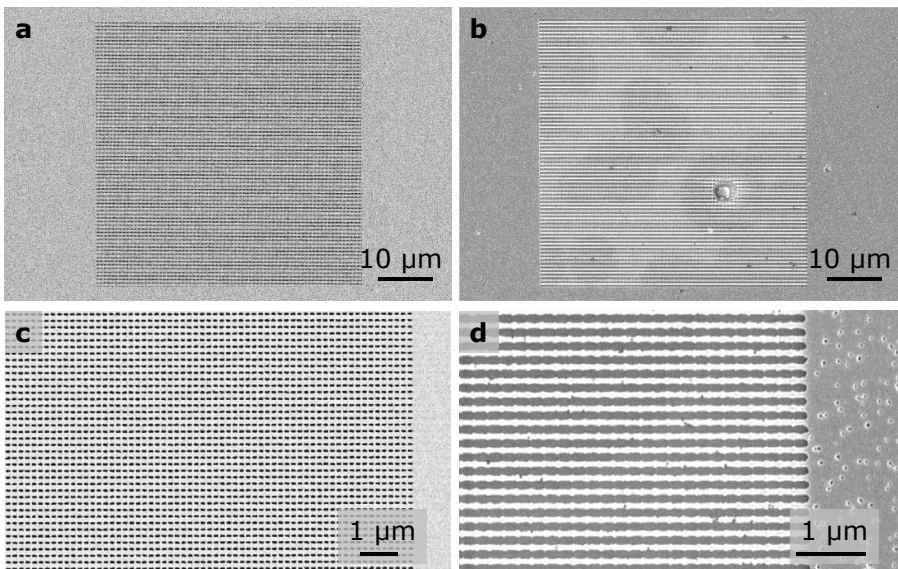


Figure 3.15: Slit arrays metasurfaces. a) SEM image of the array. b) SEM image of an overmilled array. c) Zoom into the array shown in (a). d) Zoom into the overmilled structures shown in (b).

Additional information 3.1.: Use of O₂ plasma to clean resist residues

- Sometimes, O₂ plasma is used to clean residues of resists. This step is compatible, for example, with hBN flakes and gold structures on SiO₂ substrates, but not for insulating substrate, like CaF₂ or Pyrex, since the O₂ plasma affects the substrate below the gold, resulting in the formation of bubbles on the surface of the Au.

3.4.3. Fabrication of nano antennas arrays

The second option is to prepare the same metasurface but with nano antennas instead of slits. In this manner, the electrical field is enhanced in the gaps between the nanoantennas, instead of inside the slit [113,114]. Once again, we need to use EBL to define the resonators. In this case, we will prepare the arrays by evaporation and lift-off of the gold after the patterning step.

For the fabrication using EBL, and based on the results of previous studies, we design arrays of nano antennas of approximately half the size that we want to get. As in the case of the fabrication of the slit arrays, we spin coat the substrates with a single layer of PMMA 950K A2, and sputter 2.3 nm of Au on top. At the EBL, we set 20 kV as acceleration voltage, 3.2 nm step size and 180-200 $\mu\text{C}/\text{cm}^2$ area dose. After exposing the structures, we remove the conductive layer by immersing the sample 10 s in Au etching, and we rinse twice in DI water and once in IPA, as usual. We develop using cold (-10°C) MIBK:IPA (1:3) and rinse again in IPA. To make sure that the resist is completely removed from the exposed areas, we do a soft oxygen plasma treatment for 20 s with 20 W power. After this step, we load the sample in the evaporator and leave them un vacuum overnight, to degas the substrate, which will lead to better adhesion of the Ti/Au layer and a more successful lift-off. Finally, we evaporate 5 nm of Ti as adhesion layer, and 35 nm of Au. Lift-off is done, as usual, in acetone. Figure 3.17 shows two nanoantenna arrays, for comparison between optimized fabrication (a, c) and overdosed structures (b, d). Finally, 10 nm of SiO₂ were

sputtered on the arrays to avoid quenching the PL of the flakes transferred on top.

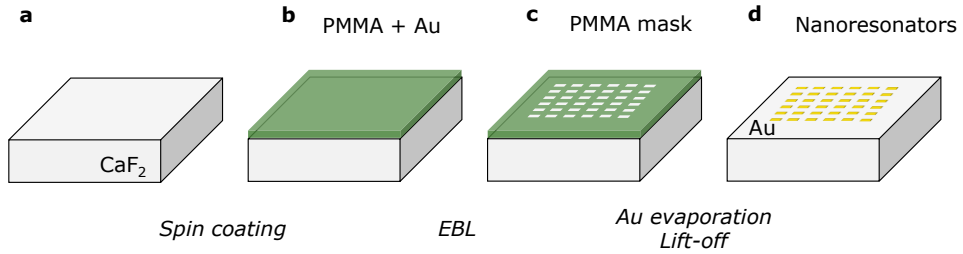


Figure 3.16: Fabrication of nano antennas arrays on CaF_2 substrate. a) Bare CaF_2 substrate, ready for the fabrication process. b) Preparation of the substrate by spin coating a single layer of PMMA and sputtering 2 nm of Au. c) PMMA mask after EBL patterning. d) Array of nano antennas after Au evaporation and lift-off.

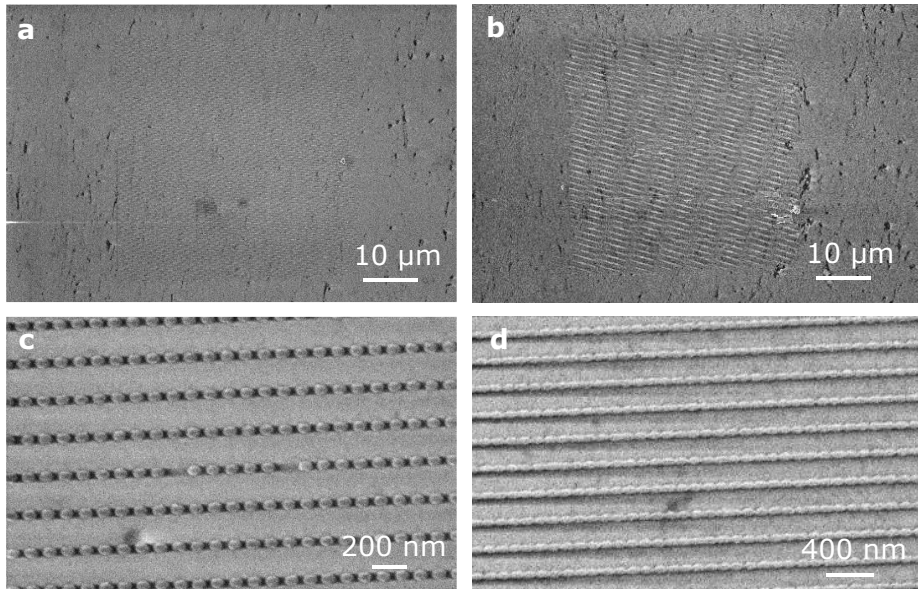


Figure 3.17: Arrays of nanoantennas for PL enhancement. a) SEM image of the array of nanoantennas designed to have the absorbance at 630 nm. b) SEM image of an overdosed array. c) Zoom into the antennas. d) Zoom into the overdosed array, showing the absence of gap between the antennas.

3.4.4. Characterization of the metasurfaces

All the arrays were characterized using a visible spectrophotometer (Figure 3.18a) that is coupled to a microscope using an optical fiber. The different absorbance wavelengths can be observed optically (Figure 3.18b) and determined quantitatively using the spectrophotometer (Figure 3.18c). As expected, for shorter antennas, we get weaker absorbance, and centered around shorter wavelengths.

(PEA)₂MnCl₄ flakes of different thicknesses, ranging from 40 to 200 nm, were transferred from PDMS stamps on top of the arrays with the absorbance centered around 610 nm and the resulting PL characterized at a Renishaw Raman spectrometer. An example of a flake transferred to one of the arrays is shown in Figure 3.19a,b. As can be observed in Figure 3.19c, the resulting PL of the flake on the array is shifted with respect to the original PL of the material. Therefore, there is a contribution mainly arising from the PL of the gold nano resonators themselves. Further studies and simulations need to be done to understand these results, to optimize the design and analysis of the measurement.

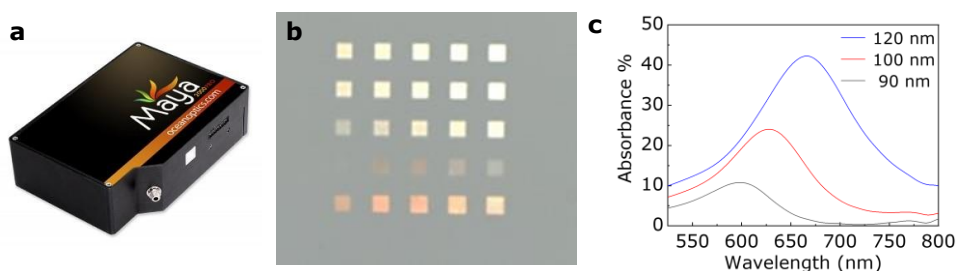


Figure 3.18: Characterization of the absorption wavelength of the nano antennas previous to the transfer of the perovskite flakes. a) Visible spectrophotometer module to couple to the optical microscope. b) Optical picture of a set of nano antennas arrays. It can already be observed how the color of the arrays is different, meaning that the nano antennas have different sizes and thus, show different optical absorption. c) Measurement of the absorbance of three different arrays of nano antennas, verifying that the absorbance frequency shifts to higher wavelengths for bigger antennas.

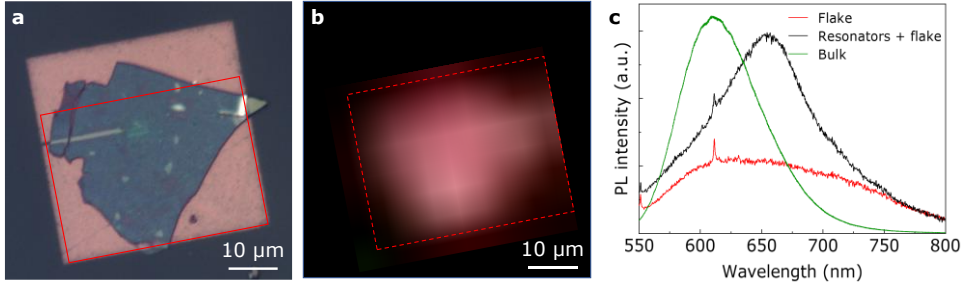


Figure 3.19: Comparison of the PL measurement of a $(\text{PEA})_2\text{MnCl}_4$ flake on and outside the array of nanoresonators tuned to absorb at 600 nm. a) Optical image of the flake used for the measurements in (b). b) PL intensity map of the array of nano resonators shown in (a), centered at 610 nm. c) PL spectra of $(\text{PEA})_2\text{MnCl}_4$ flake outside (red line) and on the array (black line), and of the bulk $(\text{PEA})_2\text{MnCl}_4$ crystal (green line).

3.4.5. Summary of results and outlook

Step	Nano Slits	Nano Antennas
Clean the CaF_2 2 mins in acetone + 2 mins in IPA	✓	✓
Evaporation of Au film	✓	✗
Spin coating + conductive layer PMMA 950K A2 (4000 rpm, 60 s) Bake: 180°C (90s) / sputtering 2,3 nm Au	✓	✓
EBL exposure: 20 kV, 180-200 $\mu\text{C}/\text{cm}^2$ Remove Au layer (5 s in Au etchant) Developing in cold MIBK: IPA (60 s)	✓	✓
Soft O_2 plasma (20 W, 20 s)	✗	✓
Ion milling + removing PMMA mask	✓	✗
Au evaporation + lift-off	✗	✓

Table 3.3: Summary of the fabrication protocol of nano resonators on CaF_2

To sum up, we prepared micro arrays of nano slits and nano antennas, for enhancing the PL of lead-free 2D HOIPs. The optimized parameters for the fabrication of both types of arrays are summarized in Table 3.3. However, despite having obtained the desired dimensions of the nano resonators, and

measured the aimed optical absorbance wavelengths, further analysis of the resulting PL spectra is required to conclude the achievement of the enhancement due to the structuring of the surface below the flakes.

3.5. Fabrication of a single THz resonator on hBN-graphene for ultrastrong light-matter coupling

3.5.1. Previous works and sample design

Recently, strong and ultrastrong light-matter coupling have drawn researchers' attention, not only for fundamental studies, but also to modify properties of matter [115,116], such as chemical reactivity [117] or phase transitions [118]. Studying light-matter interaction down to single subwavelength optical elements may provide insight on the nature of these phenomena and allow control over the opto-electronic properties of individual quantum systems.

Previous works showed that THz light matter interaction in the ultrastrong coupling (USC) regime can be achieved with complementary split ring resonators (cSRRs) coupled to electronic Landau level transitions in a semiconductor quantum well [119,120]. The intrinsically subwavelength nature of the cSRRs facilitates high electric field confinement at a given resonant frequency and thereby benefits the USC interaction. The characterization of the THz single resonator, consisting of an individual resonator, requires the use of asymmetric Si immersion lenses [119]. Having the possibility of measuring the single resonator opens the door for studying light-matter interaction in the THz range of frequencies on exfoliated flakes of 2D materials, typically of high-quality but a few micrometers lateral size. By combining the setup with an applied voltage bias, we would also be able to investigate the USC light matter interaction between the electrons in a high quality exfoliated 2D material flake and the resonant mode of a single THz resonator. The behavior of such a system in the USC regime has been theoretically studied [121,122]. For its experimental

characterization, we first need to fabricate a single THz resonator on top of an hBN/graphene heterostructure, in which the hBN acts as encapsulating layer for protecting the graphene. A schematic of the sample and the measurement configuration is shown in Figure 3.20.

The design of the sample is not as simple as merely placing the graphene flake at the center of the resonator. On the one hand, we need to modulate the Fermi level of graphene, thus the heterostructure needs to be electrically contacted, so that we can apply a gate voltage and electrically characterize the system while it is coupled to the THz pulse. For this purpose, we design a vertical cut on the disk surrounding the resonator, splitting it in two halves, that will act as two electrical contacts to both sides of the graphene channel (Figure 3.20a,b). To contact them, we create two gold wires that connect them to electrical pads outside the area covered by the immersion lenses on the sample. Moreover, as mentioned before, to optically probe the single resonator, the sample needs to be placed in the center of asymmetric immersion Si lenses. To help mounting the samples and lenses centered, we also need to include alignment marks around the resonator disk. A side view of the final sample, as it would look between the lenses, is shown in Figure 3.20c.

To prepare the sample, we begin by exfoliating graphene and hBN directly on Si/SiO₂ substrates, as described in section 1.2. We prepare the heterostructure by picking each of the flakes from the Si/SiO₂ substrate using the PC layer technique (see section 1.4.2 for details). To fill the resonator with graphene, we aim for monolayer flakes over 20 μm lateral size. Therefore, we need to find bigger hBN flakes, with thicknesses of 20 to 40 nm, that can completely cover the graphene flake. We first need to pick-up the hBN flake, then take the graphene, and transfer the full stack to a new substrate. Finally, we clean the PC by immersing the sample for 30 mins in chloroform and rinsing in IPA. The flakes are then ready for lithography. It is important not to anneal the heterostructures after transfer. Even though an annealing step is known to improve the mobility of electrons in the graphene, it can also create pinholes in the SiO₂ layer, increasing the chance of having a leakage current. Even without the annealing step, the Si/SiO₂ substrates have to some extent pinholes that

connect the SiO₂ to the device if they are in contact with the electrodes, thus resulting in the leakage current. To increase the possibility of having a viable device, we reduced the design of the resonator disk from 4 to 2 mm. This size reduces the options of reaching a pinhole as it covers 75% percent less surface than the 4 mm disk, and it gives enough signal to still be measured using the immersion lenses.

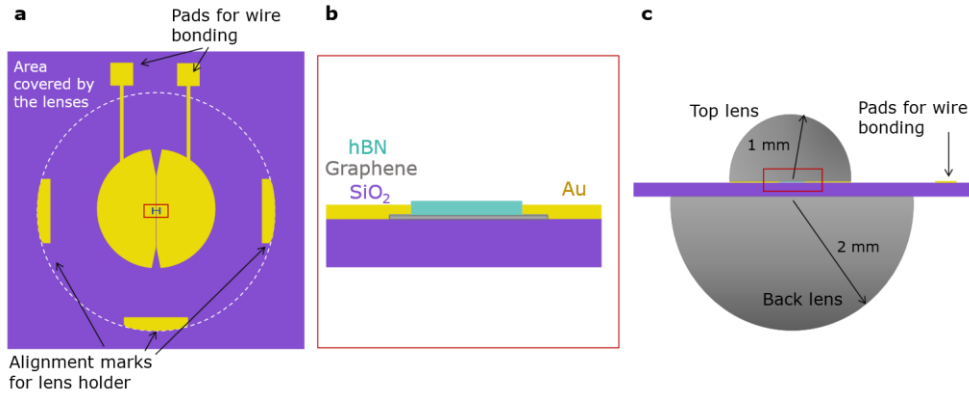


Figure 3.20: Schematics of the resonator and the structure for the coupling to the cyclotron frequency of graphene. a) Top view of the sample, where yellow areas correspond to the parts of the sample covered by gold, and white dashed line marks the area covered by the back lens. The red rectangle indicates the area from which a cross section is shown in (b). b) Cross-section of the center of the resonator, corresponding to the sections framed by a red rectangle in (a) and (c). The hBN flake protects the areas of the graphene flake in the gap of the resonator, and gold electrically contacts the edges of the graphene flake. c) Side view of the Si immersion lenses mounted on the sample. Red rectangle marks the area shown in (b).

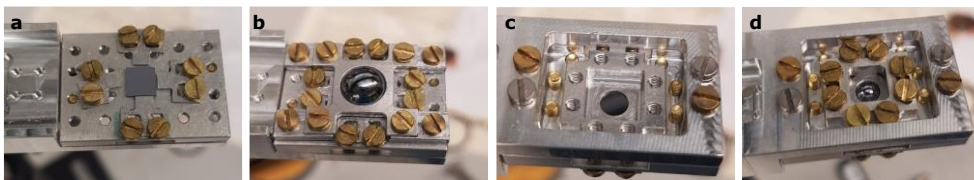


Figure 3.21: Immersion lenses sample holder. a) Si/SiO₂ substrate to be fixed over the lens hole using four clamps and manually centering it. b) Back lens fixed on the back of the sample. c) View of the upper surface of the sample, before being covered by the top lens. d) Top lens fixed on the sample.

3.5.2. Edge contacts for electrical measurements

Once the graphene-hBN heterostructure is ready, we need to electrically contact the graphene. For doing so, we prepare edge contacts, to be able to access the graphene flake, protected by the hBN.

There are two methods for fabricating edge contacts. The first is to etch through the hBN and the graphene, going a bit into the SiO₂ layer to ensure unveiling the graphene flake. This provides one dimensional contacts, since the only point of contact between the metallic electrode and the graphene is the edge of the flake [123,124]. For the fabrication of this type of contacts, we first define the electrodes with EBL (Figure 3.22a). The parameters for this EBL step are summarized in Table 3.4. Secondly, we do an etching step at the RIE to etch the heterostructure, using CHF₃ and O₂ (see the details of the recipe in Table 3.5). Once this step is done (Figure 3.22b), we evaporate 5 nm Ti by e-beam evaporation, as an adhesion layer, and 50 nm of Au via thermal evaporation. Finally, we do the lift-off of the sample by immersing it in acetone, followed by rinsing in IPA. The sample is then ready for electrical characterization (Figure 3.22c).

The type of contacts that we use for preparing the samples in this section is based on the edge contacts technique described above, using a different etching recipe to avoid etching the graphene, thus making the electrodes top contact the flake. Here, again, we used DL PMMA to define the electrodes via EBL. Then, we etched the heterostructure at the RIE, using SF₆, more selective with hBN [125,126] than CHF₃ and O₂, to avoid damaging the graphene and the silicon dioxide film. The parameters for the etching step are detailed in Table 3.5. Hence, we are able to top contact the graphene by successively e-beam evaporating 5 nm of Ti and thermally evaporating 40 nm of Au (followed by lift-off in acetone and rinse in IPA), as shown in Figure 3.23. Finally, Figure 3.24 shows the optical images of the process for a flake contacted following this method.

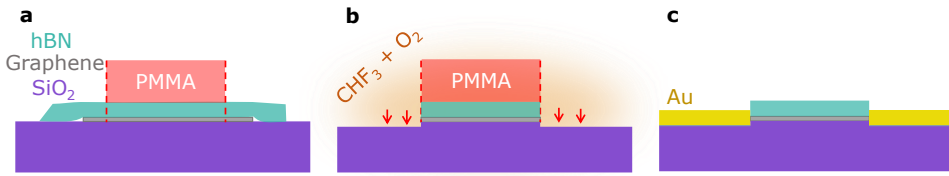


Figure 3.22: Edge contacts using one-dimensional contact procedure. a) Graphene-hBN stack on Si/SiO₂ substrate, after EBL step to define the resist (PMMA) mask. b) RIE step, in which graphene and hBN are etched away due to the action of CHF₃ and O₂ gases. c) Sample after evaporation and lift-off of the metallic electrodes.

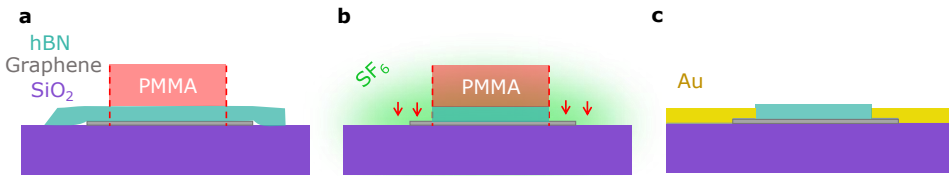


Figure 3.23: Fabrication of top contacts on hBN covered graphene. a) Graphene-hBN stack on Si/SiO₂ substrate, after EBL step to define the resist (PMMA) mask. b) RIE step, in which only the hBN is etched away with SF₆ gas, and graphene stays uncovered. c) Sample after deposition and lift-off of the metallic electrodes.

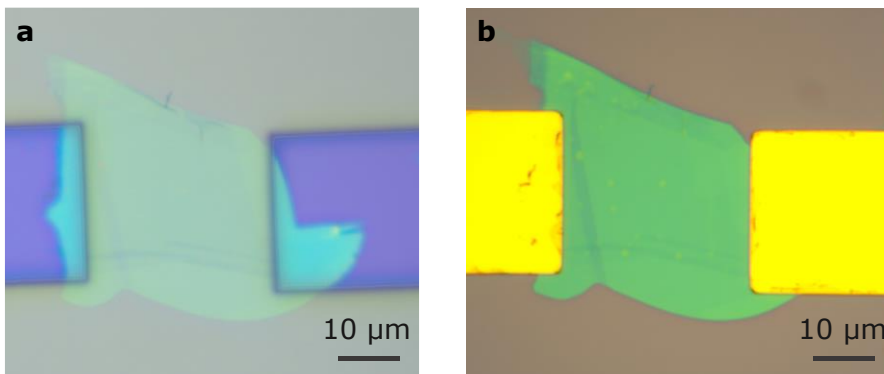


Figure 3.24: Optical images of a sample during and after fabrication of top contacts. a) Sample at step of fabrication shown in panels (a) of Figure 3.22 and Figure 3.23. b) Sample after evaporation and lift-off of the metallic contacts, as shown in panels (c) of Figure 3.22 and Figure 3.23.

Additional information 3.2.: Some tips for the encapsulation of graphene using hBN, and the fabrication of edge contacts

- Recommended thickness of hBN for encapsulating the graphene is around 20-40 nm: thinner flakes may break during the pick-up process, while thicker ones may difficult the optical location of the graphene flake underneath.
- During the etching step, it has been reported that doing 30 s etching cycles avoids cross linking the resist on the flake, allowing easier lift-off in the later step. Additionally, doing 10 s of O₂ etching (see recipe for PMMA in Table 3.5) can also help remove the hardened resist and ease the lift-off.
- It has been described in literature that the evaporation step should be performed under a 5° -15° tilt [127]. However, using a single layer of PMMA, the diffusion of Au during the evaporation, together with the slight, unavoidable tilt that comes from fixing the sample to the substrate holder and the rotation of the stage, is enough to create contact between Au and the graphene flake.

Additional information 3.3.: EBL patterning of large areas

- When defining the large areas at the EBL, such as big electrodes and pads, a write field correction may be needed, i.e., a correction layer shifted with respect to the original WF position to cover the limits of the original, avoiding gaps in the writing. For patterning this layer, we use the same EBL parameters.
- When changing from the 10 μm aperture to the 120 μm, the increase in current makes it difficult to focus using the new settings. It is possible to visualize some features on the substrate, such as markers or crosses, if we lower the brightness and contrast levels and try to correct the focus and astigmatism. However, it is important to correct the alignment using these marks, to make sure that the position of the patterns written using this aperture are exposed in the position where they were designed.

3.5.3. Fabrication of the single resonator using EBL

Once the graphene has been successfully contacted, we need to fabricate the single resonator on top, aligned so that the electrical contacts do not interfere with the resonance. Furthermore, to be able to characterize the sample in the THz regime, we need thick layers of gold (over 150 nm). While the total resonator area covers several mm, the smallest feature should be below 1 μm . This means that the EBL is more suitable for better defining these details and giving sharper features to the resonator.

First, in order not to have problems during the lift-off step, we spin coat the substrate with three layers of PMMA. Based on the DL PMMA recipe, we spin coat an additional layer of PMMA 495K A4 to achieve a higher thickness of PMMA. We spin coat each layer using an acceleration of 200 rpms, to avoid damaging the flakes, and at a speed of 4000 rpm for 60 s. After each spin coating, we bake the sample at 180°C for 90 seconds. Finally, we sputter 2.3 nm of Au as a conductive layer, for better focusing and definition with the electron beam.

Due to the difference of dimensions, we need to do the exposure in two steps, with different parameters that suit the particularities of each area. In both cases, we set the acceleration voltage to 10 kV, and will adapt suitably the remaining parameters. Since we are using positive resist, we need to write around the resonator and the vertical cut that will electrically separate the disk in two different areas, that will also act as electrodes. First, we define the center of the sample (Figure 3.25a). For the resonator and vertical cut, we use the 10 μm aperture, a dose of 90 $\mu\text{C}/\text{cm}^2$ base dose, and a step size of approximately 0.02 μm . The nominal width of the cut is 500 nm in the central 100 μm , opening to 2 μm for the 300 μm above and below the resonator (Figure 3.25b). For writing the disk and markers, and to align the sample with the aperture of the holder, we change the aperture to 120 μm for reaching a higher current. We expose the area with 130 $\mu\text{C}/\text{cm}^2$ dose and a 0.32 μm step size, using a 1000 μm WF and WF corrections (Figure 3.25c).

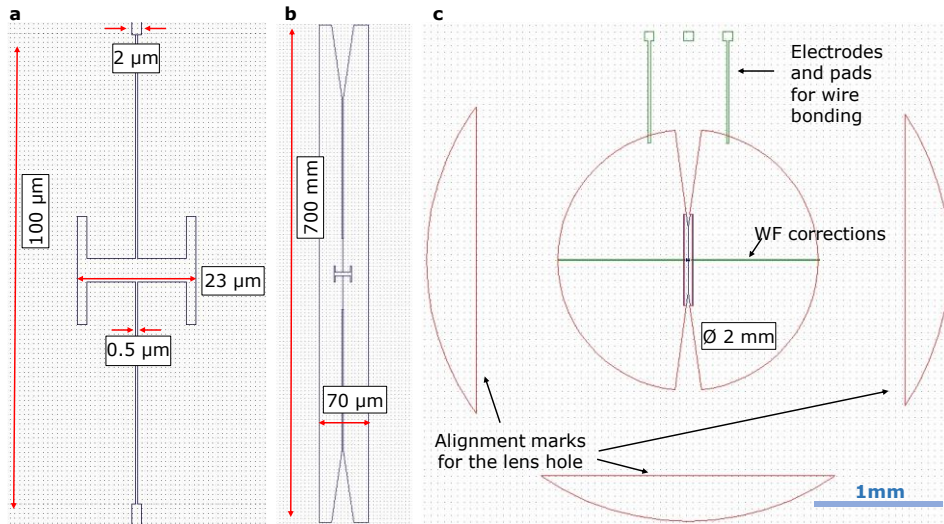


Figure 3.25: Design of the single THz resonator. a) Zoom into the resonator. b) Area of the design to be written using the 10 mm aperture, to define the central part of the disk, containing the smallest features, i.e., the resonator and the vertical cut. c) Complete design.

Finally, we clean the upper layer of gold immersing the sample 10s in Au etchant, rinsing in DI water twice and finishing with a rinse in IPA before developing in cold (-10°C) MIBK:IPA (1:3), for 30 s. We finish the developing step by rinsing the sample 30 s in IPA. These parameters are key to successfully develop the whole disk area, while we preserve the vertical resist line, that is key for the functionality of the sample. We finish the sample by evaporation of 10 nm of Ti and 150 nm of Au and lift-off in acetone. Since we use a thicker layer of PMMA, the lift-off of these samples is generally easy, and is done in about an hour. For even faster lift-off, we warm the acetone to 60°C , and check every 5-10 minutes to avoid completely evaporating the acetone. After this step and rinsing once again in IPA, the sample is ready to be measured.

3.5.4. Measurements and perspectives

The samples are characterized first at the probe station to make sure there is no leakage current from defects or pinholes on the SiO₂ film, since we need to apply a back gate to modulate graphene's Fermi level and be able to observe the coupling. We measure the sample at a probe station. We apply a voltage bias (V_{bias}) of 20 mV between the two electrodes that contact the graphene channel. Keeping the V_{bias} constant, we do a voltage sweep through a scratch in the SiO₂, that lets us access the doped Si below the SiO₂ layer (V_{gate}), as shown in Figure 3.26a. If there is no leakage current and we are able to characterize the charge neutrality point of the graphene flake (Figure 3.26b), to observe the USC regime we will need to replicate this measurement while we apply the THz field, to match the resonance frequency of the resonator to the cyclotron frequency of graphene. In the moment of writing this chapter, the work was focused on optimizing the sample holder to sustain electrical measurements together with the immersion lenses. A sample containing a graphene flake was measured at the THz set up, without any visible coupling, but the resonance frequency of the resonator was measured to be 1.5 THz, as it was designed.

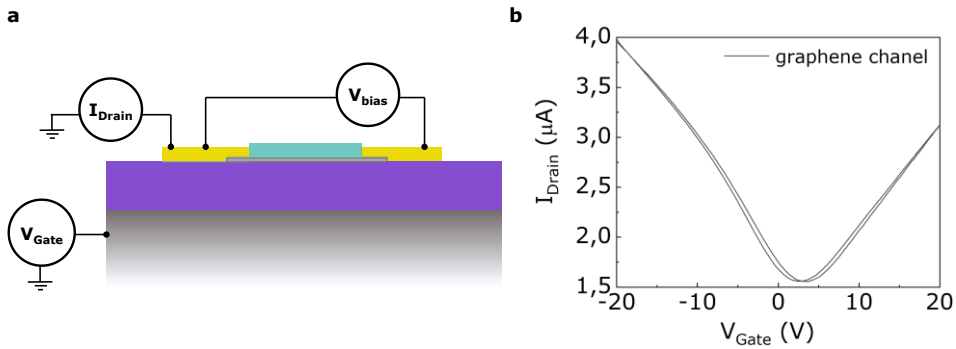


Figure 3.26: Back gate measurements of a graphene flake covered by hBN and electrically contacted with top electrodes. a) Determination of the charge neutrality point of the graphene flake by measuring the electrical current through the graphene of a voltage sweep of the gate voltage V_{Gate} , while the graphene channel is under a $V_{\text{Bias}} = 20$ mV. b) Schematics of the configuration for the measurement shown in (a).

3.6. Conclusions

In this chapter, we presented a series of samples fabricated through collaborative work within different projects. We described four distinct fabrication processes and summarized our findings for each one.

In the first case, we focused on fabricating micrometric arrays of nanoribbons on Si/SiO₂ substrates using Electron Beam Lithography (EBL). We were able to achieve ribbons with a width of 80 nm, separated by 45 nm, consistently over 20 μm . Surprisingly, we found that no proximity effect corrections were necessary despite the high density of the arrays. However, we observed that the actual measured widths of the ribbons were double the nominal widths specified in the design. This fabrication protocol was applied and optimized for the preparation of CVD grown ML-hBN nanoribbons, which exhibited high Q factors and sharp resonances, demonstrating the transferability of the process.

For the second project, we prepared non-concentric disk-ring nanocavities for magneto plasmonic studies using Electron Energy Loss Spectroscopy (EELS). Due to the small dimensions of the nanostructures, we patterned thin membranes to prepare non-concentric disk-rings nanocavities using EBL. First, we need to spin coat the sensitive resist over the membranes to prepare them for the lithography step. We determined that using low acceleration speeds and long spin coating times were crucial for obtaining homogeneous films. Baking the resist in a controlled atmosphere and ramping the temperature was essential to prevent thermal shocks that could cause the membranes to break. We also employed specific techniques to prevent shadowing effects during material evaporation. We observed that the writing mode in EBL had a significant impact on the final structures, especially on substrates with few backscattered electrons, as the ones used on this project. The concentric writing of rings proved to be the best mode for achieving round shapes on these thin membranes. Additionally, we found that the absence of backscattered electrons led to a lower effective dose during the patterning, resulting in the actual dose being double the nominal area dose of the resist. After these optimization steps, we successfully achieved the thinnest widths of rings, reaching 20 nm with a

separation of approximately 30 nm between the disk and the ring. These dimensions approached the nominal resolution limits of the techniques used.

On the other hand, we also optimized the process of patterning insulating substrates using EBL. We found that charge accumulation could distort the final dimensions of the structures. To mitigate this effect, we covered the resist with a conductive layer, either a thin layer of gold or a second spin-coated layer of a conductive resist. Adjusting the exposure to lower area doses was also necessary to ensure accurate definition of the structures. By following these steps, we successfully fabricated nano resonators on CaF_2 substrates. We achieved micrometric arrays of nanoresonators with dimensions of 30×50 nm, separated by gaps below 30 nm.

In the final project described in this chapter, we combined lithography techniques to pattern and electrically contact a single THz resonator on a graphene/hBN heterostructure. We designed a fabrication process consisting of three distinct steps. Firstly, we fabricated the heterostructure using the PC membrane technique, transferring large graphene and hBN flakes onto Si/SiO₂ substrates. Next, we designed electrodes using EBL and electrically contacted the heterostructure by selectively removing the hBN and evaporating Ti/Au. We successfully characterized the charge neutrality point of the graphene below the hBN flake. Finally, we fabricated the resonator aligned with the contacted heterostructure, divided into two separate regions by a 500 nm gap over 1 mm on each side of the resonator. These dimensions approached the resolution limit of the Direct Laser Writing (DLW) technique and posed a challenge for EBL, which is primarily focused on nanometric features. To overcome this, we modified the sample preparation by spin coating three layers of PMMA instead of the standard DL PMMA, resulting in a higher resist thickness required for the subsequent lift-off step. After optimizing the process, we successfully obtained a vertical cut of 500 nm along the approximately 2 mm disk surrounding the resonator. The working samples were then characterized at the THz set-up.

Overall, through these projects, we gained insights into various fabrication processes, dimensions and substrates, and their impact on the final structures.

We have optimized the fabrication protocols to achieve nanometric features on different substrates, adjusted exposure doses for accurate definition, and successfully fabricated complex structures such as nanoribbons, nanocavities, nanoresonators, and THz resonators. These findings contribute to the advancement of fabrication techniques and expand the possibilities for future research in nanotechnology and spectroscopic measurements.

3.7. Appendices: fabrication recipes

3.7.1. Parameters for electrical contacts at the EBL

	Write Field	Aperture	Step size	Dose
Narrow contacts	100 μm	10 μm	0.020 μm	120 $\mu\text{C}/\text{cm}^2$
Big electrodes and pads	1000 μm	120 μm	0.300 μm	170 $\mu\text{C}/\text{cm}^2$

Developing by 60s immersion in room temperature MIBK:IPA (1:3) and rinse in IPA

Table 3.4: Standard recipe for patterning electrical contacts at the EBL for DL of PMMA, and acceleration voltage of 10kV.

3.7.2. RIE recipes

ID	Material	Rate	Pressure	Power	DC bias	Gas	Flow
1	hBN	~ 5 nm/s	60 mbar	35 W	65 V	SF ₆	10 sscm
2	hBN (fast)	~ 30 nm/s	100 mbar	100 W	97 V	Ar SF ₆	10 sscm 10 sscm
3	hBN Graphene SiO ₂	~ 0.6 nm/s ~ 0.1 nm/s > 1 nm/s	40 mbar	60 W	240 V	CHF ₃ O ₂	40 sscm 4 sscm
4	SiO ₂	~ 40 nm/s	30 mbar	200 W	540V	Ar CHF ₃	38 sscm 12 sscm
5	PMMA	-	10 mbar	50 W	215 V	O ₂	10 sscm

Table 3.5: Etching recipes for RIE.

3.7.3. Ion Miller recipes

Recipe	Rate	V _{Beam}	I _{Beam}	V _{acc}	Angle
SiO₂ milling	6.3 nm/min	600 V	50 mA	50 V	260°
SiO₂ milling	3.6 nm/min	300 V	50 mA	300 V	260°
Au milling	14.4 nm/min	300 V	50 mA	50 V	260°

Table 3.6: Ion milling recipes.

4 ● Strain modulation of the photoluminescence of 2D perovskites

The application of external mechanical strain is an effective technique to change the optoelectronic properties of some 2D materials. It is known to affect optical, electrical, and magnetic properties, and even trigger phase transitions [128–130]. Interestingly, 2D materials are more sensitive to strain, and have in general stronger deformation capacity than bulk materials. Different methods for applying strain have been explored, from placing flakes on pre-strained substrates, and causing wrinkles when they recover their original shape, to flexible polymer-based substrates, that cause a deformation on the flake when they bend [131,132]. In this chapter, we target the modulation of the photoluminescence (PL) emission of 2D hybrid organic-inorganic metal-halide perovskite (HOIP) flakes by strain engineering, by placing the flakes on SiO₂ micro rings. We study the effect of strain on their optical and vibrational properties by temperature-dependent spectroscopy measurements [133]. This chapter is an extended version of the Nano Letters publication [133] (see permissions in appendix 4.6.3) and provides more details on the fabrication and experimental measurements. The work was done in collaboration with the Leibniz Institute for High Performance Microelectronics (IHP).

4.1. Selection of the composition and structure of the perovskite

Perovskites are compounds of the general chemical formula ABX_3 , where A and B are cations, positively charged, and X is an anion, negatively charge, leading to a 3D network of corner-sharing octahedra. For creating this structure, in the case of 3D HOIPs, A is a small-size cation (e.g. methylammonium or Cs^+), B is a metal, typically lead, and X is a halogen atom (Cl, Br or I). When replacing the A-site cation with large monovalent organic cations (A') leads to the formation of the layered (2D) HOIPs, whose formula is $A'_2A_{n-1}B_nX_{3n+1}$, where bilayers of monoammonium cations separate “n” layers of inorganic octahedra. These large organic cations allow to mechanically exfoliate bulk crystals in form of flakes in a similar way than graphene or other 2D materials. In recent years, both kind of HOIPs have attracted the attention of researchers due to their large absorption coefficients, high carrier mobilities and high PL quantum yield, that makes them suitable for a plethora of applications in optoelectronics [134–136], such as photodetectors [137–139], photovoltaics [140] and LEDs [141]. However, strain-based approaches have been namely explored to modify the properties of 3D HOIPs as thin films or during the synthesis of single crystals [135,142,143].

Compared to 3D HOIPs, the effect of strain on 2D HOIP flakes has been barely studied. However, they exhibit a dynamic crystalline structure that adapts and can resist up to a 6% of strain before breaking [144]. The distortion of the structure derives in the modification of their optoelectronic properties [145–147]. Moreover, it has been shown that the mechanical properties, and in particular the stiffness, of 2D HOIP flakes are dependent with the number of octahedra, n , between the organic layers, and the halide-organic composition [148–150].

To be able to perform mechanical studies on 2D HOIP flakes, we selected $(C_6H_5CH_2NH_3)_2(Cs)_3Pb_4Br_{13}$ ($n = 4$), a lead-bromide perovskite containing phenethylammonium ($C_6H_5CH_2NH_3^+ = PEA^+$) and Cs^+ as cations, which improves its stability under ambient conditions. Its $n = 4$ structure provides

stiffness making it sensitive to strain [144,146,148–150]. Figure 4.1.a shows the crystalline structure $(\text{PEA})_2\text{Pb}_4\text{Br}_{13}$ ($n = 1$), compared to that of $(\text{PEA})_2(\text{Cs})_3\text{Pb}_4\text{Br}_{13}$ ($n = 4$). The modulation of the optical properties with the number of octahedral layers, n , is also shown. The PL emission of the perovskite redshifts increasing “ n ” from $n = 1$, $n = 2$ and $n = 4$ as shown in Figure 4.1.b [151,152]. Furthermore, this material is stiffer than other 2D HOIPs explored in previous studies, as can be seen by comparing its Young’s modulus to that of other compounds, as is shown in Figure 4.2.

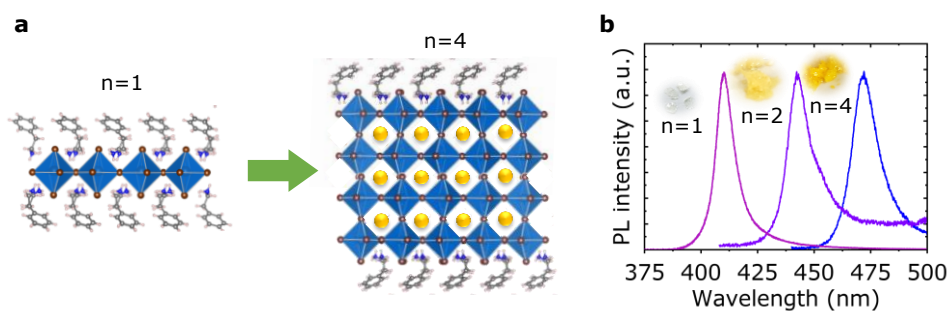


Figure 4.1: Description of the 2D perovskite used in this study. a) Schematic representation of a monolayer of the 2D HOIP $(\text{PEA})_2\text{Pb}_4\text{Br}_{13}$ ($n = 1$) and $(\text{PEA})_2(\text{Cs})_3\text{Pb}_4\text{Br}_{13}$ ($n = 4$). b) Evolution of the photoluminescence spectra with the number of octahedral layers, n , showing the shift of the PL peak with n . Insets show a sample of the synthesized crystals for $n = 1, 2$ and 4 , already showing a noticeable color difference. Reprinted with permission from [133]. Copyright © 2022, American Chemical Society.

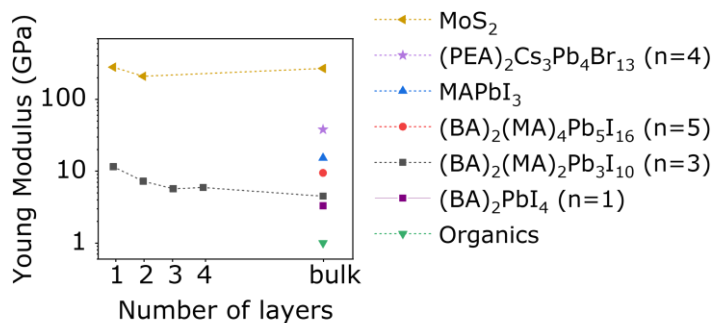


Figure 4.2: Young modulus of different materials as a function of the number of layers [144,146,148].

4.2. Transfer of 2D HOIP flakes on SiO₂ rings

4.2.1. Preparation of rings on SiO₂/Si substrates

We use a SiO₂ ring as platform for biaxial strain since it provides both support for bending and a free space in the center for the flake to accommodate the strain in the suspended areas. We prepare the rings structuring commercial Si/SiO₂ substrates. The substrates consist, as in previous chapters, of 300 nm of SiO₂ thermally grown on Si. Using DLW and ion miller to define the structures, we pattern the surface of the substrates to form the rings. A schematic following the fabrication steps is shown in Figure 4.3.

We design arrays of 10x10 rings, spaced from 25 μm to 50 μm. Since we need to mill the SiO₂ surface, we need to create a mask that protects the ring lines. For this purpose, we used the negative resist AZ n-lof 2070⁸, that we spin coat on the substrates using a speed of 4000 rpm for 60 s, with an acceleration 2000 rpms. This leads to the formation of a layer of approximately 6 μm thick (Figure 4.3a,b). Following the manufacturer's instructions, we bake the resist at 115°C for 60 s to evaporate the solvents. After exposing the rings at the DLW, we do a post bake again at 115°C for another 60 s. This step is crucial for defining the structures on the resist, since it finishes hardening the exposed areas, that will stay on the substrate forming our design. We develop the sample for 90 s in AZ 726 MIF and rinse the sample in DI water. The sample is then ready for the milling step (Figure 4.3c).

With the resist mask forming hollow pillars on the surface of the substrate, we now need to etch down the substrate to obtain the rings. We load the sample in the ion miller and run the SiO₂ etching recipe (See Chapter 3 for details), to etch the SiO₂ film through the ring height that we want to obtain. Finally, we remove the resist mask by leaving the sample in acetone overnight, and then remove any remaining residues by placing the sample 5 min in ultrasounds immersed in clean acetone. Finally, we clean the sample by ultrasonication in

⁸ https://www.microchemicals.com/products/photoresists/az_nlof_2070.html

IPA for 5 min and drying it with the N₂ gun. Following these steps, we have the sample ready for characterization of the rings, as shown in Figure 4.3d.

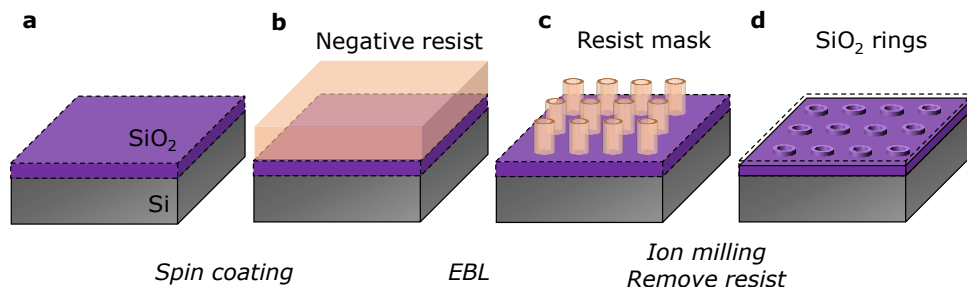


Figure 4.3: Fabrication of SiO₂ rings as platform for generating strain on perovskite flakes. a) Si/SiO₂ substrate on which the rings previous to the fabrication of the rings. b) After spin coating the substrate with a layer of the negative resist AZ n-lof 2070, we pattern the rings using EBL. c) Array of hollow pillars that act as a mask, obtained by developing the resist after the EBL step. d) SiO₂ rings after cleaning the resist, defined on the surface of the substrate by ion milling.

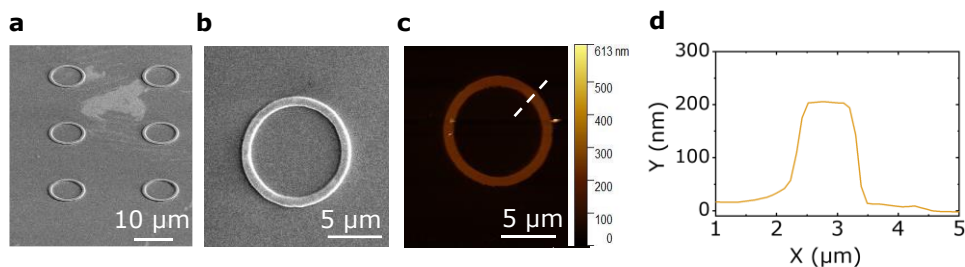


Figure 4.4: Characterization rings of 200 nm of height on SiO₂/Si substrates; a) SEM image of an array of rings. b) SEM image of one ring, as the one shown in (c). c) AFM topography image of a ring as the one shown in (b). d) AFM profile of the ring following the white dashed line in (c).

We fabricate arrays of rings with different diameters and heights, to characterize the flakes while placed on similar structures of different dimensions. As mentioned at the beginning of the chapter, we use substrates with a thermally grown film of SiO₂, of a thickness of 300 nm. The purpose is to preserve the same material on the ring and the substrate, to avoid changing the dielectric environment below the flake, that could cause variations on its PL.

Hence, the maximum ring height that we can fabricate on these substrates is slightly below 300 nm. We choose to fabricate rings of 100, 200 and 260 nm of height. The ring width was fixed to 1 μm , while the diameters were 5, 10 and 15 μm . We checked the dimensions of the rings, as well as the absence of resist residues on the rings, by using atomic force microscopy (AFM) and scanning electron microscopy (SEM). As an example, the characterization of one ring is shown in Figure 4.4. Furthermore, AFM characterization a ring of each type is shown at the end of this chapter, in Figure 4.12.

Additional information 4.1.: Fabrication using negative resists

- Resist AZ n-lof 2070, and, in general, negative resists, do not have good adhesion to the substrates. Hence, it is recommended to leave the sample still in the recipient during the developing step, instead of shaking it. During the rinse steps, it is also better not to shake the sample in the water.
- To obtain better lithography results, development can be done in two steps. First, do 45 s of developing, then change the sample to clean developer for the rest of the developing time.

4.2.2. Exfoliation and transfer of 2D perovskites on microstructures

(PEA)₂Cs₃Pb₄Br₁₃ (n=4) flakes are obtained by micro mechanical exfoliation from the synthesized crystals (Figure 4.5a) on PDMS stamps. For the first step of exfoliation, we place some crystals on a clean piece of blue Nitto tape. This material is soft for exfoliation, and we only need to peel-off the blue tape a couple of times before transferring the resulting flakes to the PDMS stamp. This is enough to obtain multiple flakes of different thicknesses, ranging from 10-20 nm, to slabs of several hundreds of nm (Figure 4.5b). Optical contrast allows characterization by optical inspection at the microscope up to approximately a micrometer, moment on which they turn to silver grey and stop showing color-

contrast. We observed that the flakes have to be thick enough to undergo the strain without breaking while simultaneously thin enough to be sensitive to it. We find that the appropriate thickness is approximately 200 nm, by placing flakes of different thicknesses on the rings.

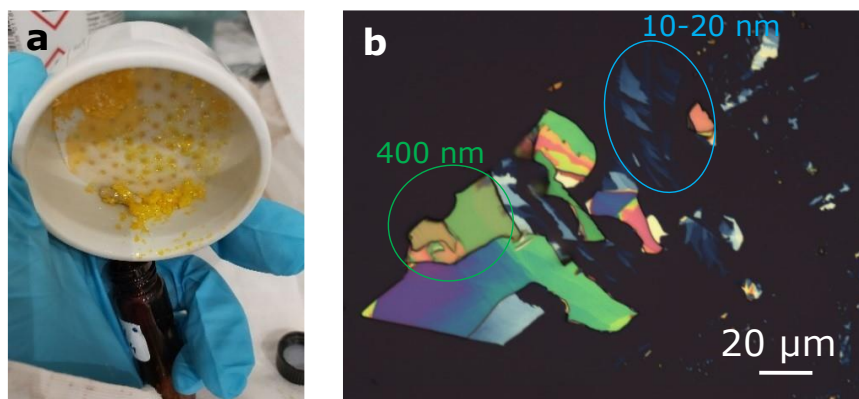


Figure 4.5: Optical images of 2D $(\text{PEA})_2\text{Cs}_3\text{Pb}_4\text{Br}_{13}$ ($n = 4$). a) Synthesized $(\text{PEA})_2\text{Cs}_3\text{Pb}_4\text{Br}_{13}$ ($n = 4$) bulk crystals. b) Flakes of different thicknesses, from approximately 10 to 400 nm, transferred on a PDMS stamp, after exfoliation from the crystal shown in (b).

To determine their original PL and confirm their $n = 4$ nature, we characterize the flakes by Raman spectroscopy directly on the PDMS stamp, before transferring them on the rings. Once some $n = 4$ flakes 200 nm thick have been identified, we can transfer them from the PDMS to the rings, following the protocol for the all-dry viscoelastic transfer [32] as shown in chapter 1. The rings are fabricated in arrays so that several of them can be covered with the same flake (Figure 4.6a). After transfer, the structures are again characterized at the AFM, showing the formation of domes, as can be seen in Figure 4.6b,c. This effect is studied for all the ring sizes, and an example of the AFM characterization of flakes on rings of each type is shown in Figure 4.13. It can be observed that the domes form for all ring sizes for flakes ranging from 60 nm up to 600 nm, except for the thinnest and widest (Figure 4.13c), on which the flake adapts to the ring but is not able to sustain the dome. Flakes bigger than 600 nm do not stick on the rings, since they exhibit almost bulk

behavior and are too stiff to adapt to the deformation. Too thin flakes, on the other hand, experience too much strain and break during the transfer step.

After transfer, some of the flakes placed on the rings were also characterized by SEM, to better understand the deformation. Figure 4.7a shows the general view of a flake transferred on top of the rings, completely covering two of them. By zooming into one of the covered rings, we can directly observe the resulting structure (Figure 4.7b). Finally, Figure 4.7c shows a flake transferred halfway on the rings show the formation of a gap between the flake and the substrate, free-standing over the inner part of the ring.

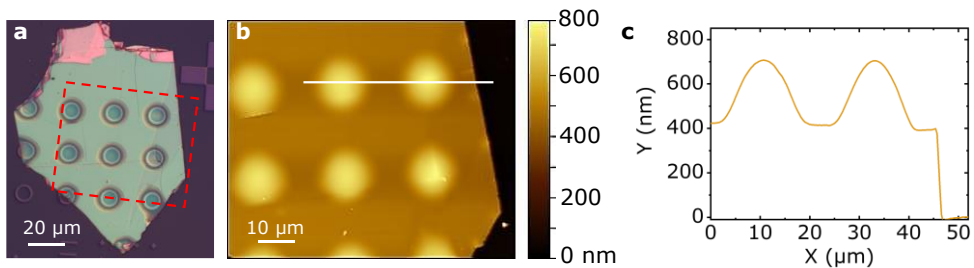


Figure 4.6: Characterization of the domes created by the flake on the rings. a) Optical image of a flake covering several rings. b) AFM image of the area marked by a red line in (a). c) AFM profile of the white line indicated in (b). Reprinted with permission from [133]. Copyright © 2022, American Chemical Society.

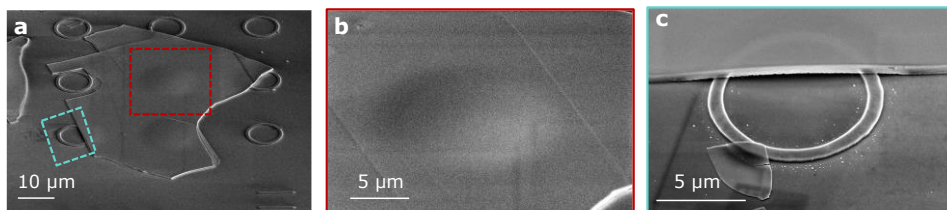


Figure 4.7: SEM images of a flake transferred on an array of rings. a) Flake completely covering two rings. Red and blue lines indicate the areas depicted in (b) and (c). b) Zoom into one of the rings covered by the flake, where the formation of a dome can be observed. c) Edge of the flake partially covering the ring. The stiffness of the flake is enough to keep itself freestanding over the center of the ring, without touching the substrate.

4.3. Photoluminescence and Raman spectroscopy studies

We study the effect that the deformation due to the dome formation has in the optical properties of the perovskite flakes. First, we perform micro-PL measurements at room temperature and down to 80 K. At room temperature, we find a slight shift of about 1 nm, and broadening of approximately 2 nm, of the PL peak of the flakes on the rings with respect to the flakes on the unstructured SiO_2 , already demonstrating changes arising from the strain (Figure 4.8a,b). However, at lower temperature, we observe more dramatic changes.

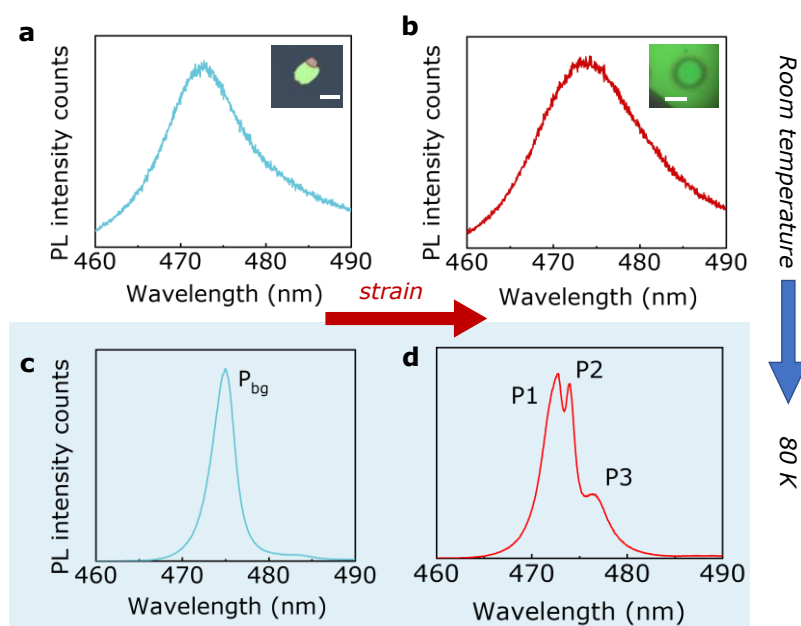


Figure 4.8: Comparison of the PL spectra of the unstrained and strained flakes at room and low temperature. a) PL of unstrained flake at room temperature. b) PL of a flake placed on a ring at room temperature, showing a slight broadening compared with the PL spectrum show in (a). c) PL of unstrained flake at 80K, on which a single peak coming from the bandgap appears, P_{bg} . d) PL spectrum of a flake on a ring at 80K, evincing three PL peaks, P1, P2 and P3. Reprinted with permission from [133]. Copyright © 2022, American Chemical Society.

When the temperature is lowered, the PL peak of unstrained flakes becomes narrower, from 11 nm down to approximately 3 nm, allowing the reveal of features on the strained flakes that were covered by the width of the spectra at room temperature. At 80 K, unstrained flakes on Si/SiO₂ substrates show a single, narrow (approximately 3 nm of width) PL peak corresponding to the bandgap of the perovskite, at 474 ± 1 nm (Figure 4.8c). On the contrary, on the PL spectra of the strained flakes we can clearly identify two new peaks, P1 and P3, around the position of the original PL peak (P2), that also remains visible and centered at the same wavelength: $P1 = 472.0 \pm 0.5$ nm, $P2 = 474.0 \pm 0.5$ nm, and $P3 = 477.0 \pm 0.5$ nm (Figure 4.8d). P1 and P3 peaks are respectively blue and red shifted with respect to the P2 peak, that, as stated before, corresponds to the bandgap. These new peaks appear from the straining of the flakes on the rings, arising from changes in the bandgap due to compressive and tensile strain [144,146,153–155], already indicating the presence of these two types of strain on the flakes. Additionally, we observe a decrease in the P1/P2 and P3/P2 ratios when increasing the temperature, revealing that not only the formation of the dome but also the mismatch of the thermal expansion coefficients of the SiO₂ and the perovskite contributes to strain the flake [156,157]. Maps showing these ratios on strained flakes are shown in Figure 4.9 and Figure 4.10b,c.

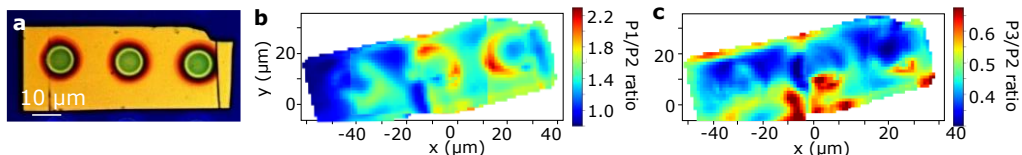


Figure 4.9: Micro-PL maps on strained flake at 80K. a) Optical image of the perovskite flake covering three rings of 200 nm of height and 10 μm diameter. b,c) micro-PL maps of the flake shown in (a), showing an increase of the P1 and P3 emission vs. the intensity of P2, particularly around the SiO₂ rings. Reprinted with permission from [133]. Copyright © 2022, American Chemical Society.

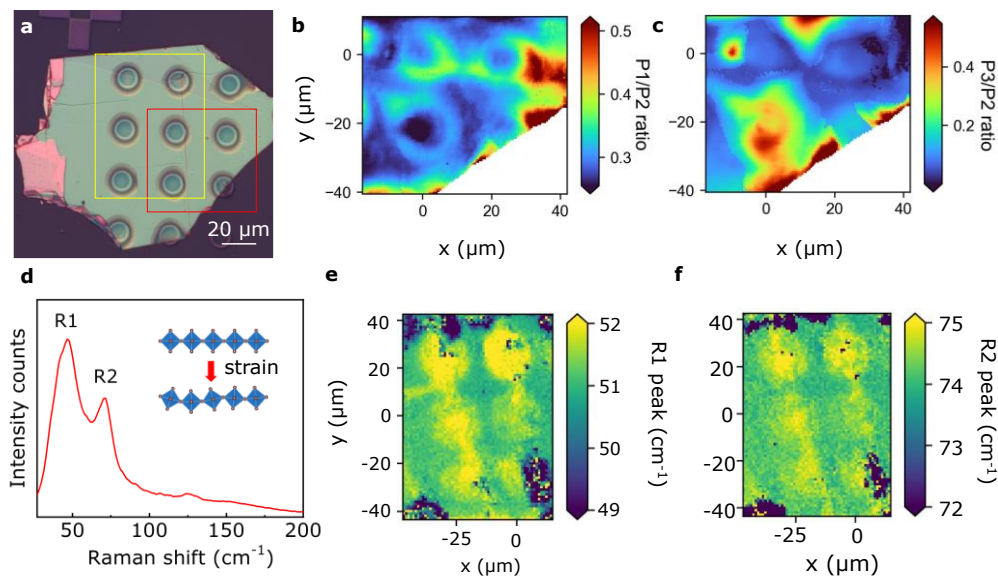


Figure 4.10: Micro-PL and Raman study of a strained flake. a) Optical image of a flake on a SiO_2 ring, with height 200 nm and diameter $10\ \mu\text{m}$. Red line frame the areas on which the micro-PL maps shown in (b) and (c) were measured, whereas the yellow line frames the areas on which Raman maps in (e) and (f) were measured. b, c) Micro-PL maps of the flake shown in (a), taken at 80 K, where the increase in the intensity of P1 and P3 against that of P2 around the SiO_2 ring can be observed. d) Raman spectrum of the strained, showing the modes under study, R1 and R2. Inset shows a schematic of the distortion of the octahedra due to the application of strain. e, f) Raman maps for the R1 and R2 modes corresponding to the areas marked by a yellow box in (a), showing a shift of the peaks around the SiO_2 rings. Reprinted with permission from [133]. Copyright © 2022, American Chemical Society.

To further identify the origin of the new features and the nature of the strain, we perform micro-Raman spectroscopy on the samples using a 532 nm laser. We study the vibrational modes of the perovskite, $\text{R1} \sim 48\ \text{cm}^{-1}$ and $\text{R2} \sim 72\ \text{cm}^{-1}$ (Figure 4.10d-f), associated with the distortion of the inorganic octahedra [158] and the displacement of the Cs^+ atoms [159]. Lowering the temperature down to 80 K, we observe a progressive shift of the peaks to lower frequencies. Additionally, there is a correlation between the shift of the Raman modes and the P1 PL peak, since the largest redshifts of the R1, R2 Raman modes correspond to the areas with highest P1/P2 ratio. The redshift of both

R1 and R2 Raman modes indicates that the accommodation to the strain is done by the inorganic layers, while the organic molecules remain less sensitive to the strain. Thus, the material adapts to tensile strain by tilting the inorganic $[\text{PbBr}_6]^{4+}$ octahedra to relax the crystal lattice, causing a slight lattice expansion and the opening of the bandgap, that leads to the appearance of the new PL peak P1 at 472 nm [160]. On the other hand, the presence of P2 means that the strain is not homogeneous throughout the whole flake, and that some areas remain unstrained and exhibit the original bandgap.

Finally, P3 can come either from compressive strain or from defects induced by the strain [152,154]. In the case of the defects, we should observe a dependence to the power excitation [161,162], that we do not obtain with power-dependence experiments. Therefore, P3 must come from compressive strain. To confirm this assignation and reconstruct the mechanical behavior of the flakes on the rings, we performed numerical simulations, presented in the next section.

4.4. Reconstruction of mechanical behavior via reverse engineering

Analysis of the radius of curvature obtained via AFM characterization reveals that PL emission is modified on flakes that show strain $<1\%$. The strain on the flakes, ε , can be estimated from the AFM images as a function of the curvature radius of the domes, R , and the flakes thickness, h , as shown in equation (2). R is determined by equation (3), where σ and ω are the height and the diameter of the dome, respectively. This estimation yields strain ranging from 0.07 to 0.4 % (Table 4.1), evincing that we are within the range of previous works, in which strain ranges between 0 to 1.72 % [145,146].

$$\varepsilon = \frac{h}{2 \cdot R} \quad (2)$$

$$R^2 = (R - \sigma)^2 + \left(\frac{\omega}{2}\right)^2 \quad (3)$$

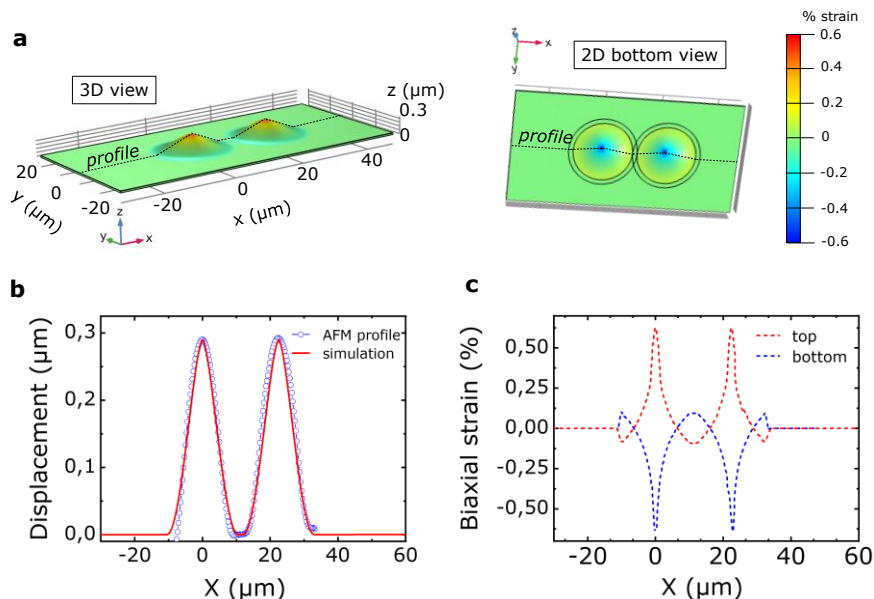


Figure 4.11: Finite element simulations of the domes formed on the SiO₂ rings carried out at 80 K. a) 3D top view (left) and 2D bottom view (right) of two domes, of a 400 nm flake on a 200 nm high and 10 μm diameter SiO₂ ring, where the color scale shows the strain distribution over the flake. The circles on the bottom view indicate the ring's anchor points. b) Comparison of the AFM profile of two domes. Red line indicates the simulation of the profile, whereas blue line and circles correspond to the experimental data. c) Strain profiles taken from the dashed lines indicated in (a). Reprinted with permission from [133]. Copyright © 2022, American Chemical Society.

These numbers are confirmed by numerical simulations, by reconstructing the formation of the domes from AFM data via finite element simulations [163]. On the rings, the flake does not experience strain in the vertical direction, but biaxial in the plane of the flake. We find a coexistence of tensile and compressive strain, with the maximums on the center of the rings, on top and bottom of the flake, respectively (Figure 4.11). This distribution of tensile (P1 emission) and compressive (P3) strain is provoked by the presence of the ring and the thermal strain, as the difference on the PL emission are enhanced at low temperatures. We find that equilibrium is localized of the top of the dome, but is inverted in the ring border, with the local maximum of the compressive strain on the upper surface of the flake, and that of the tensile strain on the bottom surface, in contact with the SiO₂ ring. This is interesting as this is the point of contact

between the rings and the flakes and explains the absence of thermal-induced strain in flakes transferred to unstructured SiO₂. On these flakes, thermal-induced deformation and strain are homogeneously distributed throughout all the flakes. However, on the domes, the flake is only in contact with the SiO₂ on the edges of the rings, causing different deformation on those areas and the parts of the flake that form the dome and do not have contact with the structures.

4.5. Conclusions

We have demonstrated strain engineering as an efficient strategy to modulate the bandgap of 2D (PEA)₂Cs₃Pb₄Br₁₃ ($n = 4$) flakes without changing the composition of the materials, on a device-compatible platform. The mechanical properties of the flake allow us to detect a strain <1%. We find the formation of new PL peaks can be explained as a combination of both mechanical and thermal strain. We have observed a coexistence of both tensile and compressive strain, while maintaining the original PL emission.

4.6. Appendices

4.6.1. AFM study

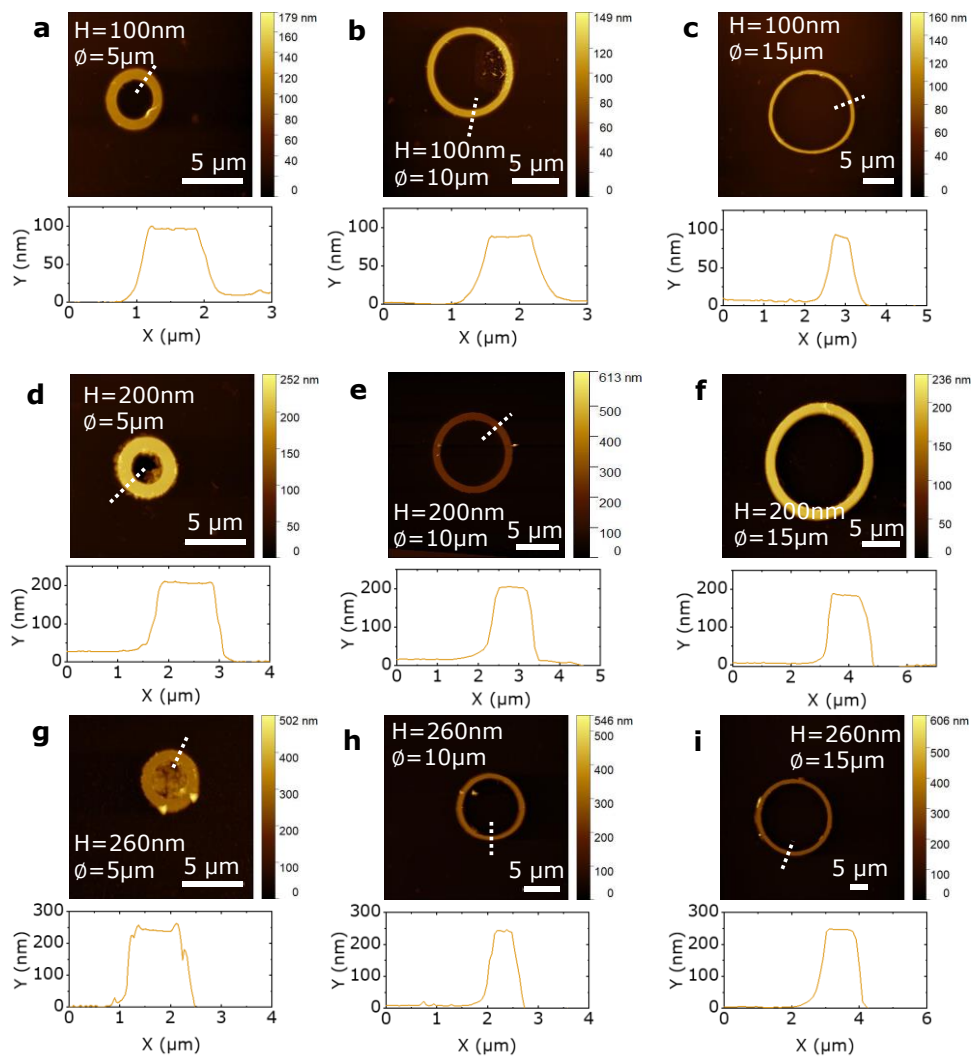


Figure 4.12: AFM characterization of the SiO_2 rings of different height, H , and diameters, \varnothing . Some resist residues stayed on the rings after fabrication for the smallest diameters. Particularly, for the case of $H = 260 \text{ nm}$ and $\varnothing = 5 \mu\text{m}$ shown in (g), the central part of the ring is filled with resist residues, but they do not interfere in the formation of the dome as they stay below the height of the ring.

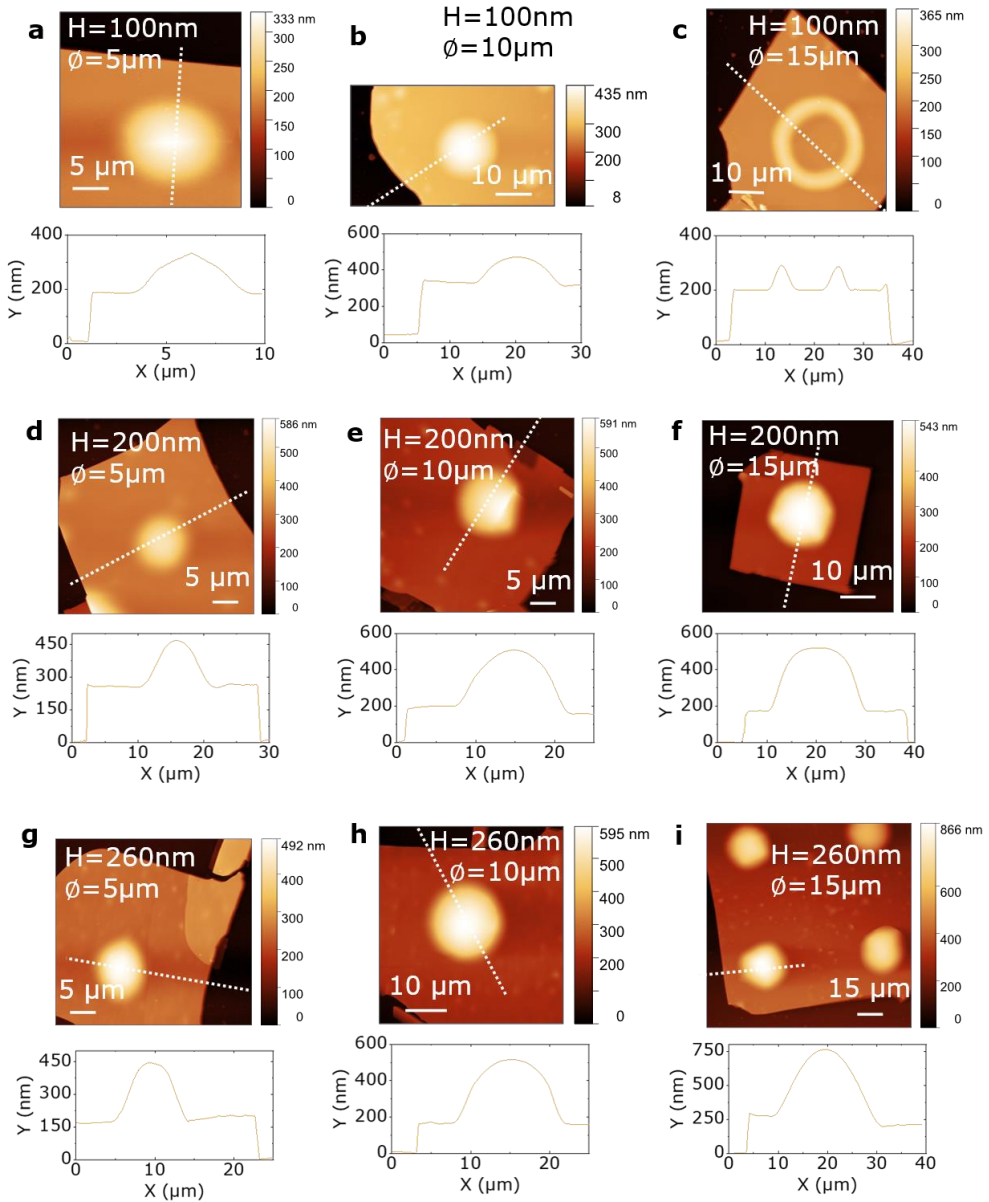


Figure 4.13: AFM characterization of the flakes after transfer to the SiO_2 rings, revealing the formation of domes for every case except for the one shown in (c), in which the diameter/height of the ring ratio is enough to allow the flake to adapt to the structure.

4.6.2. Estimation of the strain from the AFM profiles

Sample	Flake thickness h (nm)	Ring dimensions		Dome dimensions		Radius of curvature R (nm)	% strain ϵ
		Height H (nm)	Diameter \varnothing (μm)	Height σ (nm)	Diameter ω (μm)		
1	200	100	5	140	6	32.2	0.31
2	80			100	3	11.3	0.35
3	60			85	6	53.0	0.06
4	150			120	7	51.1	0.15
5	180		10	180	12	100.1	0.09
6	300			150	14	163.4	0.09
7	300			160	14	153.2	0.10
8	200		15	80	5	39.1	0.26
9	200			80	5	39.1	0.26
10	160			100	4	20.1	0.40
11	300	200	5	230	11	65.9	0.23
12	280			210	11	72.1	0.19
13	200		10	330	14	74.4	0.13
14	300			280	17	129.2	0.12
15	600			270	17	136.3	0.23
16	500			400	15.5	75.4	0.33
17	420			275	19.5	173.2	0.12
18	200		15	370	20	135.3	0.07
19	200			360	20	139.1	0.07
20	360			270	22	224.2	0.08
21	160	260	5	280	10	44.8	0.18
22	600			260	17	139.1	0.22
23	150		10	350	13	60.5	0.12
24	250			360	15	78.3	0.16
25	280			300	17	120.6	0.12
26	400			250	19	180.6	0.11
27	240			15	490	21	112.7
28	200		580		18	70.1	0.14

Table 4.1: Study of the generate strain as a function of the dome dimensions, in terms of the radius of curvature (R) for different $(\text{PEA})_2\text{Cs}_3\text{Pb}_4\text{Br}_{13}$ ($n=4$) flakes (thickness, h) and SiO_2 ring dimensions (height σ / diameter ω) for the 28 samples fabricated for this study, including the estimation of the strain (ϵ) as $\epsilon=h/(2 \cdot R)$.

4.6.3. Publisher permission

RightsLink



Tailoring Photoluminescence by Strain-Engineering in Layered Perovskite Flakes

Author: Davide Spirito, María Barra-Burillo, Francesco Calavalle, et al
Publication: Nano Letters
Publisher: American Chemical Society
Date: May 1, 2022

Copyright ©2022 American Chemical Society

PERMISSION/LICENSE IS GRANTED FOR YOUR ORDER AT NO CHARGE

This type of permission/license, instead of the standard Terms and Conditions, is sent to you because no fee is being charged for your order. Please note the following:

- Permission is granted for your request in both print and electronic formats, and translations.
- If figures and/or tables were requested, they may be adapted or used in part.
- Please print this page for your records and send a copy of it to your publisher/graduate school.
- Appropriate credit for the requested material should be given as follows: "Reprinted (adapted) with permission from {COMPLETE REFERENCE CITATION}, Copyright {YEAR} American Chemical Society." Insert appropriate information in place of the capitalized words.
- One-time permission is granted only for the use specified in your RightsLink request. No additional uses are granted (such as derivative works or other editions). For any uses, please submit a new request.

If credit is given to another source for the material you requested from RightsLink, permission must be obtained from that source.

[BACK](#) [CLOSE WINDOW](#)

5 • Phonon-photon coupling in microcavities filled with hBN

Strong coupling between molecular vibrations and microcavity modes has been demonstrated to modify physical and chemical properties of the molecular material. Here, we study the less explored coupling between lattice vibrations (phonons) and microcavity modes. Embedding thin layers of hexagonal boron nitride (hBN) into classical microcavities, we demonstrate the evolution from weak to ultrastrong phonon-photon coupling when the hBN thickness is increased from a few nanometers to a fully filled cavity. Remarkably, strong coupling is achieved for hBN layers as thin as 10 nm. Further, the ultrastrong coupling in fully filled cavities yields a polariton dispersion matching that of phonon polaritons in bulk hBN, highlighting that the maximum light-matter coupling in microcavities is limited to the coupling strength between photons and the bulk material. Tunable cavity phonon polaritons could become a versatile platform for studying how the coupling strength between photons and phonons may modify the properties of polar crystals. This chapter is an extended version of the Nature Communications publication [164], and provides a more detailed explanation on the fabrication and experimental measurements of the microcavities. All theory calculations and simulations were done by U. Muniain at Donostia International Physics Center (DIPC) and Centro de Física de Materiales (CFM).

5.1. Introduction

When light strongly couples to matter, new hybrid modes – polaritons - can emerge, whose coherent exchange of energy is faster than the decay rate of the original photonic modes and matter excitations [116,165]. Typically, polariton waves are created by placing matter inside an optical resonator, such as a Fabry Perot microcavity [166,167]. The interaction between visible light and excitonic systems has been widely explored over the past decades [168,169], leading to fundamental and applied advancements in the field, including the realization of polariton Bose Einstein condensates [170,171] and various excitonic LASER systems [172]. In analogue fashion, strong coupling in the infrared regime has been explored in semiconductor quantum wells [173–176], polar dielectrics [177], and molecular aggregates [178]. In particular, strong coupling (SC) between infrared light and molecular vibrations (vibrational strong coupling, VSC) has emerged as a new intriguing research topic, after it has been reported that this phenomenon can lead to modification of fundamental material properties, triggering, for example, phase transitions [179] or modifying chemical reactions [117,180]. In the reported experiments, strong coupling was achieved by filling classical Fabry-Pérot microcavities with molecules. Recently, molecular vibrational strong coupling could be achieved even on the nanometer scale, by exploiting phonon polaritons in h-BN nanoresonators [91] and slabs [181], the phonon polaritons by themselves being the results of strong coupling between infrared photons and phonons.

The strong and ultrastrong coupling between light and phonons offers intriguing possibilities for various fundamental studies and applications, including polaritonic control of THz waves in polar crystals [182], which in combination with microresonators [183,184], can be used for the development of phonon polariton lasers [185,186]. At surfaces or on thin layers of polar crystals, strong photon-phonon coupling can also lead to surface phonon polaritons and hyperbolic volume phonon polaritons [187,188] that allow for nanoscale concentration of infrared and terahertz fields, which could lead to novel communication and sensing technologies [189,190], particularly in form

of nanoresonators [187,191,192] or by coupling the polaritons with plasmonic antennas and metasurfaces [120,193–196]. Remarkably, a detailed study and control of the coupling strength between photons and phonons in classical Fabry-Perot microcavities is relatively unexplored terrain. This might be related to the difficulty to fabricate high-quality thin crystal layers of arbitrary thickness and place them inside the microcavities. As phonons have significant influence on many physical properties of crystals [197], such as on electrical and thermal conductivity, ferroelectricity [198,199] and superconductivity [200], controlling the coupling strength between infrared photons and phonons in microcavities may become an interesting platform for future fundamental and applied studies. For example, recent studies suggest that cavity-mediated strong light-phonon coupling may trigger quantum phase transitions without the need of an external pump [118,201].

Here we demonstrate infrared microcavities comprising polar van der Waals (vdW) materials as a versatile test bench to study the interaction of optical phonons and photons [164]⁹. Importantly, the layered structure of vdW materials allows for convenient exfoliation of high-quality crystalline layers of virtually any thickness for studying the evolution of the phonon-photon coupling strengths as a function of layer thickness. Specifically, we study in this work microcavities containing high-quality layers of hexagonal Boron Nitride (hBN), which is an insulating polar material exhibiting phonons in the mid-infrared (IR) spectral range [202]. The layered nature of hBN is illustrated in Figure 5.1. The experimental reflectivity of the hBN-microcavity system is well described by electro-dynamical calculations based on the transfer matrix method [203]. Furthermore, by describing this system by two classical coupled harmonic oscillators [204–206], we estimate the coupling strength between the cavity modes and the phonon excitation. We demonstrate that strong coupling can be achieved for layers as thin as a few nanometers, leading to the formation of microcavity phonon polaritons. We further systematically trace the evolution

⁹ All theoretical studies and calculations presented in this chapter were done by U. Muniain. Further details of these calculations can be found in the Supplementary Information of reference [164].

from the weak to the ultrastrong coupling (USC) regime [115,207–209]. The high crystal quality and adjustable layer thickness, both achieved by simple exfoliation, establish microcavities embedding van der Waals materials as a versatile platform for studying and tuning the coupling strengths between photons and optical phonons.

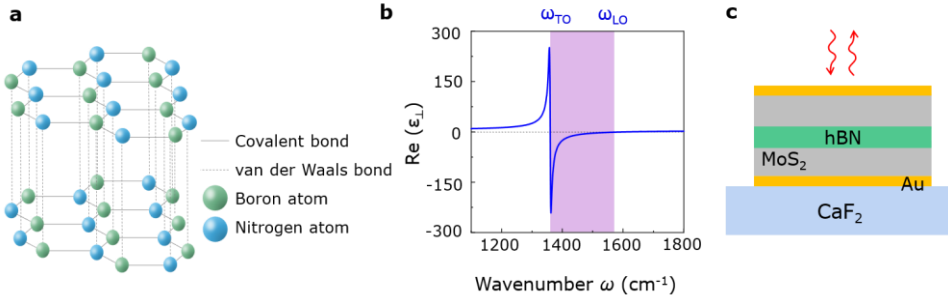


Figure 5.1: Cavity phonon polariton experiment. a) Sketch of two hBN layers, joined by van der Waals bonds; b) Real part of the in-plane dielectric function of hBN [91]. The purple area highlights the Reststrahlen band (RB) between the transverse optical (TO) and longitudinal optical (LO) phonon frequencies. c) Sketch of the experiment, illustrating spectroscopy of the infrared light reflected at a microcavity made of two gold mirrors embedding an hBN slab.

We illustrate the microcavities in Figure 5.1c. The schematic represents a thin hBN flake sandwiched between two MoS_2 layers, resulting in a $\text{MoS}_2/\text{hBN}/\text{MoS}_2$ dielectric stack, with the hBN flake located in the middle. Such heterostructures are fabricated following several steps of mechanical exfoliation on polydimethylsiloxane (PDMS) and deterministic transfer [210], as described in section 1.1 of this thesis. We use MoS_2 as a spacer, as it is spectrally flat in the mid-IR spectral region and can be easily obtained by exfoliation. An optical cavity is formed by placing the $\text{MoS}_2/\text{hBN}/\text{MoS}_2$ dielectric stack in between two gold layers of 20 nm thickness, fabricated by thermal evaporation. To place the hBN flake in the cavity center - where the maximum intensity of the electric field is expected to occur for odd cavity modes - we chose MoS_2 flakes of ideally the same thickness. For the present study, we fabricated cavities embedding hBN flakes of varying thickness L_{hBN} , as well as cavities fully filled

with hBN. Details of the fabrication process can be found in section 5.1. For each cavity, the total cavity length L_{cav} was adjusted such that the fundamental cavity resonance $\omega_{\text{cav}}^{(1)}$ coincides with the frequency of the in-plane transverse optical (TO) phonon of hBN, $\omega_{\text{TO}} = 1364 \text{ cm}^{-1}$ (169.1 meV) (Figure 5.1a) [187,202]. We determined L_{cav} by calculating the modes of a virtual cavity (in the following referred as to a *bare* cavity), for which we assume a frequency-independent hBN permittivity, $\epsilon(\omega) = \epsilon_{\text{hBN},\infty} = 4.52$ that neglects the phonon contribution (for details see Supplementary Information of [164]).

5.2. Fabrication of hBN filled microcavities tuned to the hBN TO phonon

We first discuss the design and fabrication of the microcavities. The simplest cavity to fabricate is the cavity embedding only one material. Since the first cavity mode needs to be tuned to the frequency of the TO phonon of hBN, $\omega_{\text{TO}} = 1364 \text{ cm}^{-1}$, we calculate the hBN thickness that fulfills this requirement. For cavities only filled with one material the frequencies at which the cavity modes appear are dependent of the length of the cavity, L_{cav} , and the refractive index of the material filling the cavity, n [166]. It can be calculated with equation (4), where m is the mode order, and ν_j the frequency of the j mode.

$$\nu_j = \frac{j}{2 \cdot n \cdot L_{\text{cav}}} \quad (4)$$

This equation works for cavities fully filled with a material. In the particular case of MoS₂/hBN/MoS₂ stacks embedding a very thin layer hBN, in which the hBN thickness can be neglected out of the total cavity length, we can consider the cavity completely filled with MoS₂. As the ratio between the thickness of hBN and the total cavity length, i.e., the filling factor, grows, we need to consider the refractive indexes of both the hBN, and of the material that we use as a spacer (MoS₂), to fix the hBN layer in the center of the cavity. For this

purpose, Transfer Matrix (TM) calculations were done by U. Muniain. We replace the permittivity of hBN for that of a *bare* material, of the same characteristics but without including the TO phonon in its description. In this manner, we obtain the frequency of the first cavity mode in a *bare* cavity, i.e., how the cavity would behave in the absence of the phonon. The experimental characterization of the optical properties of the materials is described in detail in section 5.6.1. With the estimation of the final thickness of the cavities, we prepared two different sets of cavities: some filled with thin layers of 10 and 100 nm of hBN, and others completely filled with hBN, of different thickness, to perform a detuning study.

Once the cavity thickness is obtained, we proceed with the fabrication following the calculated parameters. The samples need to be prepared on a substrate that is transparent in the infrared range of frequencies, as we want to characterize them both in transmission and reflectivity. Thus, we select CaF_2 as a suitable substrate for our experiments. We begin fabrication by preparing a thin film of gold on the substrate, that will act as the bottom mirror. Thermal evaporation of 15-20 nm of Au directly on the CaF_2 substrate, without the typical adhesion layer, yields a reflectivity of 98%, an adequate value for the fabrication of microcavities.

With the substrate ready, we can prepare the materials to be placed inside of the cavity by mechanical exfoliation using PDMS stamps and blue Nitto tape, as explained in Chapter 1. As stated before, we prepare two different types of microcavities: some embedding a thin layer of hBN, and some other fully filled with hBN. The fabrication process, although similar, has different steps for each case. Since we need the first cavity mode to match the frequency of the TO phonon of hBN, we have to adjust the length of the cavity accordingly. On the one hand, in the case of the fully filled cavity, we achieve this by selecting the thickness of the hBN slab. However, in the case of thin hBN layer, the thickness of hBN is kept constant while we adapt the thickness of the spacers. The particularities of these exfoliation processes are described in detail in the next sections. After the transfer of the flakes and the fabrication of the stacks of

materials of the required thicknesses, we again thermally evaporate 20 nm of Au, that form the top mirror, and close the cavity.

5.2.1. Fabrication of fully filled microcavities

To fabricate the fully filled microcavities, we first need to obtain thick flakes, or slabs, of hBN by mechanical exfoliation. We begin by placing a few crystals of hBN on a clean piece of blue Nitto tape. We peel off from the starting tape using new blue tape each time to break the crystals and obtain thinner flakes. Then, we transfer some material to PDMS stamps, following the steps described in Chapter 1. Using the optical microscope, we inspect the PDMS stamp for thick flakes. However, we need cavities between 1 to 2 μm thick. This thickness is too high compared to the thickness normally required during standard exfoliation of 2D materials. For hBN, we can optically identify the thickness of flakes up to 500 nm, approximately, as previously discussed in section 1.1.2. Thus, we need to transfer the flakes and determine their thickness using the profilometer. An example of a flake thickness measured at the profilometer is shown in Figure 5.2a. Once we have identified the flakes of the required thickness; we proceed to the evaporation of 20 nm of Au, that will form the top mirror and close the cavity.

The cavities are then ready for optical characterization at the FTIR. We measure fully filled cavities both in reflectivity (R , Figure 5.2b) and transmission (T , Figure 5.2c) mode. At frequencies well above that of the TO phonon of hBN, we get a series of dips and peaks that can be attributed to the cavity modes. At the TO phonon frequency, we get different features that will be analyzed and discussed in detail further in the text.

Additional information 5.1.: Some tips on the exfoliation of thick layers of 2D materials

- When working with 2D materials, sometimes finding a slab of material that is thicker than a few hundreds of nanometers is not

straightforward. Peeling off the blue tape just a couple of times is key to getting thick, not broken flakes or slabs.

- In case that we find two slabs so that the sum of both gives the required thickness, it is possible to stack them by picking up one of them and placing it on top of the other. The final stack will behave as if it was made from one piece of material.

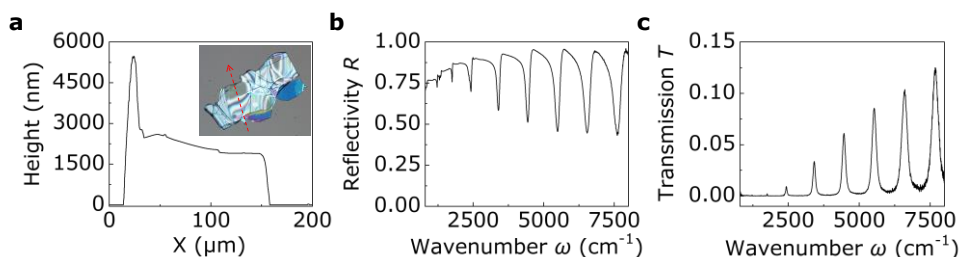


Figure 5.2: Fabrication and characterization of a microcavity fully filled with hBN, tuned to the first cavity mode. a) Profilometer measurement of the flake with the required dimensions, optical image of the flake is shown in the inset, in which the red dashed arrow indicates where the profile was measured. b) Reflectivity measurement taken at the FTIR over the area of the appropriate thickness, revealing the Fabry-Pérot behavior modes at higher frequencies, whereas at lower frequencies, new dips appear around the first cavity mode. c) Transmission spectra of the same area as shown in (b), exhibiting again Fabry-Pérot modes but giving much less signal.

5.2.2. Fabrication of microcavities embedding a thin layer of hBN

We now discuss the fabrication of microcavities embedding thin layers of hBN. In order to keep the hBN flake centered in the middle of the cavity, we need to use a material that acts as a spacer. The material of choosing has to provide flat surfaces of controllable thickness, so that we can transfer the hBN flake on top of it, and not have any vibration in the range of frequency of the TO phonon of hBN. Following these criteria, we select MoS₂, as it is a known 2D material, easy to exfoliate and spectrally flat in the IR range of

frequencies [211]. As it happens with thick hBN, when trying to obtain thick flakes of MoS₂, we lose the possibility of optically identifying the thickness of the flakes. Thus, once we optically identify some candidates that appear to be thick enough, we need to characterize them with the profilometer and identify one that fulfills the requirements. For this purpose, we need to transfer them to a low adhesion substrate, such as CaF₂ or glass, that allows a posterior pick-up of the flakes.

We measure the thickness of the MoS₂ flakes transferred to a substrate using the profilometer. Using TM calculations, we determine the total thickness of the cavity for each thickness of hBN. For instance, for an hBN thickness of 60 nm, we need a total thickness of 960 nm. Thus, ideally, we need to find two MoS₂ flakes of 450 nm. Once one is identified, we pick it up using a clean PDMS stamp, and transfer it to the gold mirror previously prepared on a CaF₂ substrate.

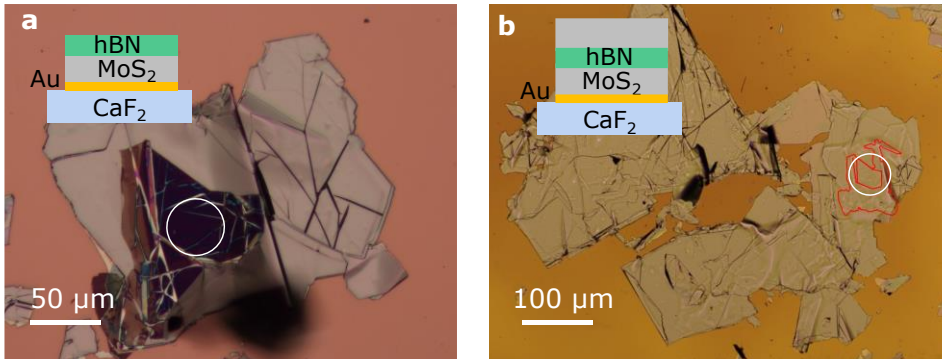


Figure 5.3: Fabrication of a microcavity embedding a 60 nm layer of hBN.

a) hBN-MoS₂ stack. White circle indicates the area where a 60 nm thick flake of hBN was placed on the area of the MoS₂ flake of approximately 450 nm of thickness, to build the first half of the cavity. Inset shows a schematic of the cross section of this area. b) Same stack as shown in (b), after the transfer of a second flake of MoS₂ of about 450 nm thick to complete the cavity. The flake shown in (a) is marked with a red line, white circle indicates hBN area as in (a).

Now we must prepare the first half of the cavity by placing the hBN layer on top of this flake. We exfoliate hBN using blue tape, as described in section

1.1. Since we need to find relatively thin hBN flakes, we can easily identify them by optical inspection of the PDMS stamp. When we find a suitable flake, we proceed to transfer it on top of the first half of the cavity (Figure 5.3a). We then characterize the thickness of the stack, to find the most suitable MoS₂ flake to place on top, but also to better determine the thickness of the hBN flake that we just transferred. Lastly, we transfer an MoS₂ flake of the proper thickness to form the final stack (Figure 5.3b) and measure the thickness again at the profilometer. After evaporation of the second Au mirror, as described in the previous section, the microcavities are ready for IR characterization.

Additional information 5.2.: Tips for the fabrication of MoS₂/hBN/MoS₂ heterostructures

- It is not essential to have the flake exactly in the center of the vertical heterostructure, since the maximum intensity of the electric field is broad and expands for about a third of the total length of the cavity, as is shown in Figure 5.6b. For instance, for the case described above it is enough to find a MoS₂ flake of thickness between 450 and 510 nm, and then adjust the thickness of the second flake accordingly, to achieve final length of the cavity as calculated.
- Transfer of hBN on MoS₂ is normally straightforward and does not require any special protocol. However, transferring the second flake of MoS₂ might be challenging, due to the thickness of the flake itself, and the fact that we need to transfer it on top of an already thick structure. To improve the chances of achieving the transfer without breaking the previously prepared stack, it is advisable to look for flakes large enough to cover the whole area, and even to touch the substrate around the stack. This is helpful, since the substrate offers a flat surface to attach to, whereas the second MoS₂ flake might present thicker areas that cause air bubbles and wrinkles on the second MoS₂ flake, that will make the transfer more difficult and increase the chances of ripping the hBN flake.

- Another useful aspect to consider is the topography of the flake that we want to transfer. If it has any areas that are flat and more homogeneous in thickness, the best option is to arrange the transfer so that this is the final part to be transferred, and that it touches with the substrate. Then, when the arm holding the slide is lifted, the flake will begin to detach from the PDMS from this side. Furthermore, since at that moment the flake would be already transferred partially to the substrate, it is more likely that it will stay on the stack even if it does not completely attach it, since the initial part will act as an anchor.

5.3. Infrared spectroscopy and analysis of hBN-filled microcavities

5.3.1. Experimental and numerical study of microcavities tuned to the TO phonon of hBN

To explore the coupling between the fundamental cavity mode and the hBN phonon, we performed a combined experimental and numerical study of cavities embedding 10 nm, 100 nm and 1665 nm thick hBN flakes (for sketches see insets in Figure 5.4b,f,j). We first verify that all three hBN flakes exhibit a sharp phonon line at $\omega_{\text{TO}} = 1364 \text{ cm}^{-1}$, by measuring reflection spectra of the stacks prior to the fabrication of the top mirror (Figure 5.4a,e,i). Additional to the phonon lines, we observe broader dips, which indicate that the stacks act as detuned open cavities of a low quality factor. By closing the cavities (i.e. fabricating the top gold mirror by thermal evaporation of 20 nm of Au), we clearly see a splitting of the reflection dip at the TO phonon frequency into two dips that are shifted to a lower and a higher frequency, $\omega_{-}^{(1)}$ and $\omega_{+}^{(1)}$, respectively (vertical blue dashed lines in Figure 5.4b,f,j). TM calculations match well the experimental reflection spectra (Figure 5.4,g,k) upon slight modification of the nominal values of the cavity parameters (see caption of

Figure 5.4). The need for such modification is attributed to uncertainties in the thickness and permittivity measurements. We find that the dip splitting $\omega_+^{(1)} - \omega_-^{(1)}$ significantly increases with increasing hBN thickness, in the experiment from 76 cm^{-1} to 215 cm^{-1} to 864 cm^{-1} (Figure 5.4b,f,j) and in the calculations from 68 cm^{-1} to 213 cm^{-1} to 860 cm^{-1} (Figure 5.4c,g,k). For comparison, we show in Figure 5.4d,h,l TM calculations of the *bare* cavity reflectivity, revealing that the uncoupled cavity modes indeed nearly perfectly coincide with the TO phonon frequency of the hBN layers, demonstrating that the double dip feature is a consequence of coupling between TO phonon and the respective fundamental cavity resonance. In the cavity that is fully filled with hBN (Figure 5.4j,k), the TO phonon also couples with higher-order cavity modes, which leads to the appearance of additional dips close to the TO phonon frequency (see discussion below).

We further corroborate the coupling between the TO phonon and the cavity modes by showing in Figure 5.4 the evolution of the reflectivity spectra as the cavity resonance is detuned from the TO phonon. For this purpose, we performed TM simulations of the reflectivity spectra as a function of total cavity length, L_{cav} , while keeping fixed the thickness of the hBN layer, $L_{\text{hBN}} = 10 \text{ nm}$ (Figure 5.4b, contour plot). We performed similar calculations for the *bare* cavity (Figure 5.4a, contour plot) and compare the results. One can observe that the first ($j = 1$) and third ($j = 3$) *bare* cavity modes ($\omega_{\text{cav}}^{(j)}$ in Figure 5.4a) split into an upper and a lower branch when the hBN layer is included ($\omega_-^{(j)}$ and $\omega_+^{(j)}$ in Figure 5.4b), as recognized by the reflection dips and their corresponding resonance frequencies (colored dashed lines in Figure 5.4a and b). Most important, the anti-crossing of the branches at the TO phonon frequency manifests the typical signature of coupling between two modes. The second cavity mode, in contrast, does not show any splitting of the reflection dips and thus reveals the absence of coupling, which can be explained by the vanishing electric field intensity of this mode in the cavity center (for further details see discussion below). The same analysis and analogue observations were made for the cavity embedding a 100 nm thick hBN layer.

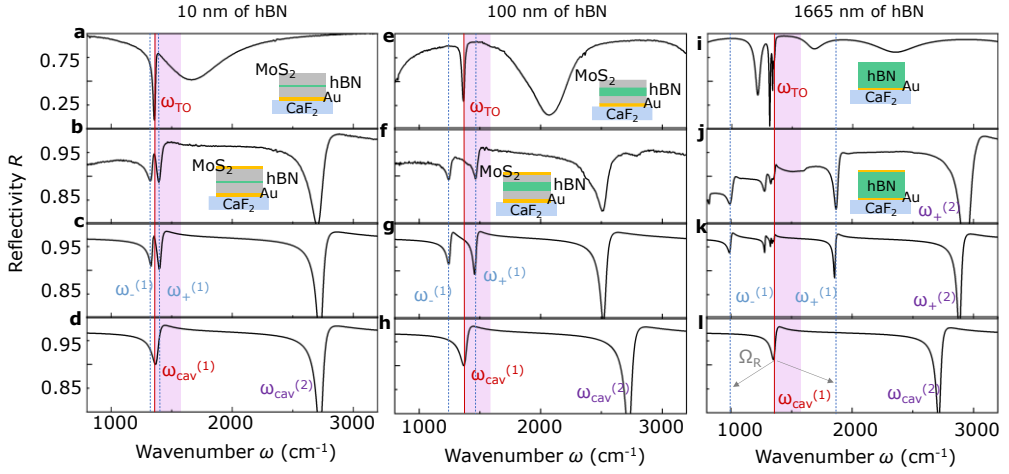


Figure 5.4: Experimental and calculated reflectivity spectra of hBN filled microcavities, in the range of frequencies close to the TO phonon. a) Experimental reflectivity spectrum of the MoS₂/hBN/MoS₂ heterostructure placed on the bottom gold mirror (illustrated by inset), measured before the evaporation of the top gold mirror. Measured thicknesses are 510 nm/10 nm/370 nm. ω_{TO} marks the frequency of the TO phonon of hBN. b) Experimental reflectivity spectrum of the stack of panel (a) after closing it with the top Au layer (illustrated by inset). $\omega_{-}^{(1)}$ and $\omega_{+}^{(1)}$ mark the dips emerging for the coupling between TO phonon and cavity mode. c) Simulated reflectivity spectrum of the cavity in panel (b), using layer thicknesses of 510 nm/10 nm/370 nm. d) Simulated reflection spectrum of the cavity of panel (c), in which hBN was replaced by a dielectric medium with $\epsilon(\omega) = \epsilon_{\text{hBN},\infty} = 4.52$. The labels $\omega_{\text{cav}}^{(1)}$ and $\omega_{\text{cav}}^{(2)}$ mark the first and second order cavity mode. e-h) Same as panels (a)-(d) for a MoS₂/hBN/MoS₂ heterostructure with measured thicknesses 520 nm/100 nm/430 nm and simulated thicknesses 480 nm/100 nm/390 nm. i-l) Same as panels (a)-(d) for a cavity fully filled with hBN, with measured and simulated hBN thickness 1665 nm. $\Omega_{\text{R}} = \omega_{+}^{(1)} - \omega_{-}^{(1)}$ in panel l marks the dip splitting. Purple shaded areas highlight the Reststrahlen band.

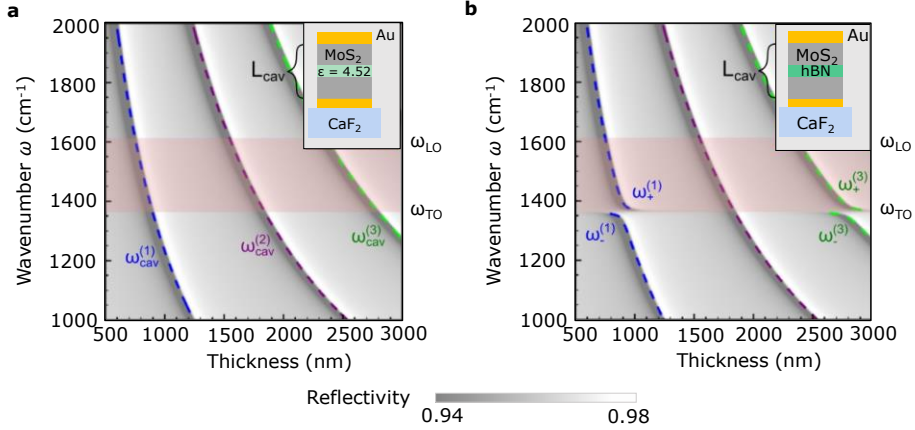


Figure 5.5: Strong coupling in a cavity filled with 10 nm of hBN. a) TM simulated reflectivity spectra of a *bare* cavity (illustrated by inset) as a function of cavity thickness L_{cav} . The dashed curves show the cavities' eigenmode frequencies $\omega_{\text{cav}}^{(i)}$ as function of L_{cav} . b) TM simulated reflectivity spectra of cavity filled with 10 nm of hBN (illustrated by inset) as a function of the total cavity thickness L_{cav} . The dashed curves show the cavities' eigenmode frequencies $\omega_{+}^{(i)}$ and $\omega_{-}^{(i)}$ as a function of L_{cav} . The reddish areas in (a) and (b) mark the Reststrahlen band of the hBN in-plane phonon.

5.3.2. Evolution of the coupling strength with the cavity filling factor

We observed in section 5.3.1 how the splitting between the polaritonic branches increases with the thickness of hBN placed in the cavity. This behavior is consistent with the scaling law of strong coupling, by which the coupling strength g depends on the amount of material interacting with the electrical field, i.e. the amount of dipolar excitations N that contributes to the coupled state, $g \sim \sqrt{N}$ [212–214].

For a quantitative analysis of the coupling between the hBN phonons and the microcavity photons in the TM calculations, we modelled the phonon-photon interaction by two coupled harmonic oscillators. One oscillator is associated with the electromagnetic field of the cavity (characterized by its resonance frequency $\omega_{\text{cav}}^{(i)}$ and decay rate $\kappa = 60\text{cm}^{-1}$) and the other one with

the hBN phonon (characterized by its resonance frequency ω_{TO} and decay rate $\gamma = 5 \text{ cm}^{-1}$). This model yields the eigenfrequencies $\omega_+^{(i)}$ and $\omega_-^{(i)}$ as a function of the known parameters $\omega_{\text{cav}}^{(i)}$, ω_{TO} , κ , γ and the unknown coupling strength g . Using $\omega_+^{(i)}$ and $\omega_-^{(i)}$ obtained from the TM calculations, we can apply the coupled harmonic oscillator model for determining g (see Appendix 5.6.3 for details).

We first studied the evolution of the coupling strength with the hBN layer thickness L_{hBN} . To that end, we calculated g as a function of the filling factor $f = L_{\text{hBN}}/L_{\text{cav}}$ for the first and second cavity mode (blue and red solid line in Figure 5.6a, respectively). We observe that g increases with the filling factor for both modes, more strongly for the first mode, which is a consequence of the intensity distribution of the electric field across the cavity (Figure 5.6b). The second cavity mode exhibits an intensity minimum in the center of the cavity, where the hBN layer is located. Thus, the coupling between hBN phonons and second cavity mode is generally much smaller than for the first cavity mode, that exhibits its intensity maximum in the cavity center. Note that this observation is consistent with the absence of a polariton gap for the second cavity mode in Figure 5.5b. The interaction between the TO phonon and the second cavity mode remains weak until the hBN layer is thick enough to sufficiently overlap with the cavities' off-center intensity maxima (shown in right panel of Figure 5.6b). A larger coupling strength can also be achieved for the second cavity mode by distributing the hBN layer near the positions where the intensity of this mode is maximum.

We can identify the weak and strong coupling regimes in Figure 5.6a according to the fulfilment of the conditions $\frac{g}{\kappa+\gamma} < \frac{1}{4}$ (blank area) and $\frac{g}{\kappa+\gamma} > \frac{1}{4}$ (beige area), respectively [165,168,215]. For the first cavity mode, remarkably, the strong coupling regime starts for $f = L_{\text{hBN}}/L_{\text{cav}} = 0.0025$, which corresponds to hBN slabs of about 3 nm thickness (about 4 atomic h-BN layers). Moreover, the usual condition for ultrastrong coupling, $\frac{g}{\omega_{\text{TO}}} > 0.1$ [207,216] (highlighted by the green area in Fig. 4), is fulfilled for hBN layers of thickness $L_{\text{hBN}} > 148 \text{ nm}$. Interestingly, we find that g saturates for the first order mode when $f > 0.8$ and

for the second-order mode when $f > 0.9$. The maximum coupling strength is obtained for both modes when the cavity is fully filled with hBN, with

$$g_{\max} = \sqrt{\frac{\omega_{\text{LO}}^2 - \omega_{\text{TO}}^2}{4}} = 428 \text{ cm}^{-1} \quad (5)$$

being exclusively determined by the materials' Reststrahlen band defined by the TO and LO phonon frequencies (for further discussion see below). In this case, the ratio $g_{\max}/\omega_{\text{TO}}$ reaches up to 0.31. These results show the versatility of the hBN-filled microcavities to explore the different light-matter coupling regimes, ranging from weak to ultrastrong coupling.

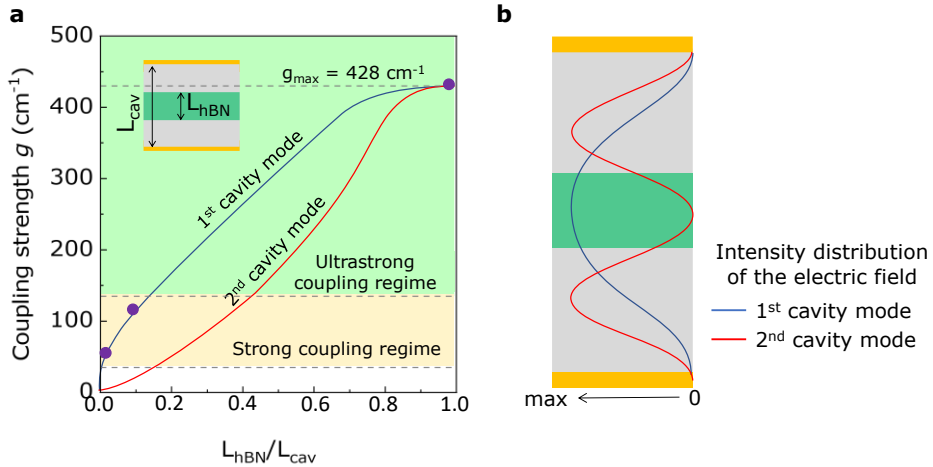


Figure 5.6: Evolution of the coupling strength as a function of the cavity filling factor. a) Coupling strength g between the TO phonon and the *bare* cavity modes, for a hBN layer of thickness L_{hBN} in the middle of a cavity of thickness L_{cav} , as sketched in the inset. The calculated evolution of g for varying L_{hBN} is shown for the first (blue solid line) and the second (red solid line) cavity modes. The coupling strengths corresponding to the strong coupling regime are highlighted by the beige area, and the green area corresponds to the ultrastrong coupling regime. Purple symbols indicate the experimental coupling strength g_{exp} obtained from Figure 5.4. b) Sketch of the intensity distribution of the electric field of the first and second cavity modes.

To identify the coupling regime for the experimental spectra shown in Figure 5.4, we determine the coupling strength according to $g_{\text{exp}} = (\omega_{+}^{(1)} - \omega_{-}^{(1)})/2$,

where $\omega_+^{(1)} - \omega_-^{(1)}$ is the experimental dip splitting. This approach [215,217] is valid because (i) the coupling strength g is large and (ii) the cavity and phonon resonances match well, i.e. $\omega_{\text{cav}}^{(1)} \approx \omega_{\text{TO}}$ (see appendix 5.6.3). Plotting g_{exp} in Figure 5.6a (purple dots), good agreement with the theoretical values (blue solid line) is found, verifying that strong coupling between microcavity photons and phonons can be indeed achieved experimentally with layers of a polar material as thin as 10 nm.

5.3.3. Ultrastrong coupling in fully filled cavities.

To further illustrate and explore the regime of maximum coupling strength, we performed a systematic experimental and theoretical study of cavities fully filled with hBN (Figure 5.7). Analogously to Figure 5.5, we calculated reflection spectra (contour plots) and eigenmode (i.e. resonance) frequencies (dashed lines) as a function of the cavity (i.e. hBN) thickness $L_{\text{hBN}} = L_{\text{cav}}$. By comparison with the spectra and eigenmodes of the corresponding *bare* cavities (Figure 5.7a), we clearly recognize the anti-crossing between the hBN phonon (ω_{TO}) and all cavity modes [218] ($\omega_{\text{cav}}^{(j)}$ with $j = 1, 2, 3, \dots$), yielding the polaritonic eigenmodes $\omega_+^{(j)}$ and $\omega_-^{(j)}$ (contrary to Figure 5.5, where coupling is observed only for odd j). Further, a much larger spectral separation of the upper and lower polariton branches occurs as compared to Figure 5.5b ($L_{\text{hBN}} = 10$ nm), yielding a polaritonic gap spanning the whole Reststrahlen band (reddish area in Figure 5.7a,b). We determine a Rabi splitting Ω_{R} of $\Omega_{\text{R}} \approx 2g = 856 \text{ cm}^{-1}$, which lies well inside the ultrastrong coupling regime ($g/\omega_{\text{TO}} = 0.31$), and which is larger than the Reststrahlen band (246 cm^{-1}). We experimentally confirm the calculations by measuring reflectivity spectra of differently thick cavities that are fully filled with hBN (Figure 5.7c). The spectral positions of the reflectivity dips are plotted in Figure 5.7b (red symbols), showing an excellent agreement with the calculated spectra and cavity eigenmodes. We note that the experimental reflectivity spectra exhibit a set of thickness-independent dips at around 819 cm^{-1} (green dots in Figure 5.7b), which stems from the out-of-plane phonon of hBN [195]. This phonon appears in the experimental spectra due to the focused

illumination of the cavity using a Cassegrainian objective, yielding electric field components perpendicular to the hBN layer. Therefore, these field components can couple with the out-of-plane hBN phonon, as opposed to the case of normal incidence, in which the electric field can only couple with the in-plane phonon. Further details can be found in the Supplementary Information of [164].

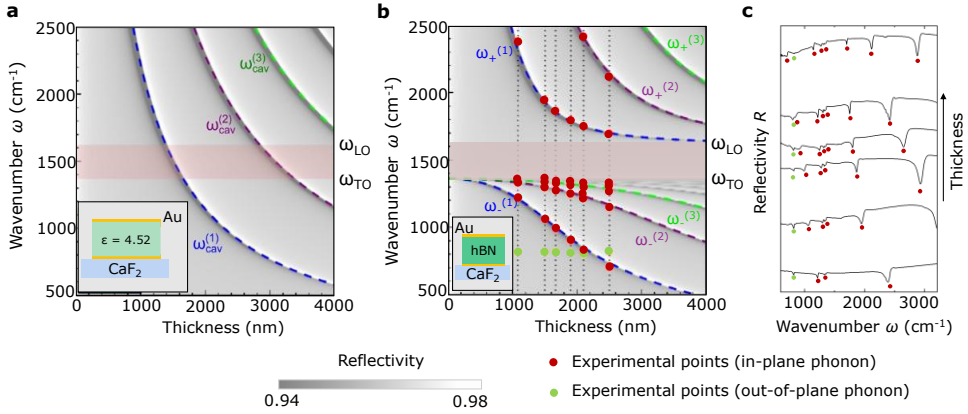


Figure 5.7: Ultrastrong coupling in microcavities fully filled with hBN. a) Reflectivity spectra of a bare cavity (illustrated by inset) as a function of cavity thickness L_{cav} . The dashed curves show the cavities' eigenmode frequencies $\omega_{\text{cav}}^{(j)}$ as a function of L_{cav} . b) Reflectivity spectra of a cavity fully filled with hBN (illustrated by inset) as a function of cavity thickness L_{cav} . The dashed curves show the cavities' eigenmode frequencies $\omega_{+}^{(j)}$ and $\omega_{-}^{(j)}$ as a function of L_{cav} . Red and yellow symbols show the spectral position of the experimental reflectivity dips extracted from panel (c). The reddish areas in (a) and (b) mark the Reststrahlen band of the in-plane phonon of hBN. c) Experimental reflectivity spectra of cavities fully filled with hBN (vertically offsetted). Cavity thicknesses (from bottom to top) are: 1080 nm, 1500 nm, 1665 nm, 1900 nm, 2100 nm, 2500 nm.

5.4. Comparison of polariton dispersion

To analyze and discuss the dispersion of the microcavity phonon polaritons, $\omega(k)$, we extracted the wavevector k from the reflectivity spectra according to

$$k = \frac{j\pi}{L_{cav}} \quad (6)$$

assuming perfect metal mirrors and where L_{cav} is the cavity length at which the eigenmode of order j and frequency ω is found (see Appendix 5.6.4). In Figure 5.8a,b we compare $\omega(k)$ for the cavity that is fully filled with hBN (obtained from Figure 5.7) and the cavity embedding a 10 nm thick hBN layer (obtained from Figure 5.5), respectively (calculations are shown by black curves and experimental values by black symbols). Note that for the fully filled cavity, all modes j were considered, whereas for the cavity filled with 10 nm of hBN we considered only the first mode ($j = 1$). Both dispersions feature anti-crossing, separating into a lower and an upper microcavity phonon polariton branch, with large Rabi splitting amounting to $\Omega_R \approx 856 \text{ cm}^{-1}$ and $\Omega_R \approx 67 \text{ cm}^{-1}$, respectively.

To appreciate the dramatic coupling strengths between infrared microcavity modes and phonons with respect to typical molecular vibrations [209], we show in Figure 5.8c,d the calculated polariton dispersions obtained (analogous to Figure 5.5 and Figure 5.7) for cavities embedding molecules that possess C=O vibrations. Specifically, we consider the ensemble of C=O oscillators of PMMA, whose electromagnetic response is described by the dielectric function provided in the Supplementary Information of [164]. Clear anti-crossing can be observed for the cavity fully filled with PMMA (Figure 5.8c), but the Rabi splitting $\Omega_R \approx 159 \text{ cm}^{-1}$ is more than 5 times smaller than that of the cavity fully filled with hBN. For the cavity filled with a 10 nm thick PMMA layer we do not find anti-crossing (Figure 5.8d), revealing that the system is in the weak coupling regime, in contrast to the strong coupling regime achieved with a 10 nm thick hBN layer (Figure 5.8b). We note that the C=O vibrations are rather strong and that many molecular vibrations can be much weaker. To demonstrate the coupling between microcavity modes and weaker molecular oscillators by way of an example, we reduced the oscillator strength in the permittivity model of C=O by a factor of 100 and recalculated the dispersions. In both the partially and fully filled cavity we do not observe anti-crossing (Figure 5.8e,f), highlighting that for weak molecular oscillator strong coupling cannot be achieved by placing them into a microcavity.

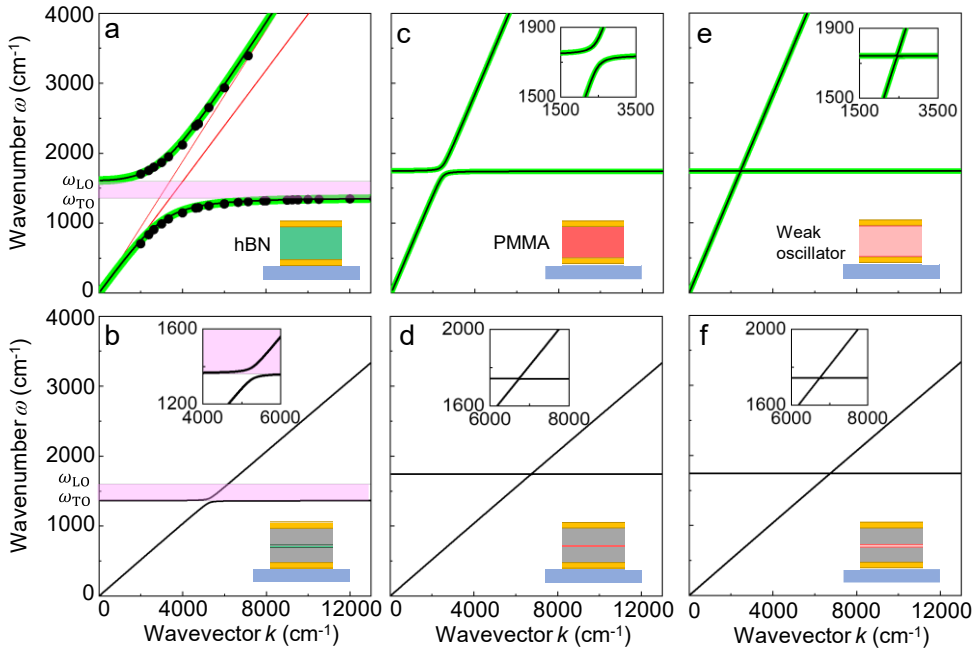


Figure 5.8: Polariton dispersions. a) Measured (black symbols) and calculated (black curves) phonon polariton dispersion obtained from hBN layers that fully fill the cavity. Green curves show the bulk phonon polariton dispersion of hBN. Red dashed lines indicate the light cones $\omega(k) = \frac{kc}{\sqrt{\varepsilon(\omega=0)}}$ and $\omega(k) = \frac{kc}{\sqrt{\varepsilon_{hBN,\infty}}}$, where $\varepsilon(\omega=0) = 6.29$ and $\varepsilon_{hBN,\infty} = 4.52$ are the low- and high-frequency permittivities. The Reststrahlen band of bulk hBN is marked by the purple area. b) Calculated (black curves) phonon polariton dispersion obtained from cavities that are filled with a 10 nm thick hBN layer. c) Calculated (black curves) polariton dispersion obtained for cavities that are fully filled with molecules exhibiting a C=O vibration. Green curves show the bulk polariton dispersion of the filling material. d) Dispersions for a 10 nm thick molecular layer embedded in the cavity. e) Calculated (black curves) polariton dispersion obtained for cavities fully filled with hypothetical molecules exhibiting a vibration of arbitrarily reduced oscillator strength. Green curves show the bulk polariton dispersion of the filling material. f) Dispersions for a 10 nm thick hypothetical molecular layer of arbitrarily reduced coupling

We finally compare the dispersions of the material in the fully filled cavities with the bulk polariton dispersion of the same material, $\omega(k) = ck\sqrt{\varepsilon_m}$, where c is the speed of light and ε_m the dielectric function of the filling material (green solid lines in Figure 5.8a,c and e). Interestingly, we find that the polariton

dispersion obtained from fully filled cavities is identical to that of the bulk polariton dispersion of the filling material [219], independent of whether phonon or molecule oscillators (weak or strong) are embedded into the cavity. The maximum splitting is determined exclusively by the material properties as clearly shown by the analytical expression of g in the Supplementary Information of [164] and is also highlighted in ref. [220]. These results show that the maximum coupling strength between a cavity mode and a dipolar excitation is governed by that of photons and bulk, implying that fully filling a resonant cavity with a specific material does not enhance the coupling strength between light and matter. The cavity merely enforces the strongly coupled state by selecting the corresponding wavevector. Importantly, strong coupling can be only achieved in case the bulk polariton dispersion of the cavity's filling material exhibits strong coupling, i.e., anti-crossing. In case the dispersion of light in bulk does not exhibit strong coupling (i.e., no polaritonic behavior), the coupling of this bulk material with a cavity mode will remain weak, that is, the cavity does not leverage the coupling strength beyond the one that can be achieved with bulk. Interestingly, it has been reported that vibrational strong coupling in cavities can modify physical and chemical properties of the cavity filling [116,117,221,222], although the coupling strength is not enhanced. An effect other than the coupling strength - such as a modification of the density of states - may be needed to explain this intriguing phenomenon.

5.5. Conclusions

In conclusion, we demonstrated that classical microcavities can be applied for studying and tuning the coupling between photons and optical phonons in thin layers of polar vdW materials, which can be obtained in high crystal quality by exfoliation. For the studied vdW material hBN, our theoretical analysis predicts strong coupling for hBN layers between 3 and 148 nm thickness, and ultrastrong coupling for hBN thicknesses larger than 148 nm. Analysis of experimental reflection spectra of cavities embedding 10 and 100 nm-thick hBN layers confirms strong coupling. For fully filled cavities ultrastrong was

demonstrated experimentally. In comparison with typical molecular vibrational strong coupling in fully filled cavities, the coupling strength is about five times larger due to the high oscillator strength of crystal phonons. Our experiments can be readily adapted to study phonon polaritons in other vdW materials [223], including doped semiconductors and heterostructures exhibiting multiple phonons or plasmon-phonon coupling. Further, by using vdW materials with even larger oscillator strength than hBN, the deep strong coupling regime [224–226] may be reached. We also note that recent experimental reports have demonstrated the possibility of tuning optical phonon frequencies by various methods, such as photoinjection [227], heterostructuring [228] and intercalation [229], which could allow for manipulating the phonon polariton spectrum, similarly to intersubband polaritonic systems [230]. Considering the intriguing vibrational strong-coupling phenomena that have been reported in literature it may be interesting to study how ultrastrong coupling of phonons may affect physical and chemical properties of crystals that are embedded into cavities. Only recently it has been predicted that strong coupling in quantum paraelectrics can trigger the ferroelectric phase [231].

5.6. Appendices

5.6.1. Fourier Transform Infrared Spectroscopy

The microcavities are characterized using FTIR spectroscopy. FTIR is based on the interaction of IR light and materials. When the IR beam goes through the sample, the material will selectively absorb, transmit or reflect certain wavelengths, depending on the type of vibration and the atoms forming the bonds in the material. The light passing through the sample, or being reflected by it, is collected and analyzed by interferometry against a reference beam. The resulting spectrum has the features that characterize the material in the sample. The light path and basic elements of a FTIR systems are illustrated in Figure 5.9a.

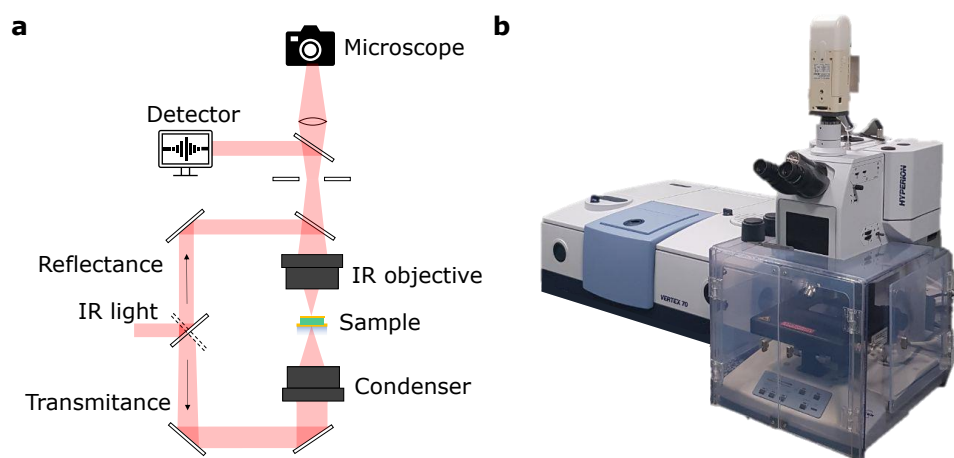


Figure 5.9: Fourier Transform Infrared Spectrometer (FTIR). a) Schematics of the basic operation of the FTIR, indicating the optical paths for reflectivity and transmission, and the positions of the sample, detector, and microscope. b) Bruker Hyperion 2000 microscope coupled to Bruker Vertex 70 FTIR spectrometer, used for the measurements presented in this chapter.

To characterize 2D materials, we couple the spectrometer to an optical microscope. The microscope has an aperture that allows selection over the area of the sample to be analyzed. However, it is important to keep this aperture

with approximately 40 μm minimum lateral size, to avoid inducing artifact in the spectra due to the diffraction limit. The measurements of the cavities describe in this chapter were performed in a Bruker Hyperion 2000 FTIR spectrometer, with 15x IR Cassegrainian objective with numerical aperture $\text{NA} = 0.4$ (Figure 5.9b). Its detector can measure the range of frequencies from 800 to 4000 cm^{-1} , in reflectivity and transmission modes. Before starting the measure, we need to calibrate the background so that we can extract the sample spectra without any background contributions. For the reflectivity measurements, we use a gold substrate to characterize the 100% reflectivity. For transmission, we want to discard the contribution of the substrate. Therefore, we take the background measurement as the signal going through a clean CaF_2 substrate.

5.6.2. Characterization of the optical parameters of the materials used in the microcavities

For the transfer matrix calculations, we consider the relative permittivity of the substrate $\epsilon_{\text{CaF}_2} = 1.882$. For the design of the microcavities, we first need to optically characterize the materials that we will use for its fabrication. First and foremost, we need to obtain the frequency of the TO phonon of hBN, since it determines the frequency to which we tune the first cavity mode. We prepared a hBN flake on CaF_2 substrate (Figure 5.10a) and performed reflectivity measurement at the FTIR. The resulting spectra is shown in Figure 5.10b. We measure a TO frequency $\omega_{\text{TO}} = 1364 \text{ cm}^{-1}$ similar to the frequency of 1360 cm^{-1} reported in [91], from which we take the rest of the parameters.

The permittivity of MoS_2 is obtained by the analysis of a series of cavities fully filled with MoS_2 . We transferred an MoS_2 with areas of different thickness to a CaF_2 substrate and evaporated 20 nm of Au on top (Figure 5.11.a). Reflectivity measurements of this flake give the position of the cavity modes (Figure 5.11.b). Then, by transfer matrix calculations, we obtain the permittivity ϵ_{MoS_2} that reproduce the frequency of these modes, obtaining one

value for each of them. The permittivity of MoS₂ as a function of the frequency is obtained by a linear fitting of these values, $\epsilon_{\text{MoS}_2}(\omega) = 14.689 + 0.00151\omega [\text{cm}^{-1}]$. Its refractive index is $n_{\text{MoS}_2} = 3.7$.

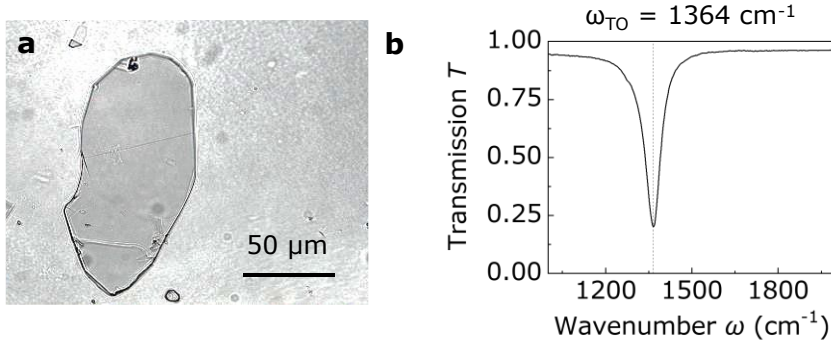


Figure 5.10: Optical characterization of the TO phonon of hBN. a) Optical image of an hBN flake transferred to a CaF₂ substrate. b) Transmission spectrum of the flake shown in (a)

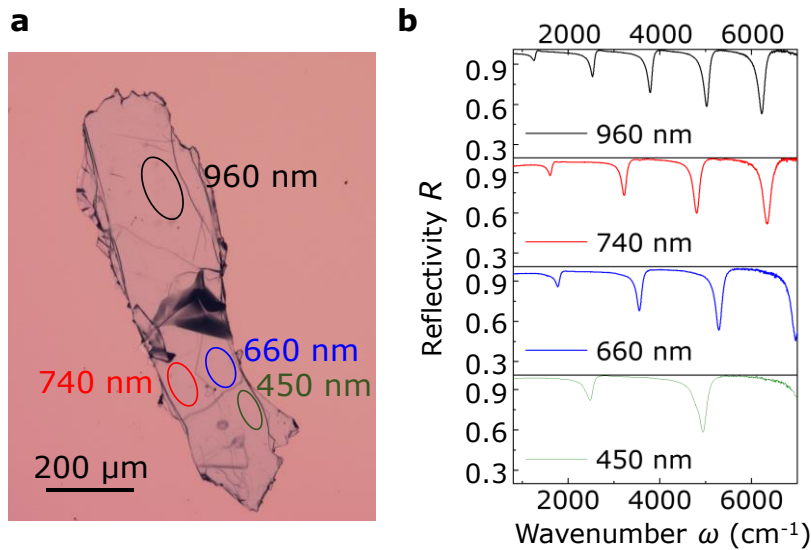


Figure 5.11: MoS₂ microcavities on a single flake to characterize the permittivity of MoS₂. a) Optical image of the single MoS₂ flakes in which areas of different thicknesses are identified and marked with circles of different colors and the corresponding labels. b) Reflectivity spectra measured at the FTIR for each of the areas marked in (a).

Finally, we measure at the FTIR the gold layer of 20 nm on the CaF₂ substrate. It has a flat reflectivity of 98% in the whole range of frequencies. For the transfer matrix calculations, the gold mirrors are described by a Drude permittivity, fitting to the data in [232].

5.6.3. Determination of the coupling strength g in TM simulations

To determine the coupling strength g in the TM simulations, we modelled the phonon-photon interaction by the coupling of two classical harmonic oscillators, where one of the oscillators is associated with the electromagnetic field of the cavity and the other one with the hBN phonon. For small g (corresponding to the weak and strong coupling regimes), the eigenfrequencies of the polaritonic modes, which correspond to the eigenvalues of the harmonic oscillator model, are given by

$$\omega_{\pm}^{(j)} = \frac{1}{2}(\omega_{\text{cav}}^{(j)} + \omega_{\text{TO}}) \pm \frac{1}{2} \text{Re} \left[\sqrt{\left(\omega_{\text{cav}}^{(j)} - \omega_{\text{TO}} + i \frac{\gamma - \kappa}{2}\right)^2 + 4g^2} \right] \quad (7)$$

where κ and γ are the cavity and phonon decay rates, respectively. For large g (corresponding to the ultrastrong coupling regime), we can neglect the losses κ and γ and obtain the following expression from the equations of the coupled harmonic oscillators:

$$\omega_{\pm}^{(j)} = \frac{1}{\sqrt{2}} \sqrt{\left(\omega_{\text{cav}}^{(j)}\right)^2 + \omega_{\text{TO}}^2 + 4g^2} \pm \sqrt{\left(\left(\omega_{\text{cav}}^{(j)}\right)^2 + \omega_{\text{TO}}^2 + 4g^2\right)^2 - 4\left(\omega_{\text{cav}}^{(j)}\right)^2 \omega_{\text{TO}}^2} \quad (8)$$

The eigenfrequencies given by equation (8) coincide with the results obtained from the Hopfield Hamiltonian, indicating that a classical model of harmonic oscillators can describe the ultrastrong coupling regime [196]. For intermediate values of g , equations (7) and (8) give very similar results.

In order to determine g for a fixed hBN layer thickness L_{hBN} , we choose the total thickness L_{cav} for which the cavity mode is tuned to the TO phonon (i.e. $\omega_{\text{cav}}^{(j)} = \omega_{\text{TO}} = 1364 \text{ cm}^{-1}$). Then, we determine for this cavity the eigenfrequencies of the modes ($\omega_+^{(j)}$ and $\omega_-^{(j)}$ for the filled cavity, and $\omega_{\text{cav}}^{(j)}$ for the bare cavity) from the poles of the reflection coefficient of the system, as obtained from the TM simulations [231] (for details see Supplementary Information of [164]). We note that the spectral position of reflection minima and the actual polaritonic modes of a system can be different due to the interference of spectrally closely spaced modes (particularly in weakly coupled systems [168,215]). The coupling strength is finally obtained by solving equations (7) and (8) for g (depending on whether the system is in the strong or in the ultrastrong coupling regime). Note that the value of g varies slightly depending on whether we solve the equations for ω , $\omega_+^{(j)}$ or $\omega_-^{(j)}$. We thus determine g by minimizing the combined error.

From the TM simulations considering the 10 nm hBN layer (Fig. 3a) we obtained $\omega_+^{(1)} = 1395 \text{ cm}^{-1}$, $\omega_-^{(1)} = 1332 \text{ cm}^{-1}$, $\kappa = 60 \text{ cm}^{-1}$ and $\gamma = 5 \text{ cm}^{-1}$, yielding subsequently $g = 34 \text{ cm}^{-1}$ via the harmonic oscillator model. For the 100 nm hBN layer (for details see Supplementary Information of [164]). we obtained $\omega_+^{(1)} = 1471 \text{ cm}^{-1}$, $\omega_-^{(1)} = 1260 \text{ cm}^{-1}$, $\kappa = 60 \text{ cm}^{-1}$, $\gamma = 5 \text{ cm}^{-1}$, and subsequently $g = 106 \text{ cm}^{-1}$. For the fully-filled cavity (Fig. 5a) we obtained $\omega_+^{(1)} = 1857 \text{ cm}^{-1}$, $\omega_-^{(1)} = 1002 \text{ cm}^{-1}$, $\kappa = 30 \text{ cm}^{-1}$, $\gamma = 5 \text{ cm}^{-1}$, and subsequently $g = 428 \text{ cm}^{-1}$. We note that the values for $\omega_+^{(1)}$ and $\omega_-^{(1)}$ obtained for these three cavities are very close to the frequencies of the calculated reflectivity dips. For example, for the cavity containing the 10 nm hBN layer, the reflection dips occur at $\omega_+^{(1)} = 1392 \text{ cm}^{-1}$ and $\omega_-^{(1)} = 1322 \text{ cm}^{-1}$. We conclude that the dips in the experimental reflection spectra reveal the polaritonic eigenmodes and thus can be directly used to determine the experimental coupling strengths.

5.6.4. Comparison between phonon polariton dispersions

The polaritonic modes in bulk hBN are associated with propagating waves characterized by a wavevector k and an angular frequency ω that are connected

according to the dispersion relation $\omega(k)$. On the other hand, the modes of the cavity for normal incidence are standing waves with selected discrete wavelengths λ_{cav} , which depend on the cavity length L_{cav} , according to $\lambda_{\text{cav}} = \frac{2L_{\text{cav}}}{j}$ (j is the order of the mode). For the fully-filled cavity, λ_{cav} would also correspond to the wavelength of the phonon polariton in bulk. Thus, for a given resonant frequency ω , we recover the corresponding wavevector k of the bulk dispersion relation $\omega(k)$ by applying

$$k = \frac{2\pi}{\lambda_{\text{cav}}} = \frac{j\pi}{L_{\text{cav}}} \quad (9)$$

6. Summary and final conclusions

This thesis presents a comprehensive guide on the nanofabrication of different types of samples, by using the techniques and tools available at CIC nanoGUNE. We described in detail the optimization process for the successful fabrication of samples for different studies and projects.

In the first part, we introduce some generalities about the techniques, focusing on those aspects that may play an important role during the fabrication of samples. First, we introduce the basics for exfoliation of 2D materials. By successive peeling of the materials using blue tape, we obtain thin flakes and even monolayers of 2D materials from original, bulk crystals. To identify and characterize the thickness of these layers, we can use optical contrast, AFM measurements. Additionally, Raman spectroscopy can be used to identify monolayers and bilayers of some materials, like graphene and MoS₂. To transfer the flakes to substrates, and to fabricate van der Waals heterostructures, we use different strategies and platforms.

Firstly, viscoelastic stamps of polydimethylsiloxane (PDMS) are useful for transferring flakes from the blue tape to a final substrate. Furthermore, being translucent they are a good platform for optical inspection of thin layers, providing color contrast for a range of thicknesses of different materials. Some characterization techniques, such as Raman spectroscopy, can be performed on the flakes directly on the PDMS stamp before the transfer to the substrate. However, AFM or profilometry measurements cannot be performed on their surface, due to their viscoelastic properties. On the other hand, PDMS stamps can also be used for fabrication of heterostructures by successively transferring flakes on top of each other, although some contamination may be left in the interface between each layer.

Secondly, membrane-based strategies, such as the transfer using a PC membrane, are useful for picking up flakes and forming heterostructures with clean interface. However, they usually require high temperatures and solvents, which may damage the flake. The cleaning of the membrane using a solvent also leads to the accumulation of residues on the upper surface of the heterostructure.

In Chapter 2, we review the general fabrication techniques that were explored for the fabrication of the samples. In particular, Direct Laser Writer (DLW) is a type of optical lithography that directs a laser beam to pattern a resist sensitive to the wavelength of the laser (405 nm), obtaining minimum resolutions of approximately 500 nm. On the other hand, using Electron Beam Lithography (EBL) to pattern electron sensitive resist, we are able to obtain minimum features of 20 nm. Adjusting the exposure parameters (acceleration voltage, dose factor, step size), selecting an appropriate resist and correcting the proximity effect are key aspects to the successful fabrication of any sample.

After lithography, using reactive ion etching or ion milling, we are able to remove material to structure substrates or flakes in the desired shape. Cr-Al hard masks can be used to protect the surfaces from etching and preserve the surface properties of the materials. On the contrary, we deposit material on the samples by evaporation or sputtering. During the lift-off step, we remove the excess material that is deposited over the resist layer and obtain the final structures.

All these protocols and details are put into context in Chapter 3. In this section we present a series of samples fabricated as collaborative work within the framework of different projects. We describe four different fabrication processes.

First, we describe the fabrication of micrometric arrays of nanoribbons on Si/SiO₂ substrates using EBL. The minimum dimensions that were achieved are ribbons of 80 nm of width, separated by 45 nm, consistently over 20 μm. We conclude that no proximity effect corrections are required despite the density of the arrays, but that the actual measured widths of the ribbons double the nominal widths on the design.

Si/SiO₂ substrates are a standard platform for the preparation of samples for electronic or spectroscopic measurements. However, for transmission electron microscopy (TEM), we need to have transparent substrates that allow the passage of electrons. The standard substrates in this case are nanometrically thin membranes. In order to prepare non-concentric disk-ring nanocavities for Electron Energy Loss Spectroscopy (EELS) we patterned these membranes using EBL. We observed the influence of the writing mode in the EBL for the case of substrates with few backscattered electrons and determined that the best writing mode for round shape, as disks and rings, on the thin membranes, is the concentric writing of rings. Furthermore, the absence of backscattered electrons translates into lower effective dose, thus the actual dose

required for writing the structures doubles the nominal area dose of the resist.

When preparing thin TEM membranes for the lithography, it is important to use low acceleration speeds and long spin coating time to get homogeneous films. Baking the resist to remove the solvents needs to be done in a controlled atmosphere and ramping the temperature, to avoid the breaking of the membranes due to thermal shocks. After the lithography, evaporation of materials was done by fixing the membranes to a substrate and without rotation, to avoid shadowing effects. Finally, lift-off was done by immersing the samples in the removing solution and leaving the membranes overnight to ensure the soaking in acetone and gentle removal of the resist, without using a heavy flow of acetone. For these samples, the thinnest widths of the rings achieved were 20 nm, with separation of approximately 30 nm between the disk and the ring. These dimensions are close to the nominal resolution limits of the techniques, and the minimum that can be obtained using these substrates and materials.

On the opposite side, patterning insulating substrates using EBL can induce charge accumulation that distorts the final dimensions of the structures. To avoid this effect, we need to cover the resist with a conductive layer, that can be either a thin layer of gold deposited on the resist or a second spin coated layer of a conductive resist. A consequent adjustment of the exposure to lower area doses is also required for the correct definition of the structures. These factors were considered for the fabrication of nano resonators on CaF_2 substrates by electron beam lithography. Furthermore, we combined the use of cold developer and O_2 plasma, as well as the degassing of the substrate precious to the metal evaporation, to achieve the successful lift-off of micrometric arrays consisting on 30×50 nm nanoresonators separated between each other by

gaps below 30 nm. These steps are key to obtain nanometric features on insulating substrates, and to enhance the adhesion of the nano resonators on the surface of CaF_2 . We tuned the optical absorption of the arrays by slightly varying the dimensions and spacing of the nanoresonators and confirmed the shift of the absorption line from 600 to 670 nm using a visible spectrophotometer coupled to a microscope.

In the last project that is described in the chapter, we combine the lithography described above to pattern and electrically contact a single THz resonator on a graphene/hBN heterostructure, on the standard Si/SiO₂ substrate. We designed the fabrication process as a protocol based on three distinct steps: First, we fabricated the graphene/hBN heterostructure using the PC membrane technique, by pick-up and transfer of large graphene and hBN flakes (over 30 μm lateral size) directly exfoliated on Si/SiO₂ substrates. Then, we design the electrodes using EBL, and electrically contacted the heterostructure by selectively removing the hBN using reactive ion etching, and evaporating Ti/Au. We characterized the charge neutrality point of the graphene below the hBN flake. Finally, we fabricated the resonator aligned on the contacted heterostructure, and divided into two separate regions by a 500 nm gap over 1 mm to each side of the resonator. These dimensions are close to the resolution limit of the DLW, and almost too big to be patterned at the EBL, a tool focused on nanometric features, thus the challenge of this project. On the one hand, we spin coated the sample with three layers of PMMA, instead of the standard DL PMMA, to achieve a higher resist thickness, needed for the posterior lift-off step of the 150 nm of Au required for the fabrication of the THz resonator. After some optimization tests, we reduced the developing time and increased the nominal size of the gap between the two parts of the resonator to obtain a vertical cut of 500 nm along the near 2 mm of the disk surrounding the

resonator, and the working samples were left to be characterized at the THz set-up.

In conclusion, we believe that all the fabrication and studies developed and described in the thesis provide insight into the preparation of protocols for nanofabrication and offer a toolbox for the fabrication of a wide variety of samples on both standard and unconventional substrates. Furthermore, after this compilation of samples and fabrication processes, we include two complete works that were developed during this thesis, from the design and preparation of the samples to the characterization, measurements, and analysis of the results. In Chapter 4, we present a study of the effect of biaxial strain on hybrid organic-inorganic metal-halide layered perovskites (HOIPs), by transferring some flakes on SiO₂ rings. We observed that a strain below 1% is able to induce changes in the photoluminescence and Raman spectra by distorting the octahedra layer in the perovskite. The study highlights the importance of material design and the choice of strain-inducing platforms for device-compatible substrates. It also emphasizes the significance of combining simulations and spectroscopic techniques to understand and develop new applications for strain-based optoelectronics and sensing using 2D HOIPs.

Moreover, the evolution from the weak to the ultrastrong coupling regime in classical microcavities embedding hBN layers of different thicknesses is presented in Chapter 5. In summary, this study demonstrated that classical microcavities can be used to study and control the coupling between photons and optical phonons in thin layers of polar van der Waals materials, specifically hexagonal boron nitride (hBN). The theoretical analysis predicted strong coupling for hBN layers between 3 and 148 nm thickness, and ultrastrong coupling for thicknesses larger than 148 nm. Experimental reflection spectra confirmed strong coupling for cavities embedding 10 nm and 100 nm thick hBN layers, and

ultrastrong coupling for fully filled cavities. The coupling strength in hBN was found to be about five times larger than typical molecular vibrational strong coupling due to the high oscillator strength of crystal phonons. This approach can be extended to study phonon polaritons in other van der Waals materials, including doped semiconductors and heterostructures. Furthermore, exploring ultrastrong coupling of phonons in crystals embedded in cavities could provide insights into the effects on their physical and chemical properties.

List of recipes

Table 1.1: Spin coating parameters for the preparation of PVA/PMMA substrates.....	29
Table 2.2: Evolution of thickness with spin coating speed of a) PMMA495K in anisole; b) PPMA950K in anisole.	49
Table 2.3: Recipe for spin coating a double layer of PMMA.....	49
Table 2.4: Recipe for the deposition of Au conductive layer for EBL on insulating substrates.....	50
Table 2.5: Parameters for the developing of samples prepared at the EBL using PMMA and 2.3 nm of Au as conductive layer.	55
Table 3.1: Summary of the size and dose corrections for the fabrication of SiO ₂ nano gratings.	67
Table 3.2: Fabrication of nanostructures via EBL and metal deposition and lift-off on commercial Si ₃ N ₄ membranes.....	78
Table 3.3: Summary of the fabrication protocol of nano resonators on CaF ₂	85
Table 3.4: Standard recipe for patterning electrical contacts at the EBL for DL of PMMA, and acceleration voltage of 10kV.	98
Table 3.5: Etching recipes for RIE.....	98
Table 3.6: Ion milling recipes.	98

Acronyms

2D	<i>Two-Dimensional</i>
3D	<i>Three-Dimensional</i>
Acc.	<i>Acceleration</i>
AFM	<i>Atomic Force Microscopy</i>
CVD	<i>Chemical Vapor Deposition</i>
cSRR	<i>Complimentary Split Ring Resonator</i>
DI	<i>Deionized</i>
DL	<i>Double Layer</i>
DLW	<i>Direct Laser Writer</i>
EBL	<i>Electron Beam Lithography</i>
EELS	<i>Energy Loss spectroscopy</i>
FTIR	<i>Fourier Transform Infrared</i>
hBN	<i>Hexagonal Boron Nitride</i>
HEPA	<i>High-efficiency particulate</i>
HMDS	<i>Hexamethyldisilazane</i>
HOIP	<i>Hybrid organic-inorganic metal-halide perovskite</i>
IPA	<i>Isopropanol</i>
IR	<i>Infrared</i>
LO	<i>Longitudinal Optical</i>
MIBK	<i>Methyl isobutyl ketone</i>
ML	<i>Multi-layer</i>

PC	<i>Polycarbonate</i>
PCL	<i>Polycaprolactone</i>
PDMS	<i>Polydimethylsiloxane</i>
PEA	<i>Phenethyl ammonium</i>
PL	<i>Photoluminescence</i>
PMMA	<i>Polymethylmethacrylate</i>
PVA	<i>Poly vinyl alcohol</i>
RIE	<i>Reactive Ion Etching</i>
SC	<i>Strong coupling</i>
SEIRA	<i>Surface Enhanced Infrared Absorption Spectroscopy</i>
SEM	<i>Scanning Electron Microscopy</i>
TEM	<i>Transmission Electron Microscopy</i>
TM	<i>Transfer Matrix</i>
TMD	<i>Transition Metal Dichalcogenide</i>
TO	<i>Transversal Optical</i>
USC	<i>Ultrastrong coupling</i>
vdW	<i>van der Waals</i>
VSC	<i>Vibrational Strong Coupling</i>
WF	<i>Write Field</i>

Publications

Microcavity phonon polaritons – from weak to ultrastrong phonon-photon coupling.

María Barra-Burillo, Unai Muniain, Sara Catalano, Marta Autore, Felix Casanova, Luis E. Hueso, Javier Aizpuru, Ruben Esteban, Rainer Hillenbrand. *Nat. Commun.* **12**, 6206 (2021)

Tailoring photoluminescence by strain-engineering in layered perovskite flakes.

Davide Spirito, María Barra-Burillo, Francesco Calavalle, Costanza L. Manganeli, Marco Gobbi, Rainer Hillenbrand, Fèlix Casanova, Luis E. Hueso, Beatriz Martín-García. *Nano Lett.* **22**, 4153 (2022)

Coherent Phononics of van der Waals Layers on Nanogratings.

Wenjing Yan, Andrey V. Akimov, María Barra-Burillo, Manfred Bayer, Jonathan Bradford, Vitalyi E. Gusev, Luis E. Hueso, Anthony Kent, Serhii Kukhtaruk, Achim Nadzeyka, Amalia Patanè, Andrew W. Rushforth, Alexey V. Scherbakov, Dmytro D. Yaremkevich, and Tetiana L. Linnik.

Nano Lett. **22**, 6509 (2022)

Dual-band coupling between nanoscale polaritons and vibrational and electronic excitations in molecules.

A. Bylinkin, F. Calavalle, M. Barra-Burillo, R.V. Kirtaev, E. Nikulina, E.B. Modin, E. Janzen, J.H. Edgar, F. Casanova, L.E. Hueso, V.S. Volkov, P. Vavassori, I. Aharonovich, P. Alonso-Gonzalez, R. Hillenbrand, A.Y. Nikitin. *Nano Lett.* **23**, 3985 (2023)

Real-space observation of ultraconfined in-plane anisotropic acoustic terahertz plasmon polaritons.

S. Chen, P. L. Leng, A. Konečná, E. Modin, M. Gutierrez-Amigo, E. Vicentini, B. Martín-García, M. Barra-Burillo, I. Niehues, C. Maciel Escudero, X. Y. Xie, L. E. Hueso, E. Artacho, J. Aizpurua, I. Errea, M. G. Vergniory, A. Chuvilin, F. X. Xiu, R. Hillenbrand. *Nat. Mater.* **22**, 860 (2023)

Near- and Far-Field Observation of Phonon Polaritons in Wafer Scale Multilayer Hexagonal Boron Nitride Prepared by Chemical Vapor Deposition.

Eugenio Calandrini, Sachin M. Shinde, Subash Sharma, María Barra-Burillo, Andrei Bylinkin, Felix Casanova, Luis E. Hueso, Andrei Chuvilin, Clifford McAleese, Ben R. Conran, Xiaochen Wang, Teo Kenneth, Valentyn S. Volkov, Andrea C. Ferrari, Alexey Y. Nikitin, and Rainer Hillenbrand. *Submitted (2023)*.

Characterizing the backscattered spectrum of Mie spheres.

M. Molezuelas-Ferreras, A. Nodar, M. Barra-Burillo, J. Olmos-Trigo, J. Las-Alonso, I. Gómez-Viloria, E. Posada, J. J. Miguel Varga, R. Esteban, J. Aizpurua, L. E. Hueso, C. Lopez, G. Molin-Terriza. *Submitted (2023)*

References

- [1] K. S. Novoselov, A. Mishchenko, A. Carvalho, and A. H. Castro Neto, *2D Materials and van Der Waals Heterostructures*, *Science* **353**, aac9439 (2016).
- [2] K. S. Novoselov, A. K. Geim, S. V. Morozov, D. Jiang, Y. Zhang, S. V. Dubonos, I. V. Grigorieva, and A. A. Firsov, *Electric Field Effect in Atomically Thin Carbon Films*, *Science* **306**, 666 (2004).
- [3] P. Miró, M. Audiffred, and T. Heine, *An Atlas of Two-Dimensional Materials*, *Chem Soc Rev* **43**, 6537 (2014).
- [4] D. Akinwande et al., *A Review on Mechanics and Mechanical Properties of 2D Materials—Graphene and Beyond*, *Extreme Mech. Lett.* **13**, 42 (2017).
- [5] R. Mas-Ballesté, C. Gómez-Navarro, J. Gómez-Herrero, and F. Zamora, *2D Materials: To Graphene and Beyond*, *Nanoscale* **3**, 20 (2011).
- [6] F. Liu, *Mechanical Exfoliation of Large Area 2D Materials from VdW Crystals*, *Prog. Surf. Sci.* **96**, 100626 (2021).
- [7] J. N. Coleman et al., *Two-Dimensional Nanosheets Produced by Liquid Exfoliation of Layered Materials*, *Science* **331**, 568 (2011).
- [8] V. Nicolosi, M. Chhowalla, M. G. Kanatzidis, M. S. Strano, and J. N. Coleman, *Liquid Exfoliation of Layered Materials*, *Science* **340**, 1226419 (2013).
- [9] C. Huo, Z. Yan, X. Song, and H. Zeng, *2D Materials via Liquid Exfoliation: A Review on Fabrication and Applications*, *Sci. Bull.* **60**, 1994 (2015).
- [10] K. DiCamillo, S. Krylyuk, W. Shi, A. Davydov, and M. Paranjape, *Automated Mechanical Exfoliation of MoS₂ and MoTe₂ Layers for Two-Dimensional Materials Applications*, *IEEE Trans. Nanotechnol.* **18**, 144 (2019).
- [11] Y. Huang et al., *Universal Mechanical Exfoliation of Large-Area 2D Crystals*, *Nat. Commun.* **11**, 2453 (2020).
- [12] H. Li, J. Wu, Z. Yin, and H. Zhang, *Preparation and Applications of Mechanically Exfoliated Single-Layer and Multilayer MoS₂ and WSe₂ Nanosheets*, *Acc. Chem. Res.* **47**, 1067 (2014).
- [13] X. Xu, T. Guo, H. Kim, M. K. Hota, R. S. Alsaadi, M. Lanza, X. Zhang, and H. N. Alshareef, *Growth of 2D Materials at the Wafer Scale*, *Adv. Mater.* **34**, 2108258 (2022).

-
- [14] W. Zheng and L. Y. S. Lee, *Beyond Sonication: Advanced Exfoliation Methods for Scalable Production of 2D Materials*, *Matter* **5**, 515 (2022).
- [15] Z. Cai, B. Liu, X. Zou, and H.-M. Cheng, *Chemical Vapor Deposition Growth and Applications of Two-Dimensional Materials and Their Heterostructures*, *Chem. Rev.* **118**, 6091 (2018).
- [16] F. Huang, *Optical Contrast of Atomically Thin Films*, *J. Phys. Chem. C* **123**, 7440 (2019).
- [17] D. Bing, Y. Wang, J. Bai, R. Du, G. Wu, and L. Liu, *Optical Contrast for Identifying the Thickness of Two-Dimensional Materials*, *Opt. Commun.* **406**, 128 (2018).
- [18] Y. Anzai, M. Yamamoto, S. Genchi, K. Watanabe, T. Taniguchi, S. Ichikawa, Y. Fujiwara, and H. Tanaka, *Broad Range Thickness Identification of Hexagonal Boron Nitride by Colors*, *Appl. Phys. Express* **12**, 055007 (2019).
- [19] H. Li, J. Wu, X. Huang, G. Lu, J. Yang, X. Lu, Q. Xiong, and H. Zhang, *Rapid and Reliable Thickness Identification of Two-Dimensional Nanosheets Using Optical Microscopy*, *ACS Nano* **7**, 10344 (2013).
- [20] A. Rousseau et al., *Monolayer Boron Nitride: Hyperspectral Imaging in the Deep Ultraviolet*, *Nano Lett.* **21**, 10133 (2021).
- [21] Y. Shimazaki, I. Schwartz, K. Watanabe, T. Taniguchi, M. Kroner, and A. Imamoglu, *Strongly Correlated Electrons and Hybrid Excitons in a Moiré Heterostructure*, *Nature* **580**, 472 (2020).
- [22] H. Li, Q. Zhang, C. C. R. Yap, B. K. Tay, T. H. T. Edwin, A. Olivier, and D. Baillargeat, *From Bulk to Monolayer MoS₂: Evolution of Raman Scattering*, *Adv. Funct. Mater.* **22**, 1385 (2012).
- [23] A. N. Barbosa, N. S. Figueroa, M. Giarola, G. Mariotto, and F. L. Freire, *Straightforward Identification of Monolayer WS₂ Structures by Raman Spectroscopy*, *Mater. Chem. Phys.* **243**, 122599 (2020).
- [24] S. Sahoo, R. Palai, and R. S. Katiyar, *Polarized Raman Scattering in Monolayer, Bilayer, and Suspended Bilayer Graphene*, *J. Appl. Phys.* **110**, 044320 (2011).
- [25] Y. ying Wang, Z. hua Ni, T. Yu, Z. X. Shen, H. min Wang, Y. hong Wu, W. Chen, and A. T. Shen Wee, *Raman Studies of Monolayer Graphene: The Substrate Effect*, *J. Phys. Chem. C* **112**, 10637 (2008).
- [26] *Leica Microsystems*, <https://www.leica-microsystems.com/>.
- [27] *Nikon*, https://www.microscope.healthcare.nikon.com/en_EU/.

-
- [28] M. K. Chaudhury and G. M. Whitesides, *Direct Measurement of Interfacial Interactions between Semispherical Lenses and Flat Sheets of Poly(Dimethylsiloxane) and Their Chemical Derivatives*, *Langmuir* **7**, 1013 (1991).
- [29] W. Hiranyawasit, K. Punpattanakul, A. Pimpin, H. Kim, S. Jeon, and W. Srituravanich, *A Novel Method for Transferring Graphene onto PDMS*, *Appl. Surf. Sci.* **358**, 70 (2015).
- [30] B. Jayasena and S. N. Melkote, *An Investigation of PDMS Stamp Assisted Mechanical Exfoliation of Large Area Graphene*, *Procedia Manuf.* **1**, 840 (2015).
- [31] Y. Huang, E. Sutter, N. N. Shi, J. Zheng, T. Yang, D. Englund, H.-J. Gao, and P. Sutter, *Reliable Exfoliation of Large-Area High-Quality Flakes of Graphene and Other Two-Dimensional Materials*, *ACS Nano* **9**, 10612 (2015).
- [32] A. Castellanos-Gomez, M. Buscema, R. Molenaar, V. Singh, L. Janssen, H. S. J. van der Zant, and G. A. Steele, *Deterministic Transfer of Two-Dimensional Materials by All-Dry Viscoelastic Stamping*, *2D Mater.* **1**, 011002 (2014).
- [33] S. Chen et al., *Real-Space Observation of Ultraconfined in-Plane Anisotropic Acoustic Terahertz Plasmon Polaritons*, *Nat. Mater.* **22**, 860 (2023).
- [34] P. J. Zomer, M. H. D. Guimarães, J. C. Brant, N. Tombros, and B. J. van Wees, *Fast Pick up Technique for High Quality Heterostructures of Bilayer Graphene and Hexagonal Boron Nitride*, *Appl. Phys. Lett.* **105**, 013101 (2014).
- [35] C. Dean, A. F. Young, L. Wang, I. Meric, G.-H. Lee, K. Watanabe, T. Taniguchi, K. Shepard, P. Kim, and J. Hone, *Graphene Based Heterostructures*, *Solid State Commun.* **152**, 1275 (2012).
- [36] T. Uwanno, Y. Hattori, T. Taniguchi, K. Watanabe, and K. Nagashio, *Fully Dry PMMA Transfer of Graphene on h-BN Using a Heating/Cooling System*, *2D Mater.* **2**, 041002 (2015).
- [37] Y. Li, S. Weng, R. Niu, W. Zhen, F. Xu, W. Zhu, and C. Zhang, *Poly(Vinyl Alcohol)-Assisted Exfoliation of van Der Waals Materials*, *ACS Omega* **7**, 38774 (2022).
- [38] Y. Liu, N. O. Weiss, X. Duan, H.-C. Cheng, Y. Huang, and X. Duan, *Van Der Waals Heterostructures and Devices*, *Nat. Rev. Mater.* **1**, 16042 (2016).

- [39] C. K. Safeer, J. Ingla-Aynés, N. Ontoso, F. Herling, W. Yan, L. E. Hueso, and F. Casanova, *Spin Hall Effect in Bilayer Graphene Combined with an Insulator up to Room Temperature*, *Nano Lett.* **20**, 4573 (2020).
- [40] F. Herling, C. K. Safeer, J. Ingla-Aynés, N. Ontoso, L. E. Hueso, and F. Casanova, *Gate Tunability of Highly Efficient Spin-to-Charge Conversion by Spin Hall Effect in Graphene Proximitized with WSe₂*, *APL Mater.* **8**, 071103 (2020).
- [41] N. Ontoso et al., *Unconventional Charge-to-Spin Conversion in Graphene/ Mo Te₂ van Der Waals Heterostructures*, *Phys. Rev. Appl.* **19**, 014053 (2023).
- [42] S. Son et al., *Strongly Adhesive Dry Transfer Technique for van Der Waals Heterostructure*, *2D Mater.* **7**, 041005 (2020).
- [43] K. L. Haley, J. A. Cloninger, K. Cerminara, R. M. Sterbentz, T. Taniguchi, K. Watanabe, and J. O. Island, *Heated Assembly and Transfer of Van Der Waals Heterostructures with Common Nail Polish*, *Nanomanufacturing* **1**, 49 (2021).
- [44] A. Jain, P. Bharadwaj, S. Heeg, M. Parzefall, T. Taniguchi, K. Watanabe, and L. Novotny, *Minimizing Residues and Strain in 2D Materials Transferred from PDMS*, *Nanotechnology* **29**, 265203 (2018).
- [45] R. A. B. Devine, D. Mathiot, W. L. Warren, D. M. Fleetwood, and B. Aspar, *Point Defect Generation during High Temperature Annealing of the Si-SiO₂ Interface*, *Appl. Phys. Lett.* **63**, 2926 (1993).
- [46] K. Hofmann, G. W. Rubloff, and R. A. McCorkle, *Defect Formation in Thermal SiO₂ by High-temperature Annealing*, *Appl. Phys. Lett.* **49**, 1525 (1986).
- [47] Y. Liu, C. Liu, Z. Ma, G. Zheng, Y. Ma, and Z. Sheng, *Annealing Effect on Photoluminescence of Two Dimensional WSe₂/BN Heterostructure*, *Appl. Phys. Lett.* **117**, 233103 (2020).
- [48] L. Schnitzspan, J. Cramer, J. Kubik, M. Tarequzzaman, G. Jakob, and M. Klaui, *Impact of Annealing Temperature on Tunneling Magnetoresistance Multilayer Stacks*, *IEEE Magn. Lett.* **11**, 1 (2020).
- [49] E. Harvey and M. Ghantasala, *12 - Nanofabrication*, in *Nanostructure Control of Materials*, edited by R. H. J. Hannink and A. J. Hill (Woodhead Publishing, 2006), pp. 303–330.
- [50] *Cleanroom* / *CIC* *NanoGUNE*, <https://www.nanogune.eu/en/nanogune/glance/facilities-equipment/equipment/cleanroom>.

-
- [51] B. Bhushan, editor, *Encyclopedia of Nanotechnology* (Springer Netherlands, Dordrecht, 2012).
- [52] J. Ai, Q. Du, Z. Qin, J. Liu, and X. Zeng, *Laser Direct-Writing Lithography Equipment System for Rapid and Mm-Precision Fabrication on Curved Surfaces with Large Sag Heights*, *Opt. Express* **26**, 20965 (2018).
- [53] D. Bäuerle, *Laser Processing and Chemistry* (Springer Berlin Heidelberg, Berlin, Heidelberg, 2011).
- [54] M. Häfner, C. Pruss, and W. Osten, *Laser Direct Writing: Recent Developments for the Making of Diffractive Optics*, *Opt. Photonik* **6**, 40 (2011).
- [55] R. F. W. Pease, *Electron Beam Lithography*, *Contemp. Phys.* **22**, 265 (1981).
- [56] M. A. Mohammad, M. Muhammad, S. K. Dew, and M. Stepanova, *Fundamentals of Electron Beam Exposure and Development*, in *Nanofabrication*, edited by M. Stepanova and S. Dew (Springer Vienna, Vienna, 2012), pp. 11–41.
- [57] P. Naulleau, *Optical Lithography*, in *Comprehensive Nanoscience and Nanotechnology* (Elsevier, 2019), pp. 387–398.
- [58] H. Ni, G. Yuan, L. Sun, N. Chang, D. Zhang, R. Chen, L. Jiang, H. Chen, Z. Gu, and X. Zhao, *Large-Scale High-Numerical-Aperture Super-Oscillatory Lens Fabricated by Direct Laser Writing Lithography*, *RSC Adv.* **8**, 20117 (2018).
- [59] K. Coimbatore Balram et al., *The Nanolithography Toolbox*, *J. Res. Natl. Inst. Stand. Technol.* **121**, 464 (2016).
- [60] *Direct Laser Writer | Heidelberg Instruments*, <https://heidelberg-instruments.com/product/%ce%bcmla/>.
- [61] S. Okazaki, *Resolution Limits of Optical Lithography*, *J. Vac. Sci. Technol. B Microelectron. Nanometer Struct.* **9**, 2829 (1991).
- [62] J. Fischer, G. von Freymann, and M. Wegener, *The Materials Challenge in Diffraction-Unlimited Direct-Laser-Writing Optical Lithography*, *Adv. Mater.* **22**, 3578 (2010).
- [63] *Raith 150 TWO*, <https://raith.com/product/raith150-two/>.
- [64] C. A. Mack and J. E. Connors, *Fundamental Differences between Positive- and Negative-Tone Imaging*, in edited by J. D. Cuthbert (San Jose, United States, 1992), p. 328.

-
- [65] M. Hatzakis, B. J. Canavello, and J. M. Shaw, *Single-Step Optical Lift-Off Process*, IBM J. Res. Dev. **24**, 452 (1980).
- [66] A. S. Gangnaik, Y. M. Georgiev, and J. D. Holmes, *New Generation Electron Beam Resists: A Review*, Chem. Mater. **29**, 1898 (2017).
- [67] T. Manouras and P. Argitis, *High Sensitivity Resists for EUV Lithography: A Review of Material Design Strategies and Performance Results*, Nanomaterials **10**, 1593 (2020).
- [68] M. Yoshiiwa, H. Kageyama, Y. Shirota, F. Wakaya, K. Gamo, and M. Takai, *Novel Class of Low Molecular-weight Organic Resists for Nanometer Lithography*, Appl. Phys. Lett. **69**, 2605 (1996).
- [69] *Image Reversal Resist Processing*, (n.d.).
- [70] S. Ramadan, Y. Zhang, D. K. H. Tsang, O. Shaforost, L. Xu, R. Bower, I. E. Dunlop, P. K. Petrov, and N. Klein, *Enhancing Structural Properties and Performance of Graphene-Based Devices Using Self-Assembled HMDS Monolayers*, ACS Omega **6**, 4767 (2021).
- [71] E. Seo, B. K. Choi, and O. Kim, *Determination of Proximity Effect Parameters and the Shape Bias Parameter in Electron Beam Lithography*, Microelectron. Eng. **53**, 305 (2000).
- [72] P. J. Kelly and R. D. Arnell, *Magnetron Sputtering: A Review of Recent Developments and Applications*, Vacuum **56**, 159 (2000).
- [73] H. Ekinçi, *Plasma and Reactive Ion Etching*, in *Reference Module in Materials Science and Materials Engineering* (Elsevier, 2016).
- [74] A. Carvalho, A. S. Rodin, and A. H. Castro Neto, *Phosphorene Nanoribbons*, EPL Europhys. Lett. **108**, 47005 (2014).
- [75] Y.-W. Son, M. L. Cohen, and S. G. Louie, *Energy Gaps in Graphene Nanoribbons*, Phys. Rev. Lett. **97**, 216803 (2006).
- [76] M. Yagmurcukardes, F. M. Peeters, R. T. Senger, and H. Sahin, *Nanoribbons: From Fundamentals to State-of-the-Art Applications*, Appl. Phys. Rev. **3**, 041302 (2016).
- [77] Y. Long et al., *Magnetic Coupling Metasurface for Achieving Broad-Band and Broad-Angular Absorption in the MoS₂ Monolayer*, Opt. Mater. Express **7**, 100 (2017).
- [78] J. Lu, J. Yao, J. Yan, W. Gao, L. Huang, Z. Zheng, M. Zhang, and J. Li, *Strain Engineering Coupled with Optical Regulation towards a High-Sensitivity In₂S₃ Photodetector*, Mater. Horiz. **7**, 1427 (2020).
- [79] G. Hu, A. Krasnok, Y. Mazor, C.-W. Qiu, and A. Alù, *Moiré Hyperbolic Metasurfaces*, Nano Lett. **20**, 3217 (2020).

-
- [80] W. Yan et al., *Coherent Phononics of van Der Waals Layers on Nanogratings*, Nano Lett. **22**, 6509 (2022).
- [81] Z. Dai, L. Liu, and Z. Zhang, *Strain Engineering of 2D Materials: Issues and Opportunities at the Interface*, Adv. Mater. **31**, 1805417 (2019).
- [82] Z. Peng, X. Chen, Y. Fan, D. J. Srolovitz, and D. Lei, *Strain Engineering of 2D Semiconductors and Graphene: From Strain Fields to Band-Structure Tuning and Photonic Applications*, Light Sci. Appl. **9**, 190 (2020).
- [83] F. Vialla and N. D. Fatti, *Time-Domain Investigations of Coherent Phonons in van Der Waals Thin Films*, Nanomaterials **10**, 2543 (2020).
- [84] P. Soubelet, A. A. Reynoso, A. Fainstein, K. Nogajewski, M. Potemski, C. Faugeras, and A. E. Bruchhausen, *The Lifetime of Interlayer Breathing Modes of Few-Layer 2H-MoSe₂ Membranes*, Nanoscale **11**, 10446 (2019).
- [85] M. K. Zalalutdinov et al., *Acoustic Cavities in 2D Heterostructures*, Nat. Commun. **12**, 3267 (2021).
- [86] D. N. Basov, M. M. Fogler, and F. J. García de Abajo, *Polaritons in van Der Waals Materials*, Science **354**, aag1992 (2016).
- [87] T. Low, A. Chaves, J. D. Caldwell, A. Kumar, N. X. Fang, P. Avouris, T. F. Heinz, F. Guinea, L. Martin-Moreno, and F. Koppens, *Polaritons in Layered Two-Dimensional Materials*, Nat. Mater. **16**, 182 (2017).
- [88] Q. Zhang, G. Hu, W. Ma, P. Li, A. Krasnok, R. Hillenbrand, A. Alù, and C.-W. Qiu, *Interface Nano-Optics with van Der Waals Polaritons*, Nature **597**, 187 (2021).
- [89] D. Rodrigo, O. Limaj, D. Janner, D. Etezadi, F. J. García de Abajo, V. Pruneri, and H. Altug, *Mid-Infrared Plasmonic Biosensing with Graphene*, Science **349**, 165 (2015).
- [90] M. Autore et al., *Enhanced Light–Matter Interaction in ¹⁰B Monoisotopic Boron Nitride Infrared Nanoresonators*, Adv. Opt. Mater. **9**, 2001958 (2021).
- [91] M. Autore et al., *Boron Nitride Nanoresonators for Phonon-Enhanced Molecular Vibrational Spectroscopy at the Strong Coupling Limit*, Light Sci. Appl. **7**, 17172 (2017).
- [92] I. Dolado et al., *Nanoscale Guiding of Infrared Light with Hyperbolic Volume and Surface Polaritons in van Der Waals Material Ribbons*, Adv. Mater. **32**, 1906530 (2020).
- [93] E. J. C. Dias, R. Yu, and F. J. García de Abajo, *Thermal Manipulation of Plasmons in Atomically Thin Films*, Light Sci. Appl. **9**, 87 (2020).

-
- [94] Y. Wu, J. Ordonez-Miranda, S. Gluchko, R. Anufriev, D. D. S. Meneses, L. Del Campo, S. Volz, and M. Nomura, *Enhanced Thermal Conduction by Surface Phonon-Polaritons*, *Sci. Adv.* **6**, eabb4461 (2020).
- [95] X. Li et al., *Large-Area Synthesis of High-Quality and Uniform Graphene Films on Copper Foils*, *Science* **324**, 1312 (2009).
- [96] N. Jr. Bareza et al., *Phonon-Enhanced Mid-Infrared CO₂ Gas Sensing Using Boron Nitride Nanoresonators*, *ACS Photonics* **9**, 34 (2022).
- [97] H. Hu, X. Yang, X. Guo, K. Khaliji, S. R. Biswas, F. J. García de Abajo, T. Low, Z. Sun, and Q. Dai, *Gas Identification with Graphene Plasmons*, *Nat. Commun.* **10**, 1131 (2019).
- [98] F. H. L. Koppens, T. Mueller, Ph. Avouris, A. C. Ferrari, M. S. Vitiello, and M. Polini, *Photodetectors Based on Graphene, Other Two-Dimensional Materials and Hybrid Systems*, *Nat. Nanotechnol.* **9**, 780 (2014).
- [99] Eugenio Calandrini, Sachin M. Shinde, Subash Sharma, Maria Barra Burillo, Andrei Bylinkin, Felix Casanova, Luis E. Hueso, Andrei Chuvilin, Clifford McAleese, Ben R. Conran, Xiaochen Wang, Teo Kenneth, Valentyn S. Volkov, Andrea C. Ferrari, Alexey Y. Nikitin, and Rainer Hillenbrand, *Near- and Far-Field Observation of Phonon Polaritons in Wafer Scale Multilayer Hexagonal Boron Nitride Prepared by Chemical Vapor Deposition*, Submitted (2023).
- [100] J. Qin et al., *Nanophotonic Devices Based on Magneto-Optical Materials: Recent Developments and Applications*, *Nanophotonics* **11**, 2639 (2022).
- [101] A. Kimel et al., *The 2022 Magneto-Optics Roadmap*, *J. Phys. Appl. Phys.* **55**, 463003 (2022).
- [102] A. López-Ortega, M. Zapata-Herrera, N. Maccaferri, M. Pancaldi, M. Garcia, A. Chuvilin, and P. Vavassori, *Enhanced Magnetic Modulation of Light Polarization Exploiting Hybridization with Multipolar Dark Plasmons in Magnetoplasmonic Nanocavities*, *Light Sci. Appl.* **9**, 49 (2020).
- [103] F. Hao, E. M. Larsson, T. A. Ali, D. S. Sutherland, and P. Nordlander, *Shedding Light on Dark Plasmons in Gold Nanorings*, *Chem. Phys. Lett.* **458**, 262 (2008).
- [104] P. Nordlander, *The Ring: A Leitmotif in Plasmonics*, *ACS Nano* **3**, 488 (2009).
- [105] M. Prieto, R. Arenal, L. Henrard, L. Gomez, V. Sebastian, and M. Arruebo, *Morphological Tunability of the Plasmonic Response: From*

- Hollow Gold Nanoparticles to Gold Nanorings*, J. Phys. Chem. C **118**, 28804 (2014).
- [106] G. T. Forcherio, D. DeJarnette, M. Benamara, and D. K. Roper, *Electron Energy Loss Spectroscopy of Surface Plasmon Resonances on Aberrant Gold Nanostructures*, J. Phys. Chem. C **120**, 24950 (2016).
- [107] B. D. Dana, A. N. Koya, X. Song, and J. Lin, *Effect of Symmetry Breaking on Plasmonic Coupling in Nanoring Dimers*, Plasmonics **15**, 1977 (2020).
- [108] H. Kim, J. S. Han, J. Choi, S. Y. Kim, and H. W. Jang, *Halide Perovskites for Applications beyond Photovoltaics*, Small Methods **2**, 1700310 (2018).
- [109] D. W. deQuilettes, S. Koch, S. Burke, R. K. Paranjli, A. J. Shropshire, M. E. Ziffer, and D. S. Ginger, *Photoluminescence Lifetimes Exceeding 8 Ms and Quantum Yields Exceeding 30% in Hybrid Perovskite Thin Films by Ligand Passivation*, ACS Energy Lett. **1**, 438 (2016).
- [110] G. H. Ahmed, J. K. El-Demellawi, J. Yin, J. Pan, D. B. Velusamy, M. N. Hedhili, E. Alarousu, O. M. Bakr, H. N. Alshareef, and O. F. Mohammed, *Giant Photoluminescence Enhancement in CsPbCl₃ Perovskite Nanocrystals by Simultaneous Dual-Surface Passivation*, ACS Energy Lett. **3**, 2301 (2018).
- [111] Z. Xiao, Z. Song, and Y. Yan, *From Lead Halide Perovskites to Lead-Free Metal Halide Perovskites and Perovskite Derivatives*, Adv. Mater. **31**, 1803792 (2019).
- [112] G. Adamo, H. N. Swaha Krishnamoorthy, D. Cortecchia, B. Chaudhary, V. Nalla, N. I. Zheludev, and C. Soci, *Metamaterial Enhancement of Metal-Halide Perovskite Luminescence*, Nano Lett. **20**, 7906 (2020).
- [113] V. Giannini, A. I. Fernández-Domínguez, S. C. Heck, and S. A. Maier, *Plasmonic Nanoantennas: Fundamentals and Their Use in Controlling the Radiative Properties of Nanoemitters*, Chem. Rev. **111**, 3888 (2011).
- [114] Y. Park, J. Kim, Y.-G. Roh, and Q.-H. Park, *Optical Slot Antennas and Their Applications to Photonic Devices*, Nanophotonics **7**, 1617 (2018).
- [115] P. Forn-Díaz, L. Lamata, E. Rico, J. Kono, and E. Solano, *Ultrastrong Coupling Regimes of Light-Matter Interaction*, Rev. Mod. Phys. **91**, 025005 (2019).
- [116] J. Flick, N. Rivera, and P. Narang, *Strong Light-Matter Coupling in Quantum Chemistry and Quantum Photonics*, Nanophotonics **7**, 1479 (2018).
- [117] A. Thomas et al., *Tilting a Ground-State Reactivity Landscape by Vibrational Strong Coupling*, Science **363**, 615 (2019).

- [118] Y. Ashida, A. Imamoglu, J. Faist, D. Jaksch, A. Cavalleri, and E. Demler, *Quantum Electrodynamical Control of Matter: Cavity-Enhanced Ferroelectric Phase Transition*, Phys. Rev. X **10**, 041027 (2020).
- [119] S. Rajabali, S. Markmann, E. Jöchl, M. Beck, C. A. Lehner, W. Wegscheider, J. Faist, and G. Scalari, *An Ultrastrongly Coupled Single Terahertz Meta-Atom*, Nat. Commun. **13**, 2528 (2022).
- [120] G. Scalari et al., *Ultrastrong Coupling of the Cyclotron Transition of a 2D Electron Gas to a THz Metamaterial*, Science **335**, 1323 (2012).
- [121] G. M. Andolina, F. M. D. Pellegrino, V. Giovannetti, A. H. MacDonald, and M. Polini, *Theory of Photon Condensation in a Spatially Varying Electromagnetic Field*, Phys. Rev. B **102**, 125137 (2020).
- [122] P. Nataf and C. Ciuti, *No-Go Theorem for Superradiant Quantum Phase Transitions in Cavity QED and Counter-Example in Circuit QED*, Nat. Commun. **1**, 72 (2010).
- [123] L. Wang et al., *One-Dimensional Electrical Contact to a Two-Dimensional Material*, Science **342**, 614 (2013).
- [124] B. Karpiak, A. Dankert, A. W. Cummings, S. R. Power, S. Roche, and S. P. Dash, *1D Ferromagnetic Edge Contacts to 2D Graphene/h-BN Heterostructures*, 2D Mater. **5**, 014001 (2017).
- [125] S. Grenadier, J. Li, J. Lin, and H. Jiang, *Dry Etching Techniques for Active Devices Based on Hexagonal Boron Nitride Epilayers*, J. Vac. Sci. Technol. Vac. Surf. Films **31**, 061517 (2013).
- [126] J. Son et al., *Atomically Precise Graphene Etch Stops for Three Dimensional Integrated Systems from Two Dimensional Material Heterostructures*, Nat. Commun. **9**, 3988 (2018).
- [127] A. Jain, Á. Szabó, M. Parzefall, E. Bonvin, T. Taniguchi, K. Watanabe, P. Bharadwaj, M. Luisier, and L. Novotny, *One-Dimensional Edge Contacts to a Monolayer Semiconductor*, Nano Lett. **19**, 6914 (2019).
- [128] Z. Li et al., *Efficient Strain Modulation of 2D Materials via Polymer Encapsulation*, Nat. Commun. **11**, 1151 (2020).
- [129] A. Chaves et al., *Bandgap Engineering of Two-Dimensional Semiconductor Materials*, Npj 2D Mater. Appl. **4**, 29 (2020).
- [130] R. Zhao, Y. Wang, D. Deng, X. Luo, W. J. Lu, Y.-P. Sun, Z.-K. Liu, L.-Q. Chen, and J. Robinson, *Tuning Phase Transitions in 1T-TaS₂ via the Substrate*, Nano Lett. **17**, 3471 (2017).

-
- [131] R. Roldán, A. Castellanos-Gomez, E. Cappelluti, and F. Guinea, *Strain Engineering in Semiconducting Two-Dimensional Crystals*, J. Phys. Condens. Matter **27**, 313201 (2015).
- [132] Y. K. Ryu, F. Carrascoso, R. López-Nebreda, N. Agraït, R. Frisenda, and A. Castellanos-Gomez, *Microheater Actuators as a Versatile Platform for Strain Engineering in 2D Materials*, Nano Lett. **20**, 5339 (2020).
- [133] D. Spirito, M. Barra-Burillo, F. Calavalle, C. L. Manganeli, M. Gobbi, R. Hillenbrand, F. Casanova, L. E. Hueso, and B. Martín-García, *Tailoring Photoluminescence by Strain-Engineering in Layered Perovskite Flakes*, Nano Lett. **22**, 4153 (2022).
- [134] X. Li, J. M. Hoffman, and M. G. Kanatzidis, *The 2D Halide Perovskite Rulebook: How the Spacer Influences Everything from the Structure to Optoelectronic Device Efficiency*, Chem. Rev. **121**, 2230 (2021).
- [135] K. M. Boopathi et al., *Permanent Lattice Compression of Lead-Halide Perovskite for Persistently Enhanced Optoelectronic Properties*, ACS Energy Lett. **5**, 642 (2020).
- [136] J.-C. Blancon, J. Even, Costas. C. Stoumpos, Mercouri. G. Kanatzidis, and A. D. Mohite, *Semiconductor Physics of Organic-Inorganic 2D Halide Perovskites*, Nat. Nanotechnol. **15**, 969 (2020).
- [137] L. Dou, Y. Yang, J. You, Z. Hong, W.-H. Chang, G. Li, and Y. Yang, *Solution-Processed Hybrid Perovskite Photodetectors with High Detectivity*, Nat. Commun. **5**, 5404 (2014).
- [138] J. Ghosh and P. K. Giri, *Recent Advances in Perovskite/2D Materials Based Hybrid Photodetectors*, J. Phys. Mater. **4**, 032008 (2021).
- [139] W. Tian, H. Zhou, and L. Li, *Hybrid Organic-Inorganic Perovskite Photodetectors*, Small **13**, 1702107 (2017).
- [140] Y. Hou et al., *Efficient Tandem Solar Cells with Solution-Processed Perovskite on Textured Crystalline Silicon*, Science **367**, 1135 (2020).
- [141] K. Lin et al., *Perovskite Light-Emitting Diodes with External Quantum Efficiency Exceeding 20 per Cent*, Nature **562**, 245 (2018).
- [142] Y. Chen et al., *Strain Engineering and Epitaxial Stabilization of Halide Perovskites*, Nature **577**, 209 (2020).
- [143] E. G. Moloney, V. Yeddu, and M. I. Saidaminov, *Strain Engineering in Halide Perovskites*, ACS Mater. Lett. **2**, 1495 (2020).
- [144] I. Spanopoulos et al., *Uniaxial Expansion of the 2D Ruddlesden-Popper Perovskite Family for Improved Environmental Stability*, J. Am. Chem. Soc. **141**, 5518 (2019).

- [145] S. Wang et al., *The Strain Effects in 2D Hybrid Organic–Inorganic Perovskite Microplates: Bandgap, Anisotropy and Stability*, *Nanoscale* **12**, 6644 (2020).
- [146] Q. Tu, I. Spanopoulos, S. Hao, C. Wolverton, M. G. Kanatzidis, G. S. Shekhawat, and V. P. Dravid, *Probing Strain-Induced Band Gap Modulation in 2D Hybrid Organic–Inorganic Perovskites*, *ACS Energy Lett.* **4**, 796 (2019).
- [147] B. Vargas, G. Rodríguez-López, and D. Solis-Ibarra, *The Emergence of Halide Layered Double Perovskites*, *ACS Energy Lett.* **5**, 3591 (2020).
- [148] Q. Tu, I. Spanopoulos, E. S. Vasileiadou, X. Li, M. G. Kanatzidis, G. S. Shekhawat, and V. P. Dravid, *Exploring the Factors Affecting the Mechanical Properties of 2D Hybrid Organic–Inorganic Perovskites*, *ACS Appl. Mater. Interfaces* **12**, 20440 (2020).
- [149] Q. Tu, I. Spanopoulos, S. Hao, C. Wolverton, M. G. Kanatzidis, G. S. Shekhawat, and V. P. Dravid, *Out-of-Plane Mechanical Properties of 2D Hybrid Organic–Inorganic Perovskites by Nanoindentation*, *ACS Appl. Mater. Interfaces* **10**, 22167 (2018).
- [150] M. A. Reyes-Martinez, P. Tan, A. Kakekhani, S. Banerjee, A. A. Zhumekenov, W. Peng, O. M. Bakr, A. M. Rappe, and Y.-L. Loo, *Unraveling the Elastic Properties of (Quasi)Two-Dimensional Hybrid Perovskites: A Joint Experimental and Theoretical Study*, *ACS Appl. Mater. Interfaces* **12**, 17881 (2020).
- [151] C. C. Stoumpos, D. H. Cao, D. J. Clark, J. Young, J. M. Rondinelli, J. I. Jang, J. T. Hupp, and M. G. Kanatzidis, *Ruddlesden–Popper Hybrid Lead Iodide Perovskite 2D Homologous Semiconductors*, *Chem. Mater.* **28**, 2852 (2016).
- [152] M. Dyksik, S. Wang, W. Paritmongkol, D. K. Maude, W. A. Tisdale, M. Baranowski, and P. Plochocka, *Tuning the Excitonic Properties of the 2D (PEA)₂(MA)_{n-1}Pb_nI_{3n+1} Perovskite Family via Quantum Confinement*, *J. Phys. Chem. Lett.* **12**, 1638 (2021).
- [153] L. Dou et al., *Atomically Thin Two-Dimensional Organic-Inorganic Hybrid Perovskites*, *Science* **349**, 1518 (2015).
- [154] M. Kepenekian et al., *Concept of Lattice Mismatch and Emergence of Surface States in Two-Dimensional Hybrid Perovskite Quantum Wells*, *Nano Lett.* **18**, 5603 (2018).

-
- [155] A. Jaffe, Y. Lin, and H. I. Karunadasa, *Halide Perovskites under Pressure: Accessing New Properties through Lattice Compression*, ACS Energy Lett. **2**, 1549 (2017).
- [156] D.-J. Xue et al., *Regulating Strain in Perovskite Thin Films through Charge-Transport Layers*, Nat. Commun. **11**, 1514 (2020).
- [157] D. Liu, D. Luo, A. N. Iqbal, K. W. P. Orr, T. A. S. Doherty, Z.-H. Lu, S. D. Stranks, and W. Zhang, *Strain Analysis and Engineering in Halide Perovskite Photovoltaics*, Nat. Mater. **20**, 1337 (2021).
- [158] O. Yaffe et al., *Local Polar Fluctuations in Lead Halide Perovskite Crystals*, Phys. Rev. Lett. **118**, 136001 (2017).
- [159] J. Ibaceta-Jaña et al., *Vibrational Dynamics in Lead Halide Hybrid Perovskites Investigated by Raman Spectroscopy*, Phys. Chem. Chem. Phys. **22**, 5604 (2020).
- [160] L. Zhang, L. Wu, K. Wang, and B. Zou, *Pressure-Induced Broadband Emission of 2D Organic-Inorganic Hybrid Perovskite (C₆H₅C₂H₄NH₃)₂PbBr₄*, Adv. Sci. **6**, 1801628 (2019).
- [161] M. I. Dar, G. Jacopin, S. Meloni, A. Mattoni, N. Arora, A. Boziki, S. M. Zakeeruddin, U. Rothlisberger, and M. Grätzel, *Origin of Unusual Bandgap Shift and Dual Emission in Organic-Inorganic Lead Halide Perovskites*, Sci. Adv. **2**, e1601156 (2016).
- [162] A. Dobrovolsky, A. Merdasa, J. Li, K. Hirselandt, E. L. Unger, and I. G. Scheblykin, *Relating Defect Luminescence and Nonradiative Charge Recombination in MAPbI₃ Perovskite Films*, J. Phys. Chem. Lett. **11**, 1714 (2020).
- [163] D. Tedeschi et al., *Controlled Micro/Nanodome Formation in Proton-Irradiated Bulk Transition-Metal Dichalcogenides*, Adv. Mater. **31**, 1903795 (2019).
- [164] M. Barra-Burillo, U. Muniain, S. Catalano, M. Autore, F. Casanova, L. E. Hueso, J. Aizpurua, R. Esteban, and R. Hillenbrand, *Microcavity Phonon Polaritons from the Weak to the Ultrastrong Phonon-Photon Coupling Regime*, Nat. Commun. **12**, 6206 (2021).
- [165] D. S. Dovzhenko, S. V. Ryabchuk, Yu. P. Rakovich, and I. R. Nabiev, *Light-Matter Interaction in the Strong Coupling Regime: Configurations, Conditions, and Applications*, Nanoscale **10**, 3589 (2018).
- [166] A. V. Kavokin, J. J. Baumberg, G. Malpuech, and F. P. Laussy, *Microcavities*, Vol. 21 (Oxford university press, 2017).

- [167] A. Rahimi-Iman, *Polariton Physics: From Dynamic Bose–Einstein Condensates in Strongly-Coupled Light–Matter Systems to Polariton Lasers*, Vol. 229 (Springer International Publishing, Cham, 2020).
- [168] P. Törmä and W. L. Barnes, *Strong Coupling between Surface Plasmon Polaritons and Emitters: A Review*, Rep. Prog. Phys. **78**, 013901 (2015).
- [169] D. G. Lidzey, D. D. C. Bradley, M. S. Skolnick, T. Virgili, S. Walker, and D. M. Whittaker, *Strong Exciton–Photon Coupling in an Organic Semiconductor Microcavity*, Nature **395**, 53 (1998).
- [170] J. Klaers, J. Schmitt, F. Vewinger, and M. Weitz, *Bose–Einstein Condensation of Photons in an Optical Microcavity*, Nature **468**, 545 (2010).
- [171] J. Kasprzak et al., *Bose–Einstein Condensation of Exciton Polaritons*, Nature **443**, 409 (2006).
- [172] M. D. Fraser, S. Höfling, and Y. Yamamoto, *Physics and Applications of Exciton–Polariton Lasers*, Nat. Mater. **15**, 1049 (2016).
- [173] S. De Liberato, C. Ciuti, and C. C. Phillips, *Terahertz Lasing from Intersubband Polariton–Polariton Scattering in Asymmetric Quantum Wells*, Phys. Rev. B **87**, 241304 (2013).
- [174] D. Dini, R. Köhler, A. Tredicucci, G. Biasiol, and L. Sorba, *Microcavity Polariton Splitting of Intersubband Transitions*, Phys. Rev. Lett. **90**, 116401 (2003).
- [175] S. De Liberato and C. Ciuti, *Stimulated Scattering and Lasing of Intersubband Cavity Polaritons*, Phys. Rev. Lett. **102**, 136403 (2009).
- [176] L. Sapienza, A. Vasanelli, R. Colombelli, C. Ciuti, Y. Chassagneux, C. Manquest, U. Gennser, and C. Sirtori, *Electrically Injected Cavity Polaritons*, Phys. Rev. Lett. **100**, 136806 (2008).
- [177] N. C. Passler, C. R. Gubbin, T. G. Folland, I. Razdolski, D. S. Katzer, D. F. Storm, M. Wolf, S. De Liberato, J. D. Caldwell, and A. Paarmann, *Strong Coupling of Epsilon-Near-Zero Phonon Polaritons in Polar Dielectric Heterostructures*, Nano Lett. **18**, 4285 (2018).
- [178] A. Shalabney, J. George, H. Hiura, J. A. Hutchison, C. Genet, P. Hellwig, and T. W. Ebbesen, *Enhanced Raman Scattering from Vibro-Polariton Hybrid States*, Angew. Chem. **127**, 8082 (2015).
- [179] S. Wang, A. Mika, J. A. Hutchison, C. Genet, A. Jouaiti, M. W. Hosseini, and T. W. Ebbesen, *Phase Transition of a Perovskite Strongly Coupled to the Vacuum Field*, Nanoscale **6**, 7243 (2014).

-
- [180] J. A. Hutchison, T. Schwartz, C. Genet, E. Devaux, and T. W. Ebbesen, *Modifying Chemical Landscapes by Coupling to Vacuum Fields*, *Angew. Chem. Int. Ed.* **51**, 1592 (2012).
- [181] A. Bylinkin et al., *Real-Space Observation of Vibrational Strong Coupling between Propagating Phonon Polaritons and Organic Molecules*, *Nat. Photonics* **15**, 197 (2021).
- [182] T. Feurer, J. C. Vaughan, and K. A. Nelson, *Spatiotemporal Coherent Control of Lattice Vibrational Waves*, *Science* **299**, 374 (2003).
- [183] N. S. Stoyanov, T. Feurer, D. W. Ward, E. R. Statz, and K. A. Nelson, *Direct Visualization of a Polariton Resonator in the THz Regime*, *Opt. Express* **12**, 2387 (2004).
- [184] P. Sivarajah, A. Steinbacher, B. Dastrup, J. Lu, M. Xiang, W. Ren, S. Kamba, S. Cao, and K. A. Nelson, *THz-Frequency Magnon-Phonon-Polaritons in the Collective Strong-Coupling Regime*, *J. Appl. Phys.* **125**, 213103 (2019).
- [185] K. Ohtani, B. Meng, M. Franckić, L. Bosco, C. Ndebeka-Bandou, M. Beck, and J. Faist, *An Electrically Pumped Phonon-Polariton Laser*, *Sci. Adv.* **5**, eaau1632 (2019).
- [186] M. Franckić, C. Ndebeka-Bandou, K. Ohtani, and J. Faist, *Quantum Model of Gain in Phonon-Polariton Lasers*, *Phys. Rev. B* **97**, 075402 (2018).
- [187] J. D. Caldwell et al., *Sub-Diffractive Volume-Confined Polaritons in the Natural Hyperbolic Material Hexagonal Boron Nitride*, *Nat. Commun.* **5**, 5221 (2014).
- [188] S. Dai et al., *Tunable Phonon Polaritons in Atomically Thin van Der Waals Crystals of Boron Nitride*, *Science* **343**, 1125 (2014).
- [189] J. D. Caldwell, L. Lindsay, V. Giannini, I. Vurgaftman, T. L. Reinecke, S. A. Maier, and O. J. Glembocki, *Low-Loss, Infrared and Terahertz Nanophotonics Using Surface Phonon Polaritons*, *Nanophotonics* **4**, 44 (2015).
- [190] S. Foteinopoulou, G. C. R. Devarapu, G. S. Subramania, S. Krishna, and D. Wasserman, *Phonon-Polaritonics: Enabling Powerful Capabilities for Infrared Photonics*, *Nanophotonics* **8**, 2129 (2019).
- [191] J. D. Caldwell et al., *Low-Loss, Extreme Subdiffraction Photon Confinement via Silicon Carbide Localized Surface Phonon Polariton Resonators*, *Nano Lett.* **13**, 3690 (2013).

-
- [192] F. J. Alfaro-Mozaz et al., *Nanoimaging of Resonating Hyperbolic Polaritons in Linear Boron Nitride Antennas*, Nat. Commun. **8**, 15624 (2017).
- [193] D. J. Shelton, I. Brener, J. C. Ginn, M. B. Sinclair, D. W. Peters, K. R. Coffey, and G. D. Boreman, *Strong Coupling between Nanoscale Metamaterials and Phonons*, Nano Lett. **11**, 2104 (2011).
- [194] C. Huck, J. Vogt, T. Neuman, T. Nagao, R. Hillenbrand, J. Aizpurua, A. Pucci, and F. Neubrech, *Strong Coupling between Phonon-Polaritons and Plasmonic Nanorods*, Opt. Express **24**, 25528 (2016).
- [195] P. Pons-Valencia et al., *Launching of Hyperbolic Phonon-Polaritons in h-BN Slabs by Resonant Metal Plasmonic Antennas*, Nat. Commun. **10**, 3242 (2019).
- [196] D. Yoo, F. De León-Pérez, M. Pelton, I.-H. Lee, D. A. Mohr, M. B. Raschke, J. D. Caldwell, L. Martín-Moreno, and S.-H. Oh, *Ultrastrong Plasmon-Phonon Coupling via Epsilon-near-Zero Nanocavities*, Nat. Photonics **15**, 125 (2021).
- [197] N. W. Ashcroft and N. D. Mermin, *Solid State Physics* (Saunders College, 1976).
- [198] H. J. Bakker, S. Hunsche, and H. Kurz, *Coherent Phonon Polaritons as Probes of Anharmonic Phonons in Ferroelectrics*, Rev. Mod. Phys. **70**, 523 (1998).
- [199] A. Thomas, E. Devaux, K. Nagarajan, G. Rogez, M. Seidel, F. Richard, C. Genet, M. Drillon, and T. W. Ebbesen, *Large Enhancement of Ferromagnetism under a Collective Strong Coupling of YBCO Nanoparticles*, Nano Lett. **21**, 4365 (2021).
- [200] Y. He et al., *Rapid Change of Superconductivity and Electron-Phonon Coupling through Critical Doping in Bi-2212*, Science **362**, 62 (2018).
- [201] A. Thomas et al., *Exploring Superconductivity under Strong Coupling with the Vacuum Electromagnetic Field*, arXiv:1911.01459.
- [202] J. D. Caldwell, I. Aharonovich, G. Cassabois, J. H. Edgar, B. Gil, and D. N. Basov, *Photonics with Hexagonal Boron Nitride*, Nat. Rev. Mater. **4**, 552 (2019).
- [203] N. C. Passler and A. Paarmann, *Generalized 4×4 Matrix Formalism for Light Propagation in Anisotropic Stratified Media: Study of Surface Phonon Polaritons in Polar Dielectric Heterostructures*, J Opt Soc Am B **34**, 2128 (2017).

-
- [204] C. L. Garrido Alzar, M. A. G. Martinez, and P. Nussenzeig, *Classical Analog of Electromagnetically Induced Transparency*, Am. J. Phys. **70**, 37 (2002).
- [205] L. Novotny, *Strong Coupling, Energy Splitting, and Level Crossings: A Classical Perspective*, Am. J. Phys. **78**, 1199 (2010).
- [206] M. Pelton, S. D. Storm, and H. Leng, *Strong Coupling of Emitters to Single Plasmonic Nanoparticles: Exciton-Induced Transparency and Rabi Splitting*, Nanoscale **11**, 14540 (2019).
- [207] A. Frisk Kockum, A. Miranowicz, S. De Liberato, S. Savasta, and F. Nori, *Ultrastrong Coupling between Light and Matter*, Nat. Rev. Phys. **1**, 19 (2019).
- [208] C. Ciuti, G. Bastard, and I. Carusotto, *Quantum Vacuum Properties of the Intersubband Cavity Polariton Field*, Phys. Rev. B **72**, 115303 (2005).
- [209] J. George, A. Shalabney, J. A. Hutchison, C. Genet, and T. W. Ebbesen, *Liquid-Phase Vibrational Strong Coupling*, J. Phys. Chem. Lett. **6**, 1027 (2015).
- [210] A. Castellanos-Gomez, M. Buscema, R. Molenaar, V. Singh, L. Janssen, H. S. J. van der Zant, and G. A. Steele, *Deterministic Transfer of Two-Dimensional Materials by All-Dry Viscoelastic Stamping*, 2D Mater. **1**, 011002 (2014).
- [211] H. Zhang, B.-G. Shin, D.-E. Lee, and K.-B. Yoon, *Preparation of PP/2D-Nanosheet Composites Using MoS₂/MgCl₂- and BN/MgCl₂-Bisupported Ziegler–Natta Catalysts*, Catalysts **10**, 596 (2020).
- [212] Y. Kaluzny, P. Goy, M. Gross, J. M. Raimond, and S. Haroche, *Observation of Self-Induced Rabi Oscillations in Two-Level Atoms Excited Inside a Resonant Cavity: The Ringing Regime of Superradiance*, Phys. Rev. Lett. **51**, 1175 (1983).
- [213] M. G. Raizen, R. J. Thompson, R. J. Brecha, H. J. Kimble, and H. J. Carmichael, *Normal-Mode Splitting and Linewidth Averaging for Two-State Atoms in an Optical Cavity*, Phys. Rev. Lett. **63**, 240 (1989).
- [214] R. J. Thompson, G. Rempe, and H. J. Kimble, *Observation of Normal-Mode Splitting for an Atom in an Optical Cavity*, Phys. Rev. Lett. **68**, 1132 (1992).
- [215] G. Khitrova, H. M. Gibbs, M. Kira, S. W. Koch, and A. Scherer, *Vacuum Rabi Splitting in Semiconductors*, Nat. Phys. **2**, 81 (2006).
- [216] T. Niemczyk et al., *Circuit Quantum Electrodynamics in the Ultrastrong-Coupling Regime*, Nat. Phys. **6**, 772 (2010).

- [217] V. Savona, L. C. Andreani, P. Schwendimann, and A. Quattropani, *Quantum Well Excitons in Semiconductor Microcavities: Unified Treatment of Weak and Strong Coupling Regimes*, Solid State Commun. **93**, 733 (1995).
- [218] J. George, T. Chervy, A. Shalabney, E. Devaux, H. Hiura, C. Genet, and T. W. Ebbesen, *Multiple Rabi Splittings under Ultrastrong Vibrational Coupling*, Phys. Rev. Lett. **117**, 153601 (2016).
- [219] Y. N. Chen, *Antenna Coupled Quantum Infrared Detectors*, (n.d.).
- [220] A. Canales, D. G. Baranov, T. J. Antosiewicz, and T. Shegai, *Abundance of Cavity-Free Polaritonic States in Resonant Materials and Nanostructures*, J. Chem. Phys. **154**, 024701 (2021).
- [221] O. Kapon, R. Yitzhari, A. Palatnik, and Y. R. Tischler, *Vibrational Strong Light–Matter Coupling Using a Wavelength-Tunable Mid-Infrared Open Microcavity*, J. Phys. Chem. C **121**, 18845 (2017).
- [222] A. Bisht, J. Cuadra, M. Wersäll, A. Canales, T. J. Antosiewicz, and T. Shegai, *Collective Strong Light-Matter Coupling in Hierarchical Microcavity-Plasmon-Exciton Systems*, Nano Lett. **19**, 189 (2019).
- [223] S. Abedini Dereshgi, T. G. Folland, A. A. Murthy, X. Song, I. Tanriover, V. P. Dravid, J. D. Caldwell, and K. Aydin, *Lithography-Free IR Polarization Converters via Orthogonal in-Plane Phonons in α -MoO₃ Flakes*, Nat. Commun. **11**, 5771 (2020).
- [224] J. Casanova, G. Romero, I. Lizuain, J. J. García-Ripoll, and E. Solano, *Deep Strong Coupling Regime of the Jaynes-Cummings Model*, Phys. Rev. Lett. **105**, 263603 (2010).
- [225] S. De Liberato, *Light-Matter Decoupling in the Deep Strong Coupling Regime: The Breakdown of the Purcell Effect*, Phys. Rev. Lett. **112**, 016401 (2014).
- [226] N. S. Mueller, Y. Okamura, B. G. M. Vieira, S. Juergensen, H. Lange, E. B. Barros, F. Schulz, and S. Reich, *Deep Strong Light–Matter Coupling in Plasmonic Nanoparticle Crystals*, Nature **583**, 780 (2020).
- [227] A. D. Dunkelberger et al., *Active Tuning of Surface Phonon Polariton Resonances via Carrier Photoinjection*, Nat. Photonics **12**, 50 (2018).
- [228] A. A. Balandin, E. P. Pokatilov, and D. L. Nika, *Phonon Engineering in Hetero- and Nanostructures*, J. Nanoelectron. Optoelectron. **2**, 140 (2007).
- [229] J. Taboada-Gutiérrez et al., *Broad Spectral Tuning of Ultra-Low-Loss Polaritons in a van Der Waals Crystal by Intercalation*, Nat. Mater. **19**, 964 (2020).

- [230] M. Geiser, M. Beck, and J. Faist, *Terahertz Intersubband Polariton Tuning by Electrical Gating*, *Opt. Express* **22**, 2126 (2014).
- [231] I. Shlesinger, H. Monin, J. Moreau, J.-P. Hugonin, M. Dufour, S. Ithurria, B. Vest, and J.-J. Greffet, *Strong Coupling of Nanoplatelets and Surface Plasmons on a Gold Surface*, *ACS Photonics* **6**, 2643 (2019).
- [232] P. B. Johnson and R. W. Christy, *Optical Constants of the Noble Metals*, *Phys Rev B* **6**, 4370 (1972).

Acknowledgements

Después de tantas muestras, técnicas, proyectos... tanta *cleanroom* y tanta fabricación, llega el momento de agradecer a todos los que han estado a mi lado, apoyando, guiando (y aguantando, según el día) durante estos años.

To my supervisors, Luis and Rainer. Thanks for your guidance these years. I have truly learned way more than what is shown in this thesis. Luis, gracias por los consejos, el apoyo psicológico, por ser referente. Rainer, thanks for always being open to discussions, and pushing me to chase perfection down to the last comma. Thanks to both of you for this opportunity.

I also want to thank the Quantum Optoelectronics group at ETH Zürich, especially Prof. Giacomo Scalari and Prof. Jérôme Faist. Thanks for having me, it was an amazing experience among amazing people! Mathieu, Elsa, Miguel, Alexa... Thank you for making me feel at home those three months.

To everybody in nanoGUNE, especially from Nanodevices and NanoOptics groups, current and past members. I would like to thank Prof. Txema Pitarke, the director of CIC nanoGUNE, for giving me the opportunity of carrying out my work here. Fèlix, my un-official thesis supervisor. The technical team: Roger, Carlos, César, Eneko, Chris... and of course, Ralph, thanks for keeping the cleanroom under control for us!

To all the friends I made along the way (*aka* interaction area) and helped me survive the thesis with overdoses of coffee and chocolate (you know who you are). I didn't want to write names to avoid forgetting anybody, but Iris forced me to. So, if I've missed anyone, it's her fault. Here we go (in no particular order): Isabel (por cierto, creo que pronto hay rebajas...), Jose, Eoin, Yaiza, Jone, Manu, Erlaitz, Sofia, Haozhe, Uxue, Mikel (café!!), Carmen (recuérdame que te lleve chocolate), Eli (a ti también), Matteo, Iris, Florina, Marita, Andrei, Carlos, Eugenio, Monika, Edo, Jan, Iker, María, Roger, Cesar, Nerea, Juanma, Sara, Iker, Patri, Mikel, David, ...

Beatriz, tú te mereces tu propio párrafo. Gracias por tu dedicación absoluta, por tirar de mí y ayudarme a seguir siempre.

Por supuesto, gracias a mis chachis del coro: Sonia, mi primera amiga y persona de referencia en Donosti; Laura, que me abrió las puertas de esta ciudad; Ane, que se ha convertido en indispensable para mí; y los chicos, Martín, Alex, Balbino. Gracias por todas las canciones, las cervezas, y las conversaciones. Mi Donosti sois vosotros.

Volviendo a casa, no me puedo olvidar, por supuesto, de mis padres. Gracias por asegurarnos de que llegara todo lo lejos que quisiera, y por darme las herramientas para llegar a ser quién soy.

Gracias a vosotros, los de siempre. María, Yoli, Mapi, Pedro, Dani, Víctor, Jorge, por tantos años de vida compartida. Por creer en mí más que yo misma. Que esta tesis sea la ya-he-perdido-la-cuenta de muchas más aventuras a vuestro lado. Juanjo, Luna, Bea... amiguis. Por siempre estar cuando necesitaba alguien con quien hablar, un café, o simplemente marujear un rato. Y a mi sección de física: Nacho, Cris, Pili, Sof, Jorge, Quique, Bea, Ana, y allegados, Dani y Ainara. Aunque nos hayamos dispersado geográficamente, gracias por seguir cerquita. Que lo que la ciencia ha unido no lo separe el tiempo.

Por último, a ti, Lander, mi apoyo, mi compañero. ¡Qué suerte he tenido de encontrarte! Gracias por estar siempre a mi lado, escuchando todo lo que tenía que contarte. Por tenderme la mano y apostar por nosotros. Ahora empieza lo bueno.

María

En Donostia / San Sebastián,

Junio de 2023